Geometry, Kinematics & Energetics of Surf Zone Waves Near the Onset of Breaking Using Remote Sensing

Roxanne J Carini

A dissertation
submitted in partial fulfillment of the
requirements for the degree of

Doctor of Philosophy

University of Washington

2019

Reading Committee:

C Chris Chickadel, Chair

Andrew T Jessup, Chair

Jim Thomson

Program Authorized to Offer Degree:
Civil & Environmental Engineering

University of Washington

Abstract

Geometry, Kinematics & Energetics of
Surf Zone Waves Near the Onset of Breaking
Using Remote Sensing

Roxanne J Carini

Co-Chairs of the Supervisory Committee:
Affiliate Assistant Professor C Chris Chickadel
Civil & Environmental Engineering

Professor Andrew T Jessup
Civil & Environmental Engineering

The surf zone is the shallow nearshore region where waves break due to depth-limitations. These breaking waves drive important nearshore processes, including alongshore and cross-shore circulation, sediment transport, and air-sea gas and particle exchange. Measuring and modeling such processes to gain better physical understanding of surf zone dynamics and predict future coastal change is of great interest to the scientific community, as well as to the global community that relies on the coastal region and resources for security, economic stability, and recreation. Wave breaking in the surf zone is effected by bathymetry changes, currents, tides and weather, all of which result in strong spatial and temporal gradients and pose a challenge to measuring and modeling wave breaking. In this thesis, thermal infrared imagery and line-scanning LIDAR are used to measure surf zone waves near the onset of breaking. These remote sensing methods provide broad spatial coverage and high spatio-temporal resolution, which enable investigation of breaking parameters and wave energy dissipation at the onset of breaking, a time of rapid wave change that has been prohibitively challenging to accurately measure in the field.

Over 4200 waves are analyzed from data collected at the USACE Field Research Facility

in Duck, NC, including over 2600 non-breaking waves, 414 spilling breakers, 110 plunging breakers, and 1139 breakers whose initial type could not be determined. Wave height is measured using a spatio-temporal method for wave tracking that preserves the true sea surface elevation maximum and is robust to instances when the wave trough is beyond the field of view of the LIDAR transect. Methods for estimating instantaneous wave speed are refined by fitting a skewed-Gaussian function to each wave profile and tracking the fitted wave form peak. Wave slope was estimated using a variety of fitting methods to the upper 20%, 50%, and 80% of the wave face. A linear fit to the upper 80% of the wave face provides the strongest correlation with geometric wave slope defined relative to mean sea level, and the maximum wave face slope achieved by the skewed-Gaussian fitted wave form is most robust to the wave shape changes near the onset of breaking.

At the onset of spilling and plunging, critical breaking predictors are examined on a wave-by-wave basis. We find that γ, the ratio of wave height to water depth, peaks near the onset of breaking ($0.7 < \gamma_b < 0.8$ for plunging and $0.6 < \gamma_b < 0.7$ for spilling) at values consistent with solitary wave theory ($\gamma_{sol} = 0.78$) and critical γ_{rms} values previously observed at Duck and other beaches. Direct estimates of wave face slope and wave phase speed also peak at the onset of breaking. Wave face slope and γ are positively correlated and, when used together, strongly predict breaking and breaker type. A support-vector machine model is successfully used to identify or define the transition from non-breaking to breaking and from spilling to plunging.

Finally, traditionally estimated wave energy flux gradients are compared with dissipation rates estimated using the bore model and the roller model. This analysis is pursued primarily on an ensemble-averaged basis, and the results are segregated by breaker type. We find that plunging breakers lose energy at a rate 40% greater than that of spilling breakers within the first 0.2 wavelengths after the onset of breaking. Following this interval, the rate of change of wave energy flux is approximately equal for spilling and plunging breakers. The bore model

predicts maximum dissipation rate at the onset of breaking for both spilling and plunging breakers. For plunging breakers, high dissipation rate is concentrated very near the onset of breaking followed by a precipitous decrease, and for spilling breakers, the dissipation rate decreases gradually. Due to multipath reflections that can artificially augment the roller length, the roller model dissipation rates are inconclusive and require further research.

TABLE OF CONTENTS

LIST OF FIGURES

iv

v

vii

LIST OF TABLES

ACKNOWLEDGMENTS

Andy and Chris, we did it! Thank you for your patience and mentorship. Working with you has helped me grow as a scientist and a human being. You have taught me how to problem-solve in the field and ask good questions in our weekly science meetings. You have supported me through the ups and downs of graduate studies and shown great compassion through some unexpected hardships in life. Chris, your door was always open and you have been enormously generous with your time. Andy, you have advocated for me in ways seen and unseen. Thank you both for being my teachers. To the other members of my committee, Jim Thomson, Meg Palmsten, Kate Brodie, and Ryan Kelly thank you for your guidance, your thoughtful questions, your encouragement, and your career counseling.

To my Environmental Fluid Mechanics cohort, thank you for the journey. I am privileged to have grown up to be a scientist with you all, and I'm looking forward to what we will do together and on our own in the future. A special thanks to my office-mates, Mike, Seth, Maddie, and Maricarmen, for all the real life and real science questions we were open and honest and thoughtful about on a daily basis. Friends like you make it possible to finish a PhD!

To my Carini-Metzger family, thank you for all the love, support, laughs, hugs, listening, beach days and home-cooked meals over the past four years. To Peter, thanks for commiserating when I was down and providing tough love when I was lazy. Thanks for helping me see my failures as building blocks and for celebrating every little accomplishment along the way. Most importantly, thanks for helping punctuate my PhD with National Park adventures! And to my dear friends in Seattle and beyond, there are too many of you to name, but that does not diminish how much I am grateful for each of you.

DEDICATION

for Michele Dufault, a dear friend

and an enduring inspiration

Chapter 1

INTRODUCTION

1.1 Motivation

The nearshore is the region of transition between land and the continental shelf. It may include a variety of land types, such as coastal plains, wetlands, estuaries, coastal cliffs, dunes, and beaches. Nearshore regions are a mainstay of national and local economy and public recreation, and are a subject of national security. At the same time, they are vulnerable to the effects of dense human population, longterm erosion, extreme storms, and sea level rise (Elko et al., 2014). Because the nearshore responds dynamically to its environmental and anthropogenic pressures, it is a region of great interest to scientists and coastal citizens alike.

The surf zone is the shallow nearshore region where surface gravity waves are influenced by the presence of the seafloor, become unstable, and break. In the surf zone, breaking waves drive nearshore circulation, suspend sediment, and promote air-sea gas exchange. Events such as strong rip currents, beach erosion, or storm-induced flooding and infrastructure damage provide impetus for predictive models of nearshore processes. To resolve these processes, nearshore wave models must parameterize wave breaking using a chosen theory and breaking criteria. Model predictions in regions where breaking initiates often diverge from *in situ* measurements because wave breaking has large spatial and temporal variability. Additionally, even though spilling and plunging breakers dissipate energy differently, nearshore models do not incorporate breaker type in the parameterization of wave forcing. Therefore, detailed observations of spilling and plunging breakers in the field are needed to develop appropriate parameterizations of wave energy dissipation across the surf zone. Close-range remote sensing instruments, specifically LIDAR and thermal infrared imagery,

provide the spatio-temporal resolution to investigate the rapid changes that occur near the onset of breaking and are sensitive to differences between spilling and plunging breakers.

This dissertation presents extensive methodology to combine data from a line-scanning LIDAR and thermal infrared cameras to detect breaking, classify breaker type, and measure key wave parameters. Analysis of these geometric and kinematic wave properties on a wave-by-wave basis near the onset of breaking provide new ways to predict breaking and breaker type in the field. Finally, a preliminary comparison of near onset dissipation rates for spilling and plunging breakers is pursued.

1.2   *Wave Energy Dissipation Models*

In general, there are two types of wave models used in the nearshore: phase-averaged and phase-resolved. Phase-averaged models, like the Simulating WAves Nearshore (SWAN) model (Booij et al., 1997, 2008), propagate a wave spectrum onshore, using wave statistics to define breaking criteria. The goal of phase-averaged models is to model the bulk energy dissipation across the surf zone, not to replicate the details of wave breaking. This is in contrast to phase-resolved models, like the Simulating WAves till SHore (SWASH) model (Zijlema et al., 2011), which model the free surface directly to assess wave evolution and breaking. Both types of models parameterize wave breaking-induced energy dissipation using the hydraulic jump or bore model (e.g., Thornton and Guza, 1983; Janssen and Battjes, 2007).

Phase-averaged numerical models use statistical measures of the wave field to initiate breaking. The root-mean-squared wave height, water depth, and an empirical depth-limited breaking criteria γ (often tuned for better model results) are used to determine the maximum wave height supported at a given location in the surf zone. These parameters define the fraction of breaking waves and the breaking wave height probability distribution, which are used to scale the wave spectra as it propagates onshore. Phase-resolving, or wave-resolving, numerical models initiate wave breaking using a critical speed at the crest or a critical steepness of the wave face. Once exceeded, the breaking wave is modeled as a bore until

another speed or steepness threshold is reached and the wave ceases to break. Generally, these thresholds have been validated using laboratory breakers.

Essentially, phase-averaged models do not allow the total wave energy to be greater than a certain value at a given depth, and phase-resolving models do not allow individual waves to exceed a certain speed or steepness without breaking. As both model types employ the bore model, neither accounts for differences in dissipation rate due to breaker type.

1.3   Significance of Breaker Type

Plunging waves form when the wave crest overshoots the toe of the wave, as seen in Figure 1.1, and forms a large air cavity, which collapses suddenly, submerging a bubble plume and often resulting in a secondary, smaller splash-up. Spilling breakers evolve more gradually, developing an aerated, bubbly roller that slides down the front face of the wave (Figure 1.1). The classification of the breaker only applies to its initial stages, because as the beach slope and wave shape change throughout the breaking process, the breaker type changes across the surf zone. Both spilling and plunging breakers eventually reach steady state, evolving into a turbulent bore (Battjes, 1988). As breakers develop along this continuum they dissipate wave energy at different rates. Quantifying the geometric, kinematic, and energetic differences between breaker types in the surf zone is key to accurately modeling important physical processes in this region.

The classification of spilling, plunging, collapsing, and surging exists along a continuum and has been previously quantified in terms of a dimensionless surf similarity parameter, called the Iribarren number, the ratio of beach slope to wave steepness, $\xi_0 = \tan \beta / \sqrt{H_0/L_0}$, where β is the beach slope angle, H_0 is the deep water wave height, and L_0 is the deep water wavelength (Galvin, 1968). H_0 can be replaced by the breaking wave height, H_b, to define a surf zone Iribarren number, ξ_b (Battjes, 1975). Using the surf zone Iribarren number,

$$\xi_b = \frac{\tan \beta}{\sqrt{H_b/L_0}}, \tag{1.1}$$

Battjes (1975) found spilling breakers occur for $\xi_b < 0.4$, plunging for $0.4 < \xi_b < 2.0$, and
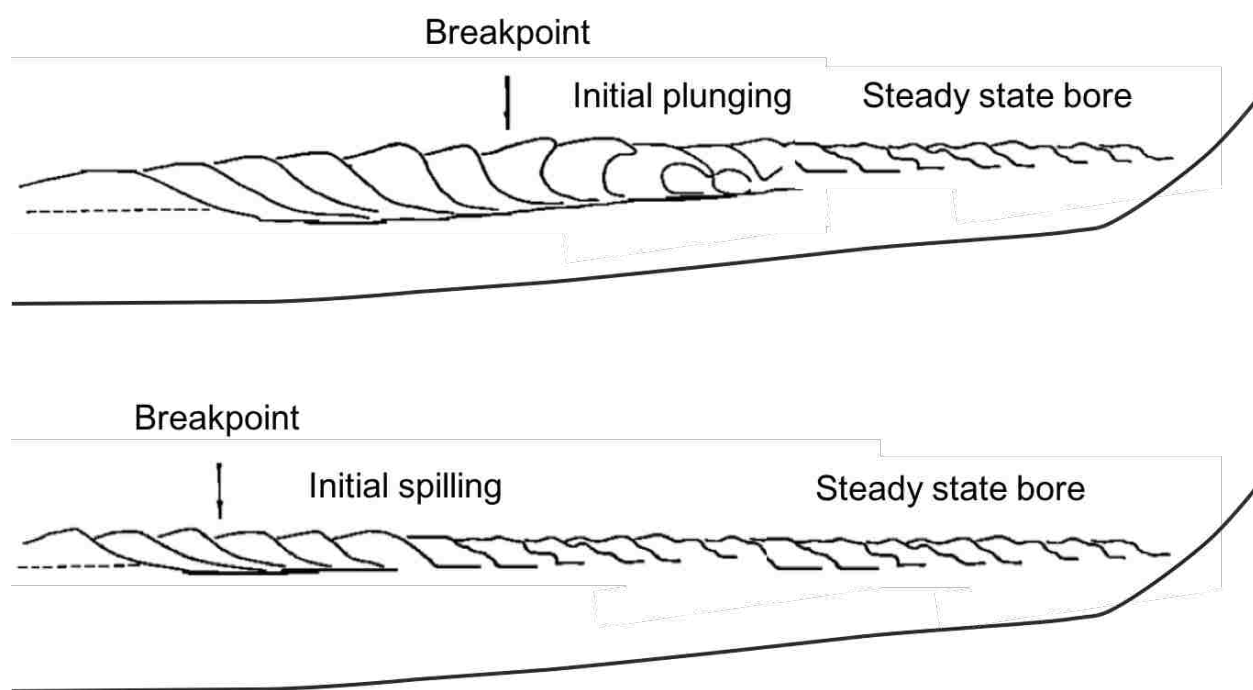
Figure 1.1: Position of water surface traced at equal time increments from films of (top) spilling and (bottom) plunging breakers on laboratory beaches. Dashed horizontal line is the still water level; arrows locate the defined breaking point. No vertical distortion. Breakpoint, initial stages and steady state stages of breaking labeled as the wave breaks across the surf zone. Image from Figure 1 of Galvin (1968).

surging and collapsing for $\xi_b > 2.0$. In other words, for a given surf zone wave steepness, spilling breakers are predicted for a shallowly sloped beach and plunging breakers are predicted for a steeply sloped beach. Collapsing and surging waves occur most frequently on steep, rocky beaches (Wright and Short, 1984) and are not considered in this surf zone study.

1.4 Remote Sensing Fundamentals

Advancement and assessment of wave energy dissipation parameterizations based on breaker type will depend on efforts to quantify and model the details of wave breaking over a range of space and time scales. Remote sensing techniques, such as visible (Electro-Optical, EO) imaging, thermal infrared (IR) imaging, and LIght Detection And Ranging (LIDAR) have been used to provide wave-resolved spatial coverage of wave breaking.

In the ocean, observable infrared signals are a combination of the emission of the scene objects and reflection of the background, in contrast to a visible band camera that sees only reflected and transmitted light from the sky and solar disk. In EO imagery, active foam, the foam generated at the crest while a wave is breaking, and residual foam, the foam left behind in the wake of a breaking wave, both appear bright (Figure 1.2a) due to the diffuse reflection of light off bubbles that make up foam. Thus it is difficult to use EO imagery to isolate the actively breaking crest from residual foam left in the wake of the breaking wave (Holman et al., 1993; Aarninkhof and Ruessink, 2004). In thermal IR imagery, foam has a higher emissivity than foam-free water, making foam appear warmer than undisturbed water of the same temperature (Niclòs et al., 2007; Branch et al., 2016), as indicated in Figure 1.2b. Observations show that foam also appears to cool rapidly after it is formed and breaking subsides (Fogelberg, 2003; Marmorino and Smith, 2005). IR imagery has been used to study deep-water wave breaking (Jessup et al., 1997a) and microscale breaking (Jessup et al., 1997b). Carini et al. (2015) recently employed a new IR technique, exploiting the unique IR signature of active foam, to detect and characterize actively breaking crests and estimate wave dissipation in the inner surf zone along a cross-shore profile.

LIDAR can be used to track the variation of wave shape and slope as it evolves. Brodie
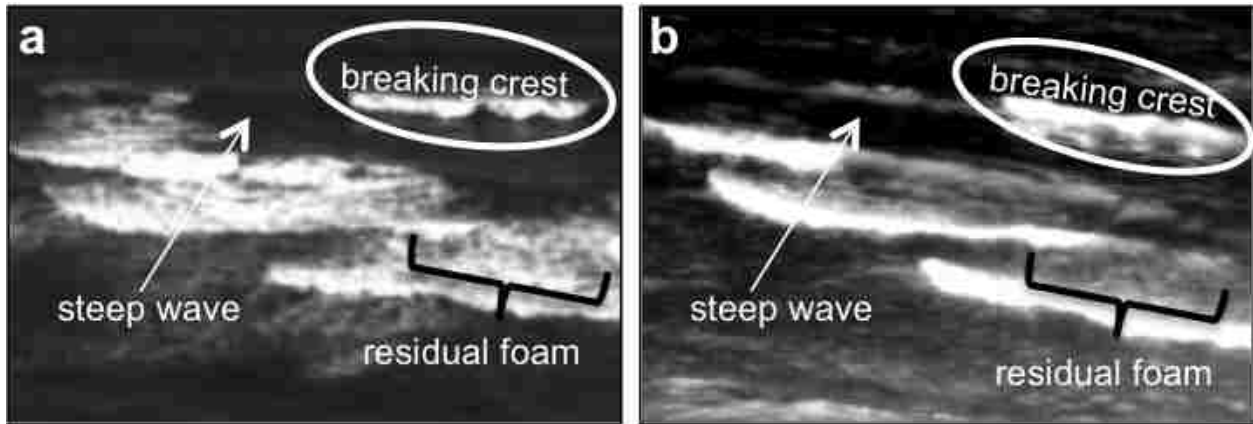
Figure 1.2: Comparison of simultaneous (a, left) visible and (b, right) infrared imagery of breaking waves in the surf zone. Active and residual foam both appear bright in the visible, while in the infrared, the breaking waves crests appear significantly brighter than the residual foam. Images adapted from Branch et al. (2014).

et al. (2015) and Brodie et al. (2016) showed that LIDAR scanners can measure the wave skewness and asymmetry at high spatial and temporal resolution, of $\mathcal{O}(1 \text{ cm})$ and $\mathcal{O}(0.5 \text{ s})$, respectively. Measurements of the evolution of wave shape across the surf zone were made from a LIDAR mounted on the shore at 8 m above the water surface, where LIDAR range varied between 65 m and 150 m depending on field conditions (foam, wave heights, rain, fog, sea spray). Figure 1.3 shows how LIDAR and IR data may be used in tandem to detect breaking and estimate key wave parameters. For example, the estimated wave face slopes (from top to bottom) in Figure 1.3 are 16°, 24°, 16°, and 11°. Recent studies using LIDAR to measure swash reflections and steady spilling breakers in the surf zone provide robust methodologies that are reviewed in Chapter 2 (Martins et al., 2016, 2017a, 2018).

1.5 Field Experiment Overview

The ROLLer EXperiment (ROLLEX) was conducted from 25 October 2016 to 10 November 2016 at the US Army Corps of Engineers (USACE) Field Research Facility (FRF) in Duck, NC. The experiment objectives were to collect remote sensing data that can be used to
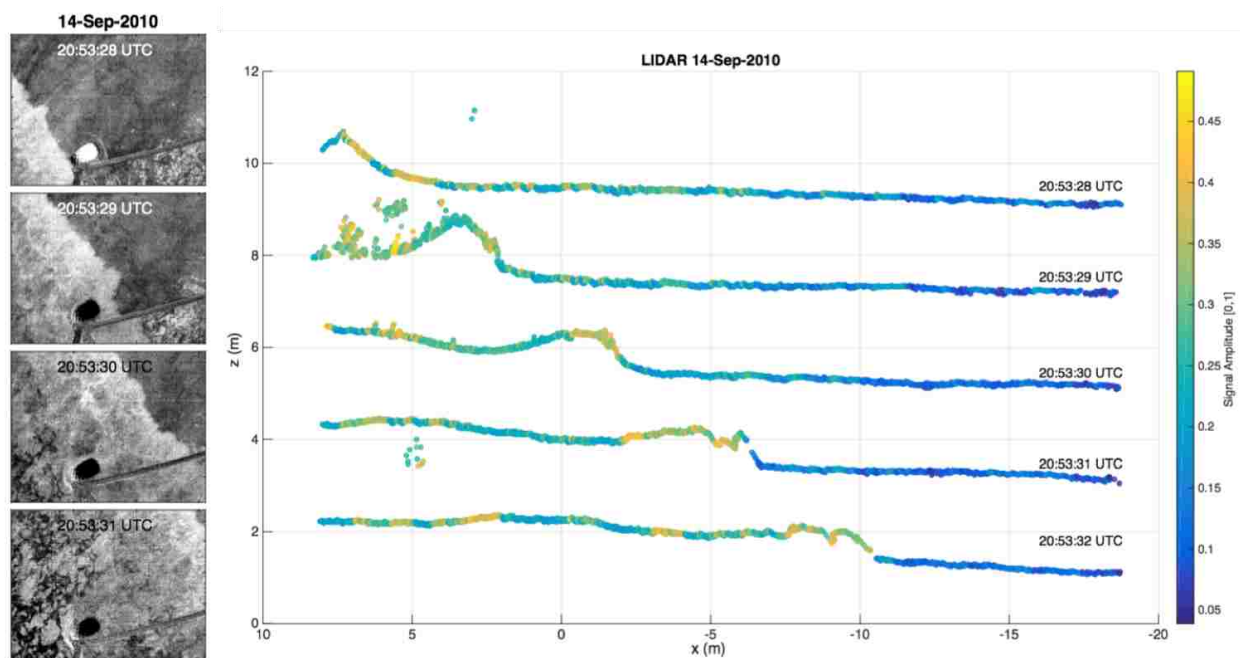
Figure 1.3: (left column) 1 Hz sequence of thermal images from the FRF Coastal Research Amphibious Buggy (CRAB), the lower part of each image. (right column) Simultaneous LIDAR scans of the wave profile show the evolution of the breaker (aspect ratio is exaggerated). Yellow and green colors indicate increased reflection from breaking wave roller and residual foam.

identify breaking waves, classify breaker type, and track the evolution of breakers across the surf zone. Breaking wave parameters would then be used to estimate wave energy dissipation due to breaking.

The surf zone at the FRF is instrumented and maintained by the USACE, and as a result of the many small and large-scale field experiments that have been conducted there over the last few decades, the site characteristics are well known. The beach morphology here is variable, but typically includes a shore-parallel sand bar or terrace, and can be punctuated by rip current channels (Plant et al., 1999). Significant wave height, H_s, at the FRF is commonly 0.2 - 1.0 m, increases to 2 - 3 m during storms, and sometimes reaches as high as 4 - 5 m (Birkemeier et al., 1985).

The FRF provides a significant amount of infrastructure including laboratories, fabrication facilities, a pier, an an imaging tower. The FRF is equipped to make detailed bathymetry measurements using amphibious vehicles and two site surveys were conducted during ROLLEX, on 03 November and 16 November 2016. These are used to define beach slope, identify any barred or plateaued bathymetry, and estimate local water depth over the course of the experiment. The FRF also maintains *in situ* instruments at 8-m and 3.5-m water depth that were used to characterize incoming wave conditions.

For ROLLEX, we deployed four thermal infrared (IR) cameras from the FRF imaging tower, two IR cameras and a line-scanning LIDAR from the FRF pier, and two *in situ* acoustic Doppler profilers (ADPs). The pier is a 6 m wide steel and concrete structure that extends approximately 560 m out from the dunes behind the beach and past the surf zone. The FRF pier deck is 7 m above mean sea level and has power access points along its length. The FRF tower is 43 m tall and is equipped with power and data connections in a small enclosure at the top, which houses an existing video imaging monitoring station (Argus).

This thesis focuses primarily on data collected from two IR cameras and the line-scanning LIDAR. One IR camera was mounted about 28 m above sea level on the FRF tower to provide a surf zone-scale field of view (FOV). The other IR camera and the LIDAR provided a wave-scale FOV from about 12 m above sea level. These two instruments were mounted to a mobile

platform that could be moved onshore or offshore throughout the experiment to maintain coverage of the breakpoint and initial stages of breaking as wave conditions changed. See Chapter 2 for a complete description of the field deployment and instrument specifications.

The wind and wave conditions recorded throughout ROLLEX are summarized in Figure 1.4. The intensity of green in the background of each panel represents how many of the remote sensing instruments were operational, with the best observational coverage occuring for 03 Nov to 09 Nov.
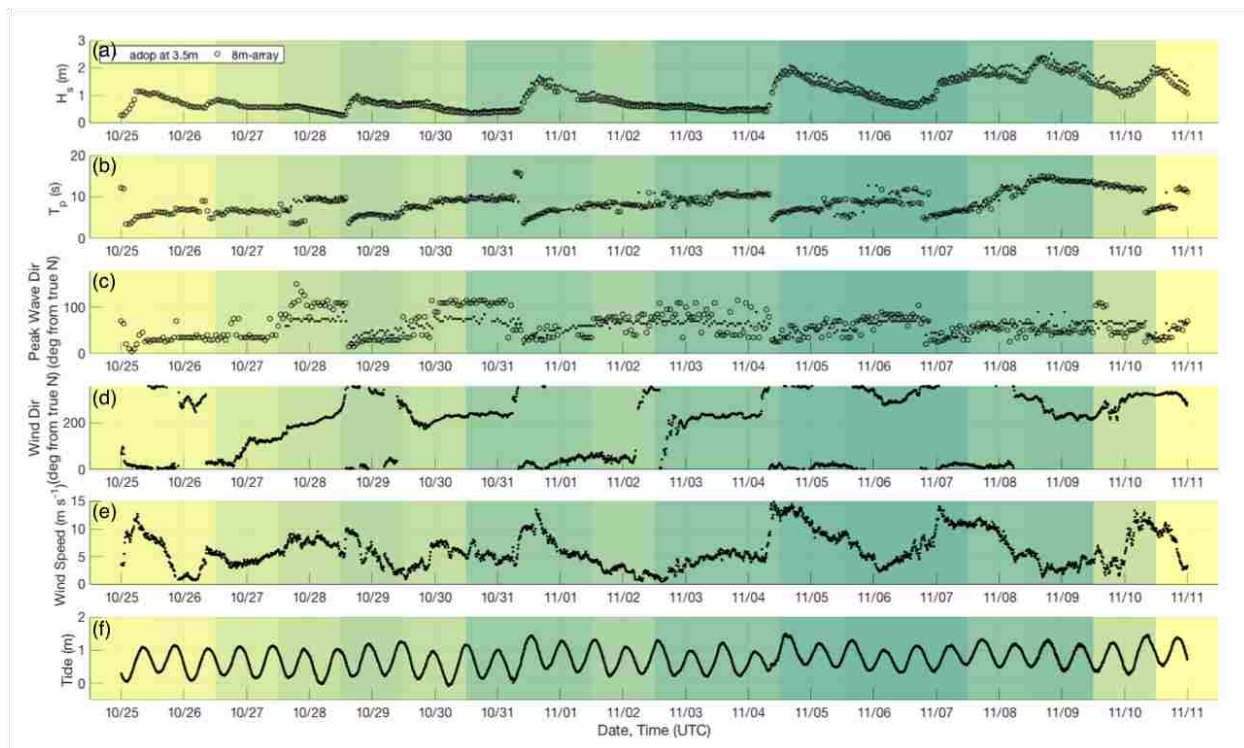
Figure 1.4: (a) Significant wave height, (b) peak wave period, (c) peak wave direction, (d) wind direction, (e) wind speed, and (f) tidal elevation throughout ROLLEX as reported by the FRF instruments in 3.5-m and 8-m water depth, the pier weather station, and the NOAA tide gauge at the end of the pier.

1.6 Thesis Outline

This thesis presents remote sensing methodologies for the study of surf zone waves near the onset of breaking. Chapter 2 details the remote sensing data fusion methods for LIDAR line-scans and thermal IR imagery. The methods are used to track, classify, and measure breaking waves. The geometric and kinematic wave parameters estimated using the techniques presented in Chapter 2 are analyzed in Chapter 3 to predict breaking and breaker type and to describe the evolution of spilling and plunging breaker near the onset of breaking. Chapter 4 extends the methods and uses key wave parameters described in Chapter 3 to estimate breaker energetics, both wave energy flux and dissipation rates near the onset of breaking. Chapter 5 summarizes the findings of this thesis, outlines remaining questions, and proposes future research.

Chapter 2

METHODS

2.1 Introduction

Nomenclature for breaking waves in the surf zone was developed during World War II, when it was imperative that wave conditions were qualitatively understood in preparation for amphibious landings (Galvin, 1968). The intuitive link between breaking wave type and the safety of a beach landing is physically substantiated by our heuristic understanding of breaker mechanics. Plunging breakers occur when the wave crest curls forward and impinges the water surface. This impinging jet may cause a secondary, smaller splash-up and creates an air cavity, which collapses, submerging a bubble plume (Basco, 1985). Spilling breakers also exhibit a curling crest, but at a much smaller scale (Duncan, 2001). This initiates an aerated roller that cascades down the front face of the wave (Basco, 1985). As they progress onshore, both spilling and plunging breakers gradually develop into turbulent steady state bores (Battjes, 1988). By their nature, spilling and plunging breakers dissipate energy differently and thus contribute differently to nearshore processes, such as air-sea gas exchange, sediment transport, and transient or steady coastal circulation. However, wave models used to predict such natural phenomena typically do not account for breaker type or stage of breaking. Specifically for wave-driven events that occur over shorter time scales, incorporating breaker type and the evolution of the stages of breaking across the surf zone may help improve model predictions. One way this can be achieved is by including key geometric wave properties that correlate with breaker type and may be used to modify the parameterization of wave energy dissipation. Thus motivated, we present the first of a two-part series addressing the evolution of spilling and plunging breakers near the onset of breaking. The major of objective of this chapter is to use remote sensing data fusion techniques for tracking, classifying, and

measuring breaking waves in the surf zone. Chapter 3 uses these measurements to investigate geometric predictors of breaking and breaker type.

Differences in geometric (e.g., wave asymmetry and roller slope), kinematic (e.g., phase speed and orbital velocities), and dynamic (e.g., breaker-induced turbulence) wave properties of spilling and plunging breakers have been measured in the laboratory (Adeyemo, 1968; Ting and Kirby, 1995, 1996; Govender et al., 2002; Blenkinsopp and Chaplin, 2007; Mukaro et al., 2013, among others) and modeled using various computational techniques (e.g., Grilli et al., 1997; Chella et al., 2016; Derakhti et al., 2018), but few field measurements are available for distinguishing breaker types and wave characteristics near the onset of breaking. Miller and Zeigler (1964) described breaker types in the field based on time-averaged sea surface and vertical velocity profiles separating them into symmetric, asymmetric, and very asymmetric categories, but concluded differentiation was still subjective. Suhayda and Pettigrew (1977) averaged ten plunging breakers, whose onset occurred at approximately the same location in the surf zone, and observed that wave height and speed peaked near onset. Weishar and Byrne (1978) found that the onset of plunging and non-plunging breakers occurred for different wave height and water depth criteria and that the breaker classification of Galvin (1968) or Battjes (1975), more commonly referred to as the Iribarren number, is insufficient to discriminate between plunging and spilling breakers. Remote sensing methodologies have greatly expanded out ability to detect the onset of breaking (Carini et al., 2015; Martins et al., 2017b) and measure wave geometries, specifically details about the plunging jet (Robertson et al., 2014) and spilling roller (Martins et al., 2018).

Remote sensing techniques that have been used to provide phase-resolved observations of waves in the surf zone include visible (Electro-Optical, EO) imaging, thermal infrared (IR) imaging, radar, and LIDAR (Holman and Haller, 2013). IR imagery has been used to study deep-water wave breaking (Jessup et al., 1997a), microscale breaking (Jessup et al., 1997b), and surf zone wave breaking (Carini et al., 2015). From the ocean surface, observable infrared signals are a combination of the thermal emission of the scene objects and reflection of the background, in contrast to the visible band, which consists of reflected light from the sun.

In EO imagery, active foam (the foam generated while a wave is breaking) and residual foam (the foam left behind in the wake of a breaking wave) both appear bright due to the diffuse reflection of light off the bubbles that make up foam. Thus it is difficult to use EO imagery to isolate actively breaking waves from the residual foam left in their wake (Holman et al., 1993; Aarninkhof and Ruessink, 2004). In thermal IR wavelengths, foam has a higher emissivity than foam-free water, making foam appear warmer (brighter) than undisturbed water of the same temperature (Niclòs et al., 2007; Branch et al., 2016). Observations show that foam also cools rapidly after it is formed and breaking subsides (Fogelberg, 2003; Marmorino and Smith, 2005), making residual foam appear darker than undisturbed water in IR imagery. By exploiting the unique IR signature of active foam, Carini et al. (2015) developed a new IR technique to detect and characterize actively breaking waves and estimate wave energy dissipation in the surf zone along a cross-shore profile. IR imagery also reveals differences between spilling and plunging breakers through distinctive temperature patterns observed on the back face of the wave. Using IR imagery in the laboratory, Watanabe and Mori (2008), Handler et al. (2012), and Huang and Hwang (2015) observed an elongated, streaky pattern of warm and cool fluid on the back of plunging breakers just before the onset of breaking. Handler et al. (2012) posited that these streaks indicate coherent counter-rotating vortices within the plunging breaker. This organized temperature structure was found to devolve into a disorganized isotropic pattern as the plunging breakers transformed into turbulent bores (Watanabe and Mori, 2008; Huang and Hwang, 2015).

LIDAR has recently been used to track the variation of wave parameters across the surf zone. Brodie et al. (2015) measured the evolution of wave height across the surf zone at spatial resolution of $\mathcal{O}(1$ cm$)$ from a LIDAR mounted on the shore at 8 m above the water surface. An extensive LIDAR methodology for measuring waves across the surf zone has been provided by Martins and collaborators, some of which are utilized in the present analysis. Of particular relevance are their wave-tracking methods (Martins et al., 2016), computation of wave phase speed (Martins et al., 2016, 2018), and direct estimation of the slope of the aerated wave face, called the roller angle (Duncan, 1981; Martins et al., 2018).

In the following sections we describe data fusion techniques for a large LIDAR and IR data set. We detail methods to track individual waves, detect breaking, and classify the type of breaking. Metrics for wave height, wave phase speed, and wave slope, are tested for non-breaking and breaking waves. The difference in wave slope at the onset of breaking between spilling and plunging breakers is provided to demonstrate the power of these methods.

2.2 Data Collection & Processing Methods

2.2.1 Field Experiment & Wave Conditions

A line-scanning LIDAR and thermal infrared (IR) cameras were deployed near the surf zone to observe waves at the onset of breaking at the US Army Corps of Engineers Field Research Facility (USACE FRF) in Duck, NC. Figure 2.1a shows the time series of tidal elevation measured by a NOAA tide gauge at the end of the FRF pier (Station ID: 8651370) and the LIDAR-derived mean sea level from the 9.6 hours of data collection spanning 07-08 November 2016. For the sampled time periods, the FRF AWAC (Acoustic Wave And Current profiler) in 3.5 m water depth reported that significant wave height gradually increased from 2.0 m to 2.5 m, peak wave period grew from 7.0 s to 14.5 s, and peak wave direction evolved from 75° to 85° relative to the shoreline, as shown in Figures 2.1b and 2.1c.

Figure 2.2a maps the positions and fields of view (FOV) of our instruments in the FRF coordinate system. This local coordinate system has its origin at 36.1776° N and 75.7497° W, with the positive x-axis pointing offshore and aligned with the FRF pier, and the positive y-axis pointing 17.7° from true north and aligned with the shoreline. The vertical z-axis is referenced to the North American Vertical Datum of 1988 (NAVD88). Two IR cameras were used in this study. One IR camera provided a surf zone-scale FOV from the FRF imaging tower (Figure 2.3a). This tower IR camera was a DRS UC640-17 long-wavelength (8-14 μm), uncooled VOx Microbolometer camera, with a 40° x 30° (H x V) FOV. It was mounted at a height of 27.8 m, obliquely viewed the surf zone at approximately 75° incidence angle, and continuously collected data at 5 Hz.
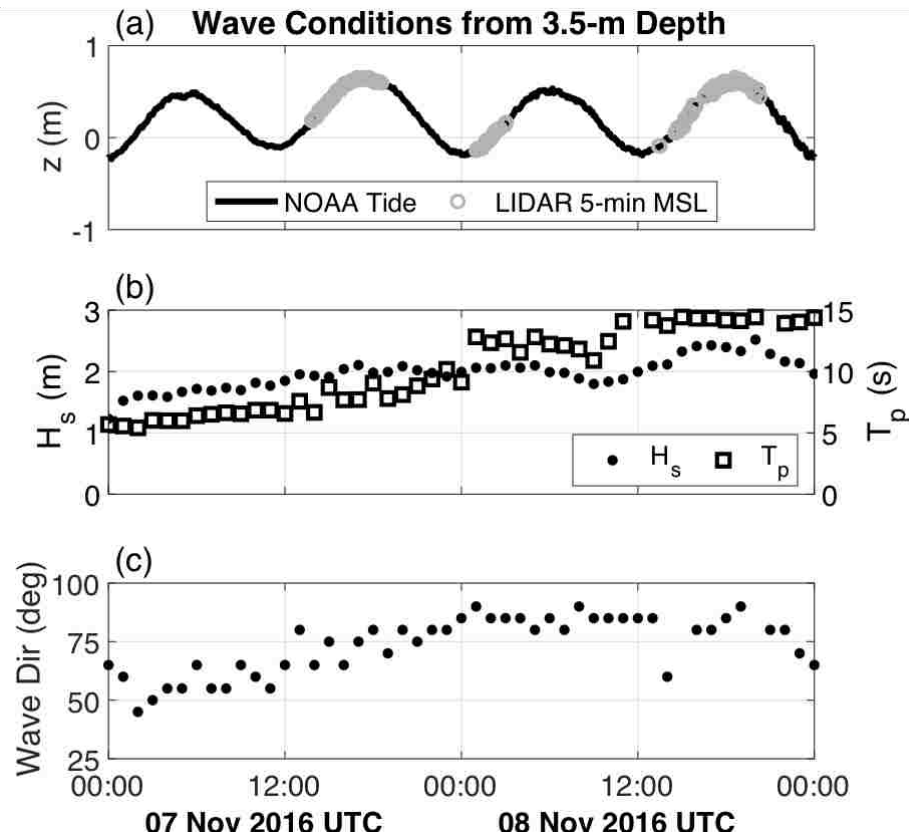
Figure 2.1: (a) Tidal elevation (solid black) and LIDAR-derived mean sea level (gray circles) for 07 and 08 Nov 2016. (b) Significant wave height (black dot) and peak wave period (black square), and (c) peak wave direction relative to the shoreline recorded by the FRF AWAC in 3.5 m water depth.
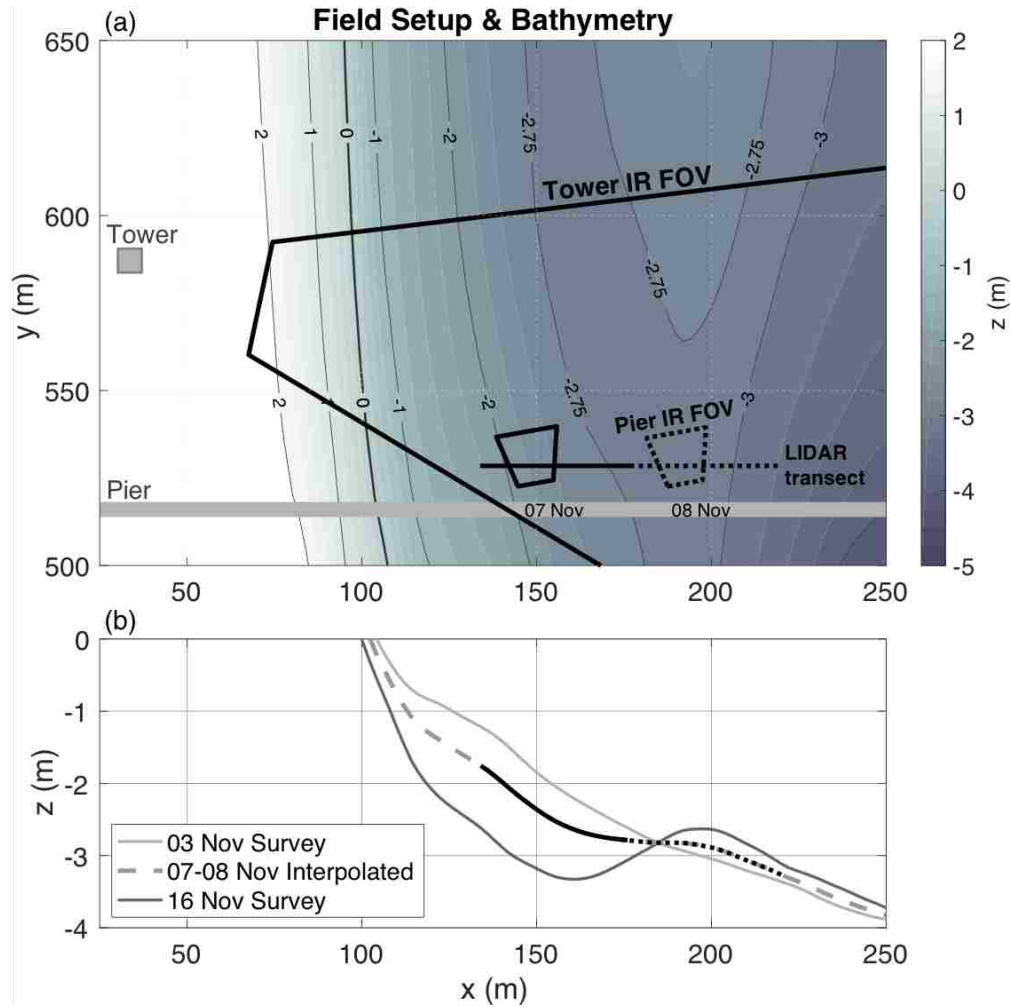
Figure 2.2: (a) A map of the tower IR camera FOV and the onshore and offshore positions of both the pier IR camera FOV and the LIDAR line-scan extent. The contours show interpolated bathymetry for 07-08 November 2016. (b) The bathymetry surveys from 03 November (light gray solid line) and 16 November (dark gray solid line) and the interpolated bathymetry (dashed gray line) are shown along the LIDAR transect range. For reference, the location of the LIDAR line-scan from 07 November (black solid line) and 08 November (dotted black line) are overlaid.
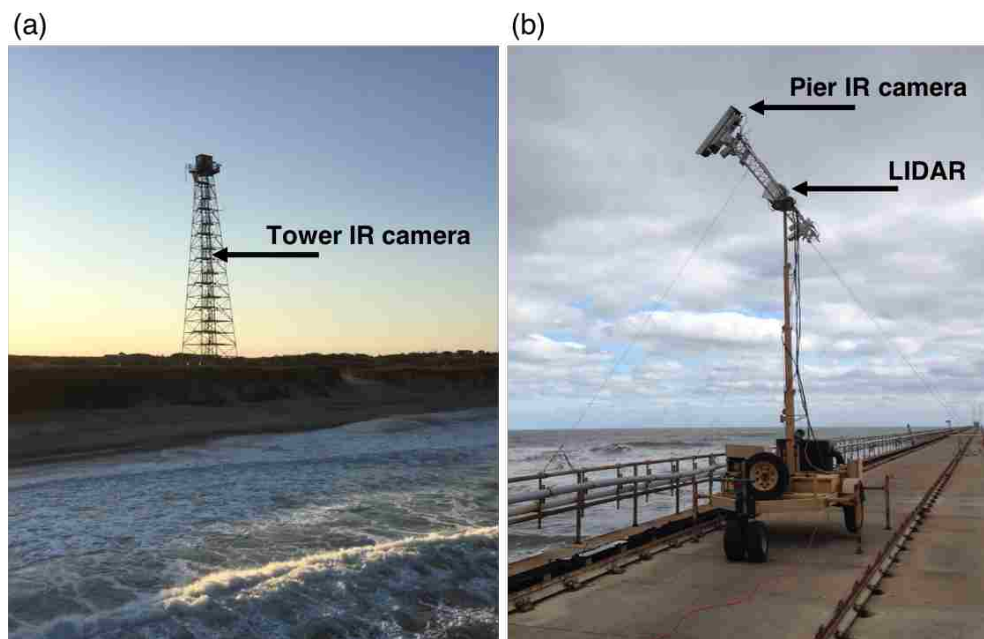
Figure 2.3: (a) The FRF imaging tower with the location of the tower IR camera labeled. (b) The mobile pier platform positioned along the FRF pier and secured with guy lines, with the pier IR camera and the LIDAR labeled.

The second IR camera and a line-scanning LIDAR provided wave-scale observations from the FRF pier. Both were mounted to a mobile pier platform, which consisted of a 6m-long frame mounted at the top of a telescoping stand (Figure 2.3b). The platform was raised to its maximum vertical position of $z = 13.2$ m to allow for optimal data collection and was stabilized by four guy lines attached to the pier. As the sea state evolved during the experiment, the platform was moved to maintain coverage of the cross-shore region spanning the onset of breaking, as marked in Figure 2.2a. The pier IR camera, identical to the tower IR camera, viewed the sea surface at 45° incidence angle and collected data continuously at 10 Hz. The LIDAR, a Riegl VZ-400, collected line-scans at 5.2 Hz. It scanned 40° onshore and 60° offshore of its position, yielding 30-40 m-long cross-shore line-scans, as shown in Figure 2.2a. The alongshore position of the line scans varied with the tidal elevation, but were located approximately 12 m north of the pier.

Bathymetric surveys of the study region were collected by the USACE using the LARC (Lighter Amphibious Resupply Cargo) land-sea surveying vehicle (Forte et al., 2017; Forte and Dopsovic, 2016) on 03 and 16 November 2016. These bathymetric surveys, shown in Figure 2.2b, reveal the initial and final beach states (planar and single-barred, respectively) at the location of the LIDAR cross-shore transects. To estimate a representative bathymetry for 07-08 November 2016, we interpolated between the two surveys using a linear weighting function based on the time between the data collection and each bathymetric survey. Evidence supporting this linearly interpolated bathymetry is provided in Appendix A. This interpolated bathymetry is shown in Figure 2.2a and 2.2b. The local beach slope was estimated using the interpolated bathymetry and ranged from 1:50 to 1:25 at the onshore LIDAR position and 1:500 to 1:50 at the offshore LIDAR position.

2.2.2   Data Transformation to Field Coordinates

A total station was used to survey the 3D locations of both IR cameras, five reference points with known FRF coordinates, and several ground control points (GCPs) across the beach and swash zone. Given these 3D points in FRF coordinates and their corresponding 2D

points in each IR image, a projective mapping was created for the tower IR camera (Holland et al., 1997; Hartley and Zisserman, 2003). Because the FOV of the pier IR camera did not capture any of the surveyed GCPs, a rectification was estimated using the surveyed camera location and its tilt as measured by a surveying level placed on the camera housing. The resulting approximate camera geometry was judged to be adequate since this camera was only used to visually assess the breaker type.

For the LIDAR, we developed an adaptive method to register the data from the LIDAR coordinate system (x', y', z') to the local FRF coordinate system (x, y, z) because the orientation of the LIDAR varied slightly throughout the experiment. Each time the pier platform was moved, we surveyed the LIDAR position and known FRF GCPs and used this information to compute the LIDAR position in FRF coordinates, (x_ℓ, y_ℓ, z_ℓ). To determine the orientation of the LIDAR, the following calculations are performed on each five-minute LIDAR data file. First, the roll of the LIDAR is determined by fitting a line in the x'-z' plane to all of the collected points. Since the LIDAR was deployed on its side, the roll angle is computed as $90° - \tan^{-1}(m)$, where m is the slope of the fitted line. We rotate the data points using this roll angle, which renders the linear fit horizontal. Over 07-08 November 2016 the mean and standard deviation of the data-derived roll were 88.5° and 0.3°, respectively. Next, the distance from the LIDAR to the sea surface is computed using the rectified instrument position (x_ℓ, y_ℓ, z_ℓ) and the tidal elevation from the NOAA tide gauge (Station ID: 8651370) located at the end of the pier, which reports mean sea level every six minutes. The tilt is chosen as the angle which, when applied to the data, rotates the mean sea surface line closest to the tidal elevation. Over 07-08 November the mean and standard deviation of the data-derived tilt were 26.3° and 0.5°, respectively. The azimuth of the instrument was estimated using a plane fit to three surveyed points on the base of the LIDAR and was found to be 0.08° and to vary less than 0.05° between deployments. Therefore, additional azimuthal rotation was not implemented. Last, the LIDAR data was translated to the FRF coordinate system by adding the instrument's FRF position, (x_ℓ, y_ℓ, z_ℓ).

While this projection correction method is useful for situations where accurate orientation

data is unavailable, due to the removal of any mean sea surface slope in the fitting process of each data file, this method is not appropriate for measuring wave setup or set-down. However, if the instrument is stationary throughout the experiment and the orientation calculations are performed on a period of time when waves are small, then wave setup or set-down may be estimated.

2.2.3 LIDAR Quality Control

The density of LIDAR returns depends on the instrument's spatial resolution and the reflector (i.e., the water surface) characteristics (Blenkinsopp et al., 2010; Brodie et al., 2015). When there is sufficient breaking to produce foam that persists on the water surface or sufficient surface roughness, the density of backscattered returns is high, and the LIDAR is able to capture breaking and non-breaking wave profiles. When there is no breaking, or no persistent foam, the smooth water surface specularly reflects the signal away and the density of returns is low. Therefore, it is important to determine when the collected LIDAR data sufficiently samples the sea surface to resolve detailed features of the wave profile.

We first interpolated the irregularly spaced LIDAR points to a uniform grid using an appropriate and achievable spatial resolution. Operating in long-range mode, the LIDAR can collect point-measurements at 42 kHz (when line-sampling at 5.2 Hz), yielding a theoretical maximum of 8076.9 point-measurements per line and an angular resolution of 0.0124°, for our field setup. The corresponding spatial resolution at the water surface is shown in Figure 2.4a as a function of cross-shore position. At 15 m onshore of the LIDAR, the spatial resolution is 0.61 cm, and at 30 m offshore of the LIDAR, the spatial resolution is 1.4 cm. The highest resolution, 0.36 cm, occurs at nadir. Based on this theoretical resolution curve, we uniformly interpolated the LIDAR transects to 1 cm resolution.

To address variations in return density, we developed a quality control criterion to determine when to accept or reject the LIDAR data based on an expected minimum sampling rate. If five minutes of data were collected at the spatial resolution shown in Figure 2.4a and binned every 10 cm, the resulting theoretical histogram of returns would match the
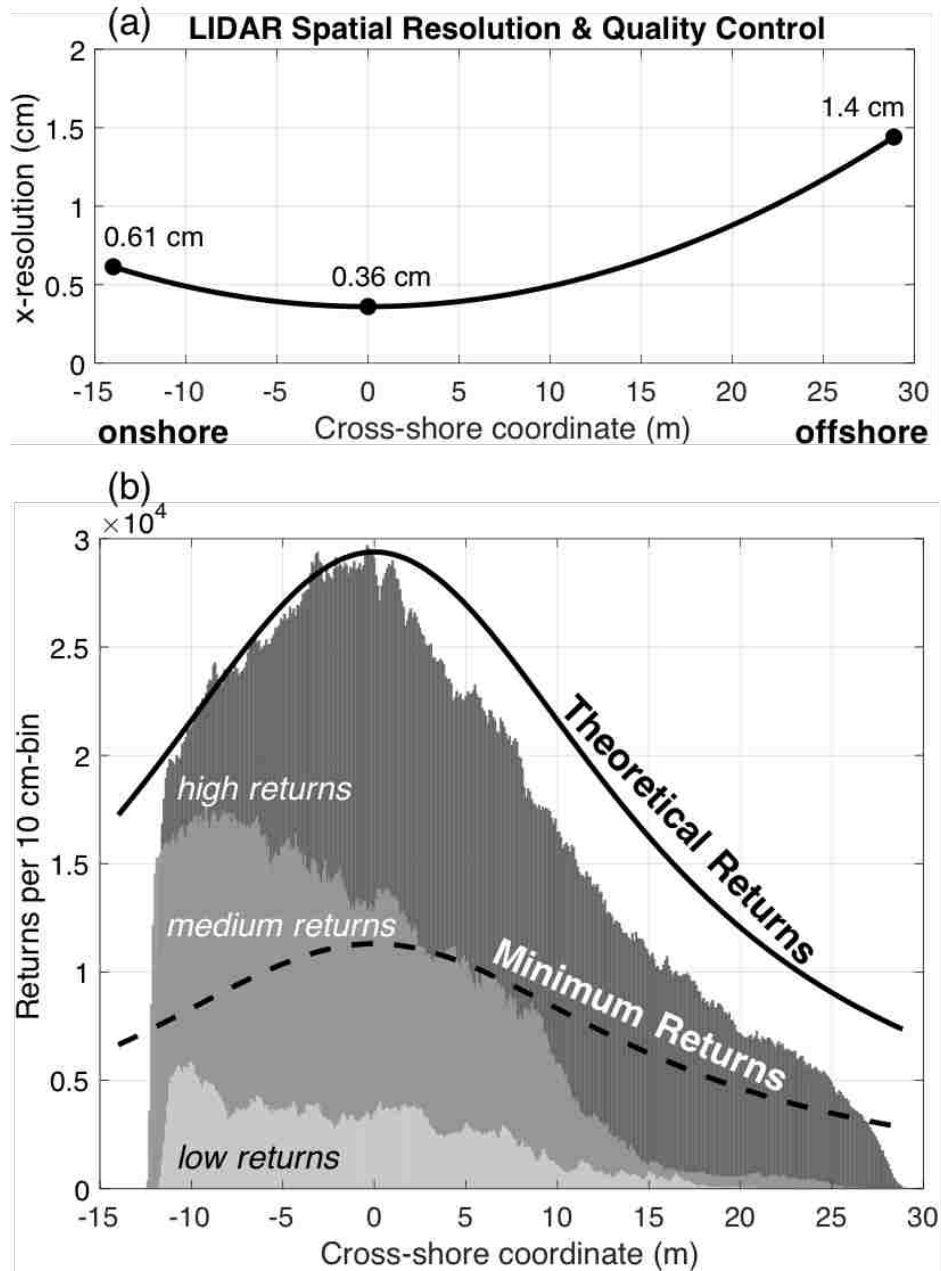
Figure 2.4: (a) Spatial resolution of the LIDAR as a function of cross-shore position. LIDAR located at cross-shore coordinate = 0. (b) Example histograms of LIDAR returns as a function of cross-shore position demonstrating the LIDAR quality control method. The theoretical returns curve (solid black line) and the minimum returns curve (dashed black line) demonstrate perfect sampling and adequate sampling, respectively.

solid black curve in Figure 2.4b. This histogram represents the maximum returns at 5.2 Hz sampling, which we neither expect nor require. Instead, a minimum histogram of returns was computed using 2 Hz sampling frequency (dashed black curve in Figure 2.4b), which would allow resolution up to a 1 Hz Nyquist frequency. This minimum-returns curve can be computed for any chosen spatial resolution, sample duration, and data-binning scheme. Any time the density of measured returns falls below the minimum-returns curve, that part of the cross-shore transect is excluded. For example, of the three overlaid histograms of LIDAR signal returns in Figure 2.4b, we can use nearly all of the high return density data (dark gray), only the onshore part of the medium return density data (medium gray), and none of the low return density data (light gray).

2.3 Data Analysis Methods

2.3.1 Wave-tracking & Wave Parameter Estimation

Central to our methodology is the development of a spatial wave-tracking algorithm that uses the full spatial and temporal resolution of the LIDAR. Our spatial peak-tracking method is illustrated in Figure 2.5. The cross-shore profiles of sea surface elevation from 30 s of data collection are plotted as a timestack in Figure 2.5a, where height is indicated by color. In the timestack, waves travel from offshore (right) to onshore (left) as time progresses from top to bottom. To initially identify each wave, we extract a time series from the offshore edge of the timestack and define initial wave peaks (x_0, t_0) as local maxima, with a minimum separation of 2 s between peaks and a minimum peak prominence of 0.25 m. Next, we extract the cross-shore transect at t_0 and choose the surface elevation maxima as the initial spatial peak, (x_{pk}, z_{pk}). This wave peak is then tracked at every time step by searching for surface elevation maxima in each sequential cross-shore transect (solid black lines in Figure 2.5a). The search is confined to the region between the location of the previous peak and a shoreward position of twice the distance the wave would have moved if traveling according to shallow water linear wave theory. Tracking continues at each time-step until we reach the

onshore limit of the transect. Each wave may vary in how many instances it was tracked due to variations in speed: faster waves travel farther between each time step and are therefore tracked at fewer points over the full transect.

In addition to tracking the peak, we track the preceding and following troughs. Figure 2.5b and 2.5c show an example spatial profile of a breaking wave and its corresponding time series, respectively. While surf zone waves have well-defined peaks, the troughs are characteristically broad and flat (Munk, 1949; Komar and Gaughan, 1973), making the trough location ambiguous, though the trough elevation is well-defined. Additionally, due to the limited cross-shore extent of our line-scans, we often do not capture the full wavelength, as is the case in Figure 2.5b, and thus cannot identify preceding and following troughs simultaneous with a peak. Therefore, we extract the time series at the location of the tracked peak and identify the trough elevations z_{tr-t} (temporal minima) just before and after the tracked peak, similar to Martins et al. (2017b). Wave period, T, is estimated as the time between these preceding and following troughs, as shown in Figure 2.5c. Individual wave heights are then computed as the difference in elevation between the spatially-tracked wave peak and temporally-tracked preceding wave trough, $H = z_{pk} - z_{tr-t}$. Note that parameters derived from the spatial profile will be denoted either with no additional subscript (as seen in the definition of H) or with subscript x, and parameters derived from the time series will always be denoted with subscript t.

Individual wave speed c is estimated from the tracked wave peaks as the slope of a 5-point moving linear regression on the (t_{pk}, x_{pk}) values, following the methods of Tissier et al. (2015) and Martins et al. (2018). This method is more robust than using the scan-to-scan velocity of the tracked peak ($\triangle x / \triangle t$). However, the 5-point regression is still susceptible to peak misidentification due to noise and rapid wave shape changes near the onset of breaking. To overcome this issue, we fit each wave form with an idealized wave shape, here formalized as a skewed-Gaussian curve, shown in Figure 2.5b. A skewed-Gaussian function,

$$f\left(\frac{x-\mu}{\omega}\right) = A\phi\left(\frac{x-\mu}{\omega}\right)\Phi\left(\alpha\left(\frac{x-\mu}{\omega}\right)\right) + \zeta, \qquad (2.1)$$
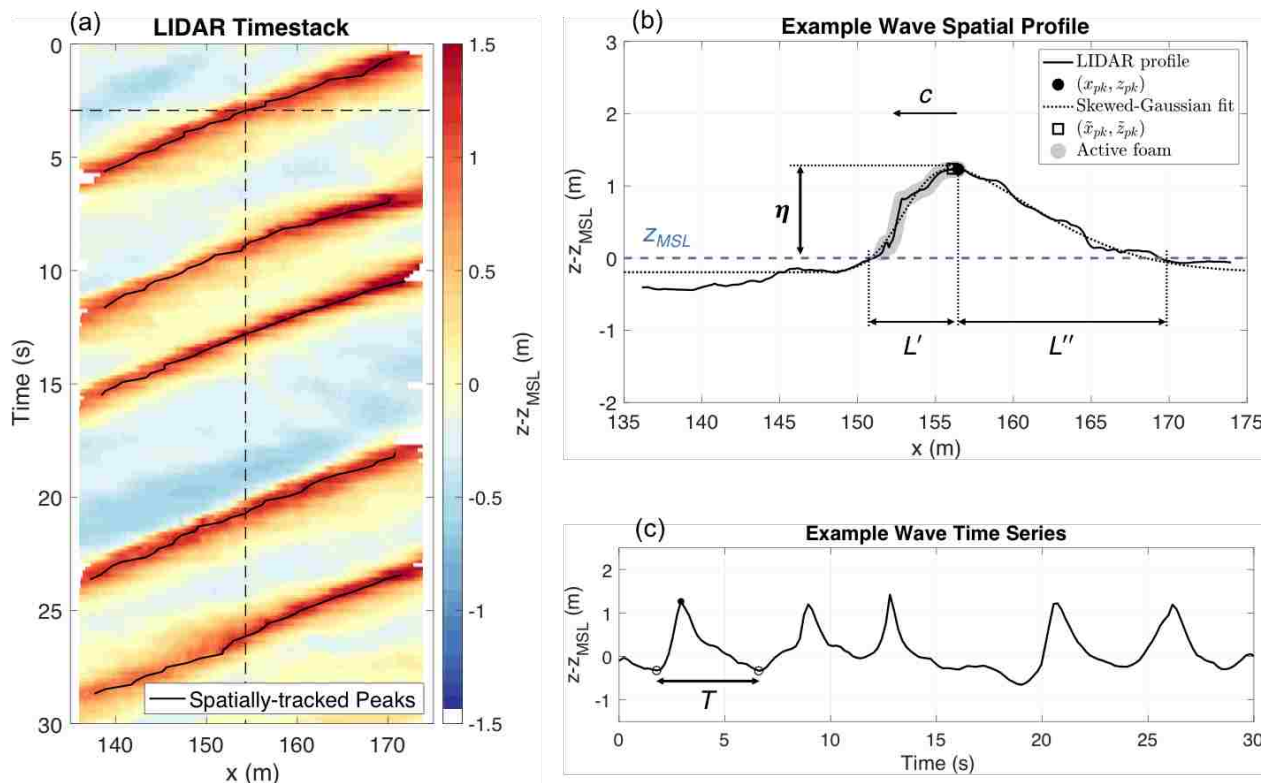
Figure 2.5: (a) A timestack showing five tracked waves. The color map represents sea surface elevation relative to mean sea level (z_{MSL}). The solid black lines show the progression of the spatially-tracked wave peaks. (b) Spatial profile from an example breaking wave extracted along the horizontal dashed line in (a). The interpolated LIDAR profile (solid black line) and spatially-tracked peak (black dot) are plotted relative to z_{MSL} (dashed blue line). The wave profile is fitted with a skewed-Gaussian curve (dotted black line). c) Time series extracted along the vertical dashed line in (a), with wave peak (dot) and preceding and following troughs (open circles) from the "example wave" marked by closed and open circles, respectively.

is the scaled product of a standard normal probability density function,

$$\phi(r) = \frac{1}{\sqrt{2\pi}} e^{-\frac{r^2}{2}}, \tag{2.2}$$

and its cumulative distribution function,

$$\Phi(r) = \frac{1}{2}\left[1 + \mathrm{erf}\left(\frac{r}{\sqrt{2}}\right)\right], \tag{2.3}$$

where r is a dummy variable representing $(x - \mu)/\omega$. The skewed-Gaussian function (2.1) was chosen to match the expected shape changes that are characteristic of a breaking wave as it pitches forward prior to breaking. The wave shape function is fit to the measured profile using a non-linear optimization of the peak location (μ), peak width (ω), horizontal skewness (α), a scaling parameter (A) and a vertical offset (ζ). For the example breaking wave in Figure 2.5b, μ=151.71, ω=7.95, α=6.72, A=3.56, ζ=0.47. To assess the goodness of fit, we use a sample χ^2 statistic,

$$\chi^2 = \Sigma\left[\frac{(z - z_{SG})^2}{\sigma_{tot}}\right], \tag{2.4}$$

where $\sigma_{tot} = \sigma_{LIDAR} + \sigma_{interp}$ is the sum of instrument variance (assumed constant at 1 cm) and the mean absolute difference between the raw and interpolated LIDAR profiles ($\langle|z_{raw} - z_{interp}|\rangle$). If the χ^2 value is less than the critical value for a χ^2 distribution with 45 degrees of freedom (conservative estimate from the 4501 cross-shore points included in the analysis) at 95% confidence, we accept the fit. For our dataset, 92.7% of the skewed-Gaussian fitted profiles pass the χ^2 test. The fitted profiles provide sub-pixel tracking of the wave peaks, $(\tilde{x}_{pk}, \tilde{z}_{pk})$, which yields a smoother estimate of wave speed, $\tilde{c}$, estimated using the 5-point moving linear regression method. Additionally, we use the skewed-Gaussian fitted wave speed and the wave period to estimate wavelength, $L = \tilde{c}T$. We do not estimate wavelength directly because our cross-shore transects did not consistently capture a full wavelength.

The water depth through which a wave travels is computed as the difference between the measured mean sea level and the interpolated bathymetry at the location of the wave peak,

$h = z_{MSL} - z_{bathy}(x_{pk})$. Using z_{MSL} as a reference level and following definitions proposed by Kjeldsen et al. (1979), we estimate wave asymmetry, L'/L'', and wave slope, η/L', as illustrated in Figure 2.5b. Three additional wave slope metrics are computed. First, we fit a line to a portion of the wave face and use the fitted slope, m_ℓ. Section 2.4.3 compares wave slope η/L' to m_ℓ computed using the upper 20% of the wave face, the upper 50%, the upper 80%, and the full wave face. For those waves nearing the onset of breaking, especially plunging breakers, a quadratic fit to a portion of the wave face may be more appropriate. Second, the maximum gradient achieved by the quadratic fit over the wave face is taken as the quadratic fit wave slope, m_q. Lastly, the maximum slope achieved by the skewed-Gaussian over the wave face is m_{SG}.

2.3.2   Breaker Detection & Classification Using IR Imagery

For each wave tracked in the LIDAR data, we use the corresponding surf zone-scale IR imagery (from the imaging tower) to determine if the wave was breaking and the wave-scale IR imagery (from the pier) to classify the type of breaker. Figure 2.6 outlines the breaker detection and classification protocol. First, we determine candidate breakers using an automated detection algorithm on the surf-zone scale IR imagery. The automated detection algorithm, developed by Carini et al. (2015), determines a threshold based on the distribution of pixel intensities and applies this threshold to isolate active breaking. Figure 2.7a presents an example surf zone-scale IR image, with active breaking marked in red. The 3D LIDAR transect is projected into 2D image coordinates and the corresponding binary values, breaking or not-breaking, are extracted to create a breaking mask for each LIDAR transect, as shown in Figure 2.7c. Following the protocol in Figure 2.6, if the automated detection algorithm never indicates active breaking along the LIDAR transect for a given tracked wave, then that wave is classified as non-breaking. For those instances where the automated detection algorithm indicates active breaking along the LIDAR transect, the wave-scale IR imagery, shown in Figure 2.7b, is manually reviewed to determine breaker type.

Any wave whose onset of breaking occurred offshore of the FOV of the wave-scale IR

(1) Use automated detection algorithm to find *candidate breakers* in surf zone-scale IR imagery:

Was active foam detected at any point during observation?

YES

NO
**Type = Non-breaking
Stage = Not breaking
(for all time steps)**
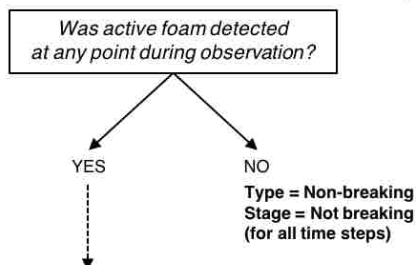
(2) Manually review *candidate breakers* in wave-scale IR imagery:

Was the wave already breaking when it entered the FOV?

YES
**Type = Undetermined
Stage = Breaking
(for all time steps)**

NO

Has the crest overturned?

YES
Stage = Onset

NO
Stage = Not breaking

Progress to next time step.
**Stage = Breaking
(for all remaining time steps)**

What best characterizes the texture of the back face of the wave?

UNIFORMLY PATCHY
Type = Spilling

ORGANIZED STREAKS
Type = Plunging

Figure 2.6: Flow chart describing the process of breaker type classification ("Type") and determination of the onset of breaking ("Stage") using the surf zone-scale and wave-scale IR imagery for each wave tracked in the LIDAR data.
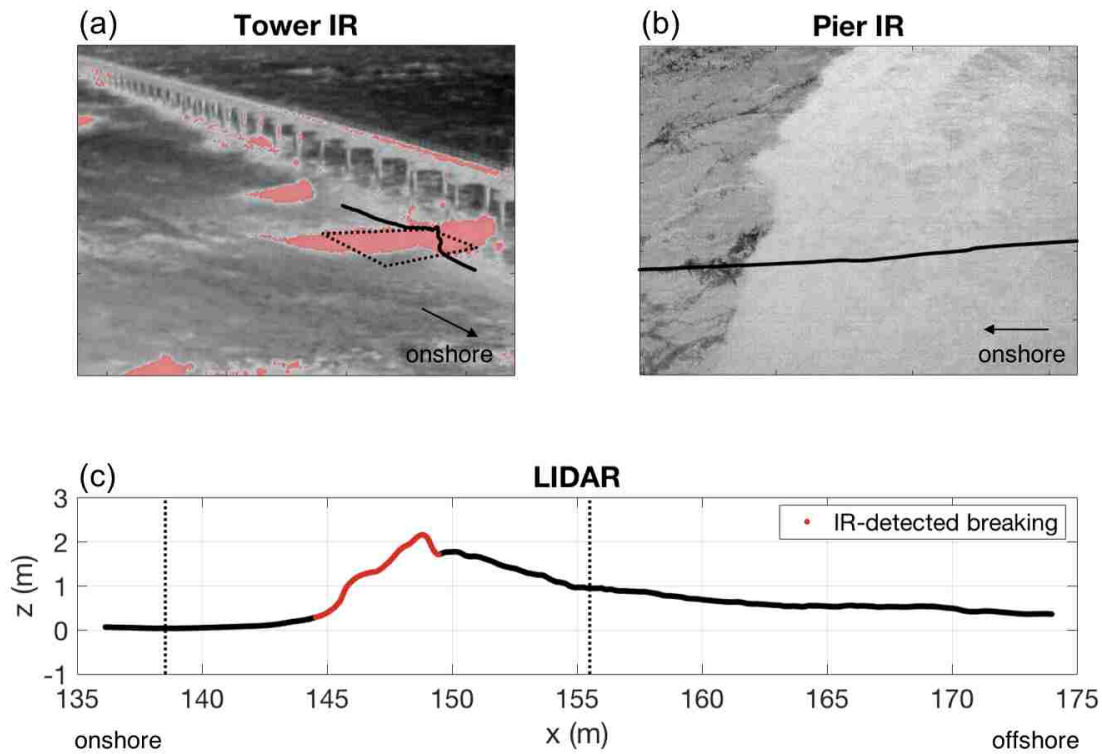
Figure 2.7: (a) An example image from the tower IR camera with identified breaking (and the warm pier) indicated by red. The corresponding LIDAR transect (solid black curve) and the pier IR camera FOV (dashed outline) are projected onto the image. The mobile pier platform is on the pier, in the far right of the image. (b) The corresponding example image from the pier IR camera with the LIDAR transect (black line) projected into the image. (c) The corresponding example LIDAR transect is shown with active breaking highlighted in red on the front face of the wave, and the FOV of the pier IR camera is marked by dashed lines.

camera and continued breaking throughout the FOV is classified as a breaker of undetermined type. If the wave is not breaking when it enters the FOV, the wave-scale imagery is manually reviewed at each time-step to determine the onset of breaking. Onset is defined as the moment the wave crest begins to overturn. To illustrate onset for spilling and plunging breakers, Figure 2.8 shows example images at pre-onset, onset, the frame following onset, and a later time. Breaker classification is based on the IR signature of the back face of the wave once it has progressed past onset to the breaking stage. For spilling breakers, the propagating roller creates an unorganized texture in the IR imagery on the back face of the wave, shown in Figure 2.8d. For plunging breakers, the straining of the fluid on the back face of the wave as the crest curls over results in an organized streak pattern in the IR imagery, shown in Figure 2.8h. Both spilling and plunging breakers evolve to a steady state over some amount of time and space (Battjes, 1988; Basco, 1985), but the limited cross-shore extent of our LIDAR transects precludes a full investigation of this transition.

2.4   Results

All wave parameters defined in Section 2.3.1 are computed and wave type is classified for each wave profile measured across the LIDAR transect. Over the 9.6 hours of data analyzed, we observed 2627 non-breaking waves, 1139 breakers of undetermined type, 414 spilling breakers, and 110 plunging breakers, for a total of 4290 waves. Figure 2.9 shows the evolution of wave height, wave speed, and wave slope for one example plunging breaker. The onset of breaking is marked by the vertical line. Statistics computed from wave-by-wave results for each wave parameter will be reported and discussed in the following sections.

2.4.1   Wave Height

To validate the wave heights estimated using the temporally-derived preceding wave troughs, z_{tr-t}, and the spatially-derived wave peaks z_{pk-x}, we compare our results with those estimated using traditional temporal methods. In this section, parameters derived from the spatial profile will always be denoted with subscript $-x$, and parameters derived from the time
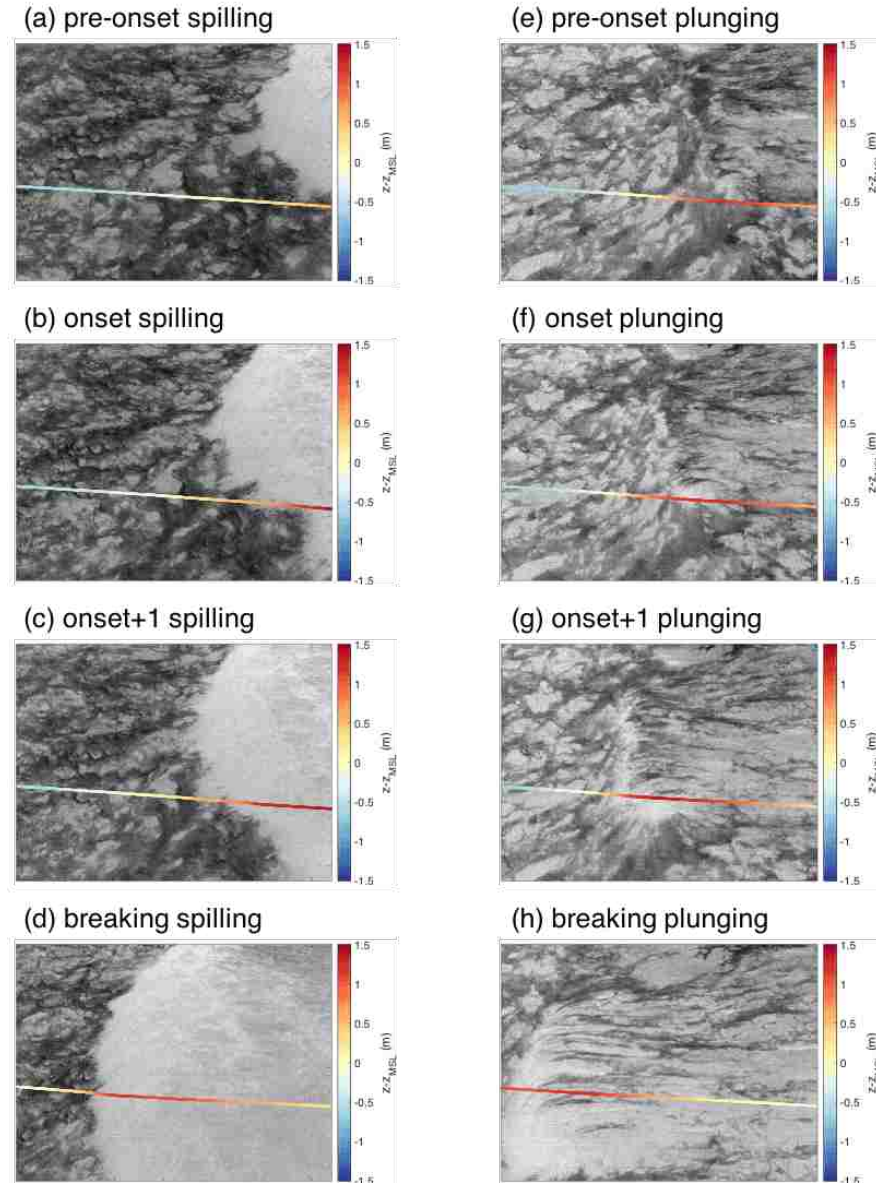
Figure 2.8: Wave-scale IR images of a spilling (left column) and a plunging (right column) breaker at various stages: (a,e) pre-onset, (b,f) onset, (c,g) one frame (approximately 0.2 s) after onset, and (d,h) breaking. The back face of a spilling breaker exhibits a uniformly patchy texture in the IR imagery. In contrast, the back face of a plunging breaker is characterized by an organized streak pattern in the IR imagery.
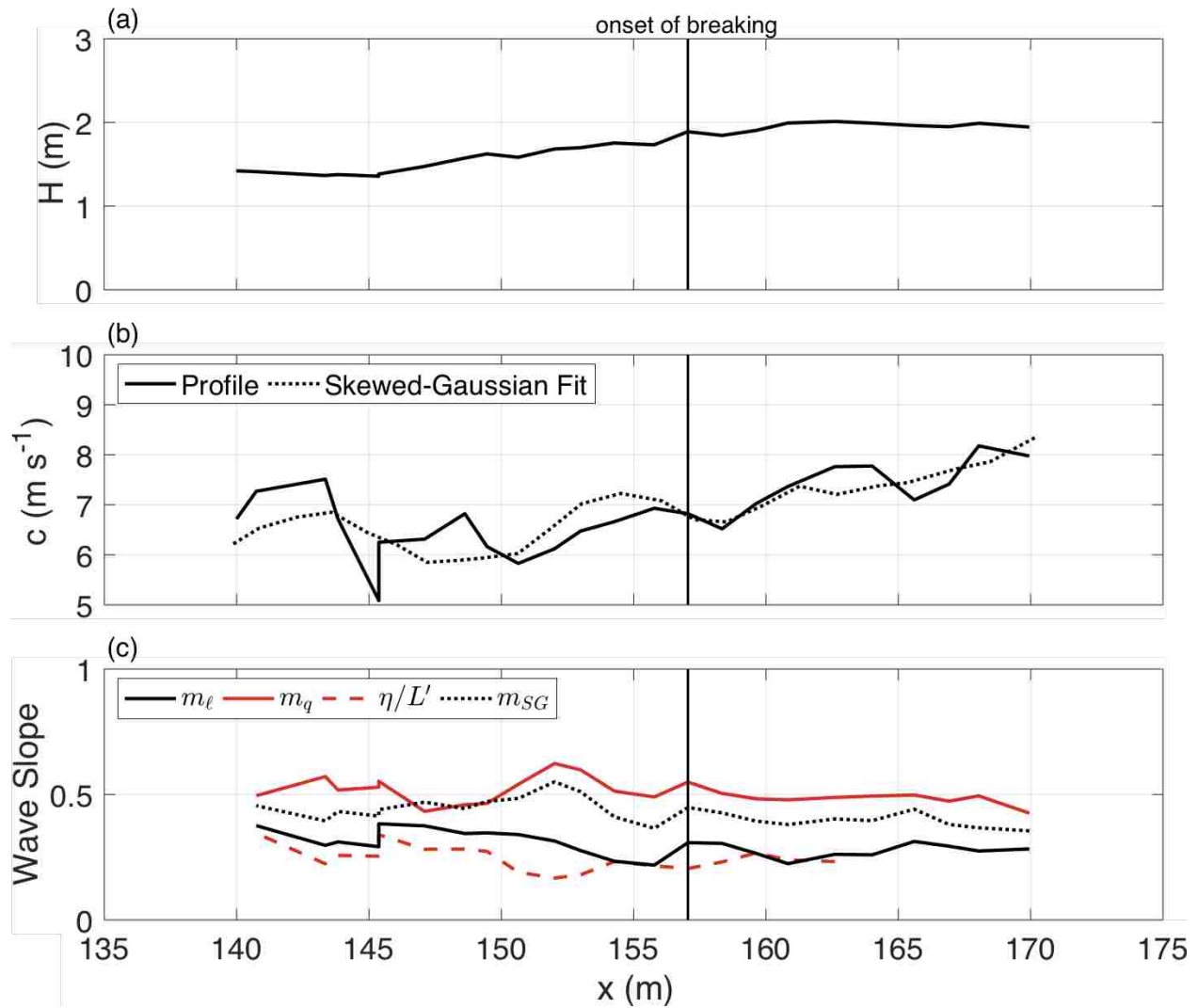
Figure 2.9: The evolution of (a) H, (b) wave speed, and (c) wave face slope across the surf zone for the example wave in Figure 2.5. Wave speed is reported for the interpolated LIDAR profile (solid line), as well as the skewed-Gaussian fit (dotted line). Four wave slope metrics are shown for comparison: linear fit m_ℓ (solid black line), quadratic fit m_q (solid red line), wave shape-based η/L' (dashed red line), and skewed-Gaussian fit m_{SG} (dotted black line). The onset of breaking is indicated by the vertical line in each panel.

series will always be denoted with subscript $-t$. Temporal peak-tracking methods sample the cross-shore LIDAR transect at discrete locations and use these time series to identify, track, and measure wave parameters (e.g., Martins et al., 2017b; Postacchini and Brocchini, 2014; Power et al., 2015). In effect, the LIDAR data are treated as a dense cross-shore array of elevation gauges. For comparison purposes, we show temporally-derived troughs, peaks, and wave heights for data sampled at a location mid-transect to ensure that both spatial and temporal wave peaks and troughs can be identified.

In Figure 2.10a, we see large scatter between temporal z_{tr-t} and spatial z_{tr-x}, with a root-mean-squared difference (rmsd) of 20 cm and a normalized rmsd (nrmsd) (normalized by the variance of the spatially-derived parameter) of 2.2. The mean bias is -4.8 cm, indicating that, on average, z_{tr-t} is lower than z_{tr-x}. These statistics suggest that the true trough elevation computed with z_{tr-x} is biased high and supports the use of the z_{tr-t} for calculating trough-to-peak wave height, H.
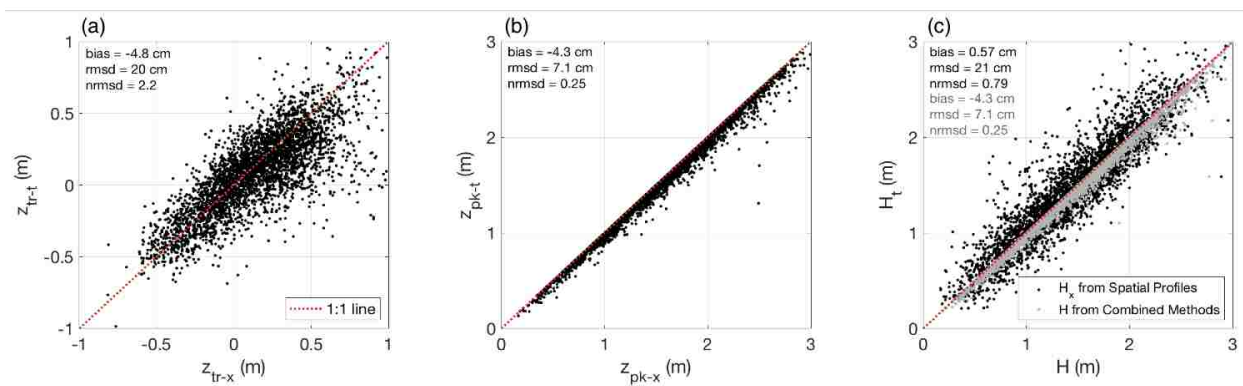
Figure 2.10: (a) Wave peak elevations and (b) wave trough elevations identified using the temporal peak-tracking method versus the spatial peak-tracking method, with 1:1 line for comparison. (c) Wave heights computed from the temporal peak-tracking method versus wave heights computed from the spatial peak-tracking method (black dots) and the combined spatio-temporal method (gray dots), with 1:1 line for comparison.

Comparing the spatially- and temporally-derived wave peak elevations in Figure 2.10b, we

find that the scatter between z_{pk-x} and z_{pk-t} is small, with an rmsd of 7.1 cm and an nrmsd of 0.25. Thus, the spatial peak-tracking methods agree well with the temporal methods. In Figure 2.10b, all points lie on or to the right of the 1:1 line, which indicates that all individual bias calculations $(z_{pk-t} - z_{pk-x})$ are zero or negative. The resulting mean bias is -4.3 cm. A negative bias is expected because the spatially-derived z_{pk-x} will always report the maximum surface elevation, while the temporally-derived z_{pk-t} may not always sample this value. When the temporal peak-tracking method samples at relatively sparse cross-shore locations (1-m spacing), the location through which the wave peak passed at a given time may occur between sample locations. The resultant bias theoretically approaches zero as the spacing between sampling points approaches zero. Benetazzo et al. (2017) quantified a similar difference between temporal and spatial sampling protocols, reporting that rogue waves are observed more frequently when searched for in space and time than when using time series alone.

Figure 2.10c compares wave height metrics. The y-axis shows the temporally-derived trough-to-peak wave height $H_t = z_{pk-t} - z_{tr-t}$, and the x-axis presents both the wave height used in our analysis, $H = z_{pk-x} - z_{tr-t}$, and a fully-spatial wave height, $H_x = z_{pk-x} - z_{tr-x}$. The rmsd (21 cm) for H_x relative to H_t is similar to that of z_{tr-x} relative to z_{tr-t}, but the nrmsd (0.79) and mean bias (0.57 cm) are lower because of the close agreement between z_{pk-x} and z_{pk-t}. The scatter and mean bias of H relative to H_t are small and almost identical to that of z_{pk-x} relative to z_{pk-t}. Since using z_{tr-x} severely limits our ability to calculate H across the full transect, and there is a relatively small and predictable bias (-4 cm) in H when z_{tr-t} is used in conjunction with z_{pk-x}, we conclude that $H = z_{pk-x} - z_{tr-t}$ is a valid metric of wave height.

2.4.2 Phase Speed

Figure 2.11 shows the broad distribution of wave speeds calculated using $\triangle x/\triangle t$ (black bars) and the narrower distribution of a smoothed version achieved by a 5-point moving regression (blue curve) for all non-breaking waves tracked from the LIDAR spatial profiles. Limiting our

comparison to non-breaking waves prevents natural wave speed variability due to breaking from confounding the method evaluation. Even with the reduction in variance achieved by the smoothed version, the wave speed c derived from the tracked LIDAR profile peaks (x_{pk}, t_{pk}) is still noisy, as illustrated by the solid line in Figure 2.9b. However, the skewed-Gaussian tracked peaks $(\tilde{x}_{pk}, \tilde{t}_{pk})$ provide a more smoothly varying wave speed estimate $\tilde{c}$ (dotted line in Figure 2.9b) via the same smoothing method. The overall variance of the wave speed distributions is also reduced, as shown by the red curve in Figure 2.11. The mean, mode, and standard deviation for c are 6.44 ms^{-1}, 5.85 ms^{-1}, and 2.23 ms^{-1}, respectively. For $\tilde{c}$, the mean and mode are not significantly different at 6.21 ms^{-1} and 5.75 ms^{-1}, respectively, and the standard deviation is slightly reduced to 1.72 ms^{-1}.
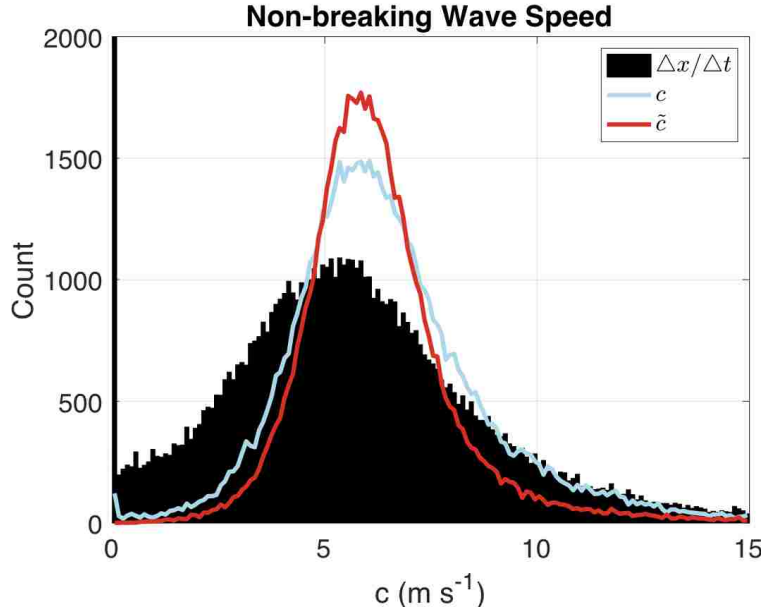
Figure 2.11: Wave speed estimated discretely (black bars), c via the 5-point regression method (blue curve) on peaks tracked in the interpolated LIDAR profiles (x_{pk}, t_{pk}), and $\tilde{c}$ from 5-point regression on the skewed-Gaussian fitted peaks $(\tilde{x}_{pk}, \tilde{t}_{pk})$.

Wave energy flux calculations require the mean energy transport velocity, called the group speed. Given shallow water linear wave theory assumptions, the group speed is approximately

equal to the individual wave phase speed. Dynamically, c represents the tracked peak speed, or crest speed, while $\tilde{c}$ represents the wave form speed. Of the two metrics, $\tilde{c}$ is the better metric to estimate phase speed. The ratio of crest speed and wave form speed ($c/\tilde{c}$) may be of interest for predicting wave breaking, similar to the way the ratio of crest speed to phase speed is used in models that resolve the free surface and water particle velocities (Zijlema et al., 2011).

2.4.3 Wave Slope

Similar to wave phase speed, wave slope can vary greatly depending on the chosen metric and the region of the wave face used to estimate slope. Of the four metrics defined in Section 2.3.1 and illustrated in Figure 2.9c, we will examine two here: the linear fit wave slope, m_ℓ, and the geometric wave slope, η/L'. Figure 2.12 shows how linear fit wave slope, m_ℓ, correlates to the geometric wave slope, η/L', as a function of the portion of the wave face included in the linear fit, and suggests a physical interpretation for this metric. The fitted region, for example the upper 50% of the wave face, is defined as the region of the wave that spans from x_{pk} to the cross-shore location where $z = z_{pk} - 0.5H$. Figures 2.12a-2.12d compare η/L' and linear fit slopes to the upper 20%, 50%, 80%, and 100% of the wave face, respectively, and include estimates from breaking and unbroken waves. The upper 20% of the wave face (Figure 2.12a) contains the steepest portions, of interest near the onset of breaking, but those regions are also highly variable (largest rmsd and nrmsd). Using the upper 50% of the wave face (Figure 2.12b) produces smaller bias and rmsd than the upper 20%, but the density plot shows many instances where m_ℓ is almost twice η/L'. The opposite trend is seen using the full wave face (Figure 2.12d). The cross-shore location of the wave trough is typically far from the wave peak, which results in a small m_ℓ and a negative bias. Based on the minimal scatter and bias reported in Figure 2.12c, we find that m_ℓ best estimates the geometric wave slope η/L' when the upper 80% of the wave face is included in the linear fit. The fit to this region is least susceptible to variability due to small shape changes near the crest and avoids bias due to curvature of the wave face near the trough.
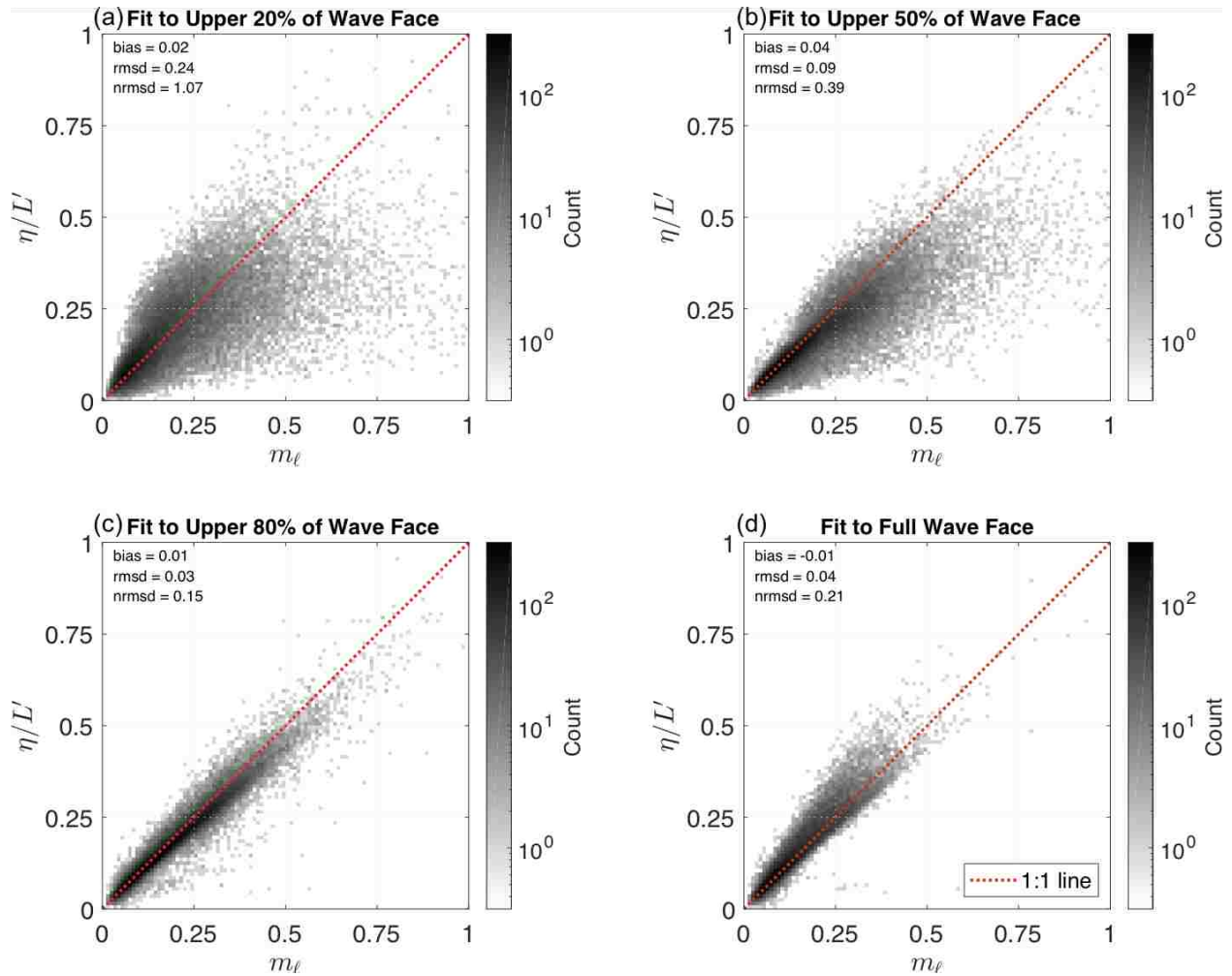
Figure 2.12: Density plots of the geometric wave slope, η/L', versus the linear fit wave slope, m_ℓ, as a function of the portion of the wave face included in the linear fit: (a) upper 20%, (b) upper 50%, (c) upper 80%, and (d) full wave face. The color bar indicates how many wave slope measurements reside in each bin, with a bin size of 0.01 for each variable. The 1:1 line is shown and the bias, rmsd, and nrmsd are reported in the upper left corner of each panel.

Table 2.1 reports characteristic percentiles of m_ℓ computed using the upper 80% of the wave face and segregated by wave type. For spilling and plunging breakers, these statistics include all stages: pre-onset, onset, and breaking. As expected, non-breaking waves exhibit the smallest wave slopes, and plunging breakers exhibit the largest wave slopes. Undetermined-type breakers, breakers whose onset was not observed by the pier IR camera, exhibit the next highest wave slopes, followed by spilling breakers.

Table 2.1: Percentiles for the linearly fit wave slope, m_ℓ, (in degrees) when fit to the upper 80% of the wave face.

Percentile	5th	25th	50th	75th	95th
Non-breaking waves	2.45°	4.56°	6.88°	10.12°	15.87°
Undetermined type breakers	6.68°	12.08°	15.62°	19.13°	25.58°
Spilling breakers	4.72°	8.34°	11.82°	15.73°	22.17°
Plunging breakers	7.37°	12.84°	16.45°	20.50°	27.46°

For breaking waves, m_ℓ can be more than twice the mean wave slopes previously used in nearshore wave energy models. For example, other slopes used and observed include, 12.6° (Duncan, 1981), 6° (Dally and Brown, 1995; Reniers and Battjes, 1997), 2.9° (Ruessink et al., 2001), and 4.6° (Carini et al., 2015). Some of the lower historical wave slopes were tuned to provide good agreement between the modeled and estimated bulk wave energy flux across the full surf zone for a range of wave conditions (Dally and Brown, 1995; Reniers and Battjes, 1997; Ruessink et al., 2001). Others were estimated from sea surface time series using assumptions of shallow water linear wave theory (Carini et al., 2015). The largest historical wave slope, 12.6°, was directly measured from photographs of spilling breakers in the laboratory by (Duncan, 1981) and agrees well with the 50th percentile of m_ℓ for spilling breakers (11.82°). Our results support more recent wave slope estimates, made directly from surf zone LIDAR profiles (Martins et al., 2018) or modeled and validated with laboratory data (Haller and Catalan, 2009), which range from 10° to 30°.

While the linearly fit wave slope (fit to the upper 80% of the wave face) is a straightforward and robust metric, it may not be appropriate for estimating slope for waves with large concavity. Near the onset of plunging, a higher order fitting function, such as a parabolic fit to the wave face, might better describe its curvature. The skewed-Gaussian wave-form fit is also a promising tool for tracking the steepening of a wave prior to breaking. Chapter 3 focuses on the evolution of wave parameters near the onset of breaking and includes analysis of the maximum gradient of the skewed-Gaussian fit, m_{SG}, and the quadratic fit wave slope, m_q, which are most appropriate for steep and nearly overturning spilling and plunging breakers.

2.5   Conclusions

This work presents detailed methodology for LIDAR and IR data fusion to track, measure, and classify breaking waves in the surf zone. We compare existing and new wave metrics for wave height, wave speed, and wave slope. A line-scanning LIDAR and two IR cameras were used to collect data of surf zone breaking waves at the US Army Corps of Engineers Field Research Facility (USACE FRF) in Duck, NC. The LIDAR and IR camera with wave-scale field of view were mounted to a mobile platform that was moved throughout the experiment to maintain coverage of the region where the onset of breaking occurred. This field deployment necessitated the development of an adaptive rectification protocol for the LIDAR data, and the resulting LIDAR data quality was objectively assessed based on wave analysis requirements.

Utilizing the full spatial and temporal resolution of the LIDAR data, we developed a peak-tracking algorithm that builds on techniques by Power et al. (2015), Martins et al. (2016), and Martins et al. (2017a). We track over 4200 individual waves. The surf zone-scale IR imagery is used to automatically identify candidate breakers using the thresholding detection algorithm from Carini et al. (2015). Those candidate breakers are manually reviewed using the higher resolution wave-scale IR imagery, and the breaker type is determined based on the unique thermal signatures of spilling and plunging breakers. The back face of spilling breakers exhibit an unorganized lacey pattern, while the back face of plunging breakers

exhibit an organized streaky pattern. Using these data fusion methods we detect the onset of breaking and classify breaker type for 524 spilling and plunging breakers.

Methods to automate the image-based wave classification, including machine learning techniques, are being investigated (paper in preparation with Dan Buscombe). The frontal nature of breaking waves and the repeated streaky or unorganized IR signatures associated with different breaker types are features that machine-learning algorithms can exploit, and unpublished results show that deep convolution neural networks classify breaker type from IR imagery with high skill.

We compute metrics of wave height, wave speed, and wave slope, on a wave-by-wave basis. Wave height, H, is calculated as the difference between the spatially-derived peak elevation and the temporally-derived trough elevation. Extracting peak elevations from the full spatial wave profiles guarantees that the true peak elevation of the wave is sampled, and extracting trough elevations from the times series (collocated with the tracked wave peaks) provides trough elevations even if the trough location is beyond the field of view of the LIDAR transect at the time the peak is observed. We compare H to H_t (computed using the time series alone) for context, and find good agreement with an rmsd of 7.1 cm, an nrmsd of 0.25, and the mean bias is -4.3 cm ($H_t \leq H$).

Computing wave speed with the LIDAR data, we find that variability is mitigated with a 5-point moving linear regression of the tracked peaks (t_{pk}, x_{pk}) and provides a more robust estimate of wave phase speed than discrete point-to-point differentiation, $\triangle x / \triangle t$. The 5-point regression methods reduces the variance of the estimated instantaneous wave speed, c, from 8.7 m^{2}s^{-2} (discrete method) to 4.4 m^{2}s^{-2}. We note that the instantaneous tracked wave speed c can be quite variable, and a smoother metric would be beneficial for future estimation of wave energy flux across the surf zone. The skewed-Gaussian method does not significantly change the mean and mode of the wave speed distribution (Figure 2.11), but it does further reduce the variance to 3.0 m^{2}s^{-2}.

Using a linear fit to the upper 80% of the wave face yields a robust estimate of wave slope that correlates strongly with the geometric wave slope, η/L' (Figure 2.5b). The resulting

median wave slopes are 6.88° for non-breaking waves, 11.82° for spilling breakers, 15.62° for breakers of undetermined type, and 16.45° for plunging breakers (Table 2.1), which agree with recent surf zone LIDAR-based wave slope estimates by Martins et al. (2018). Plunging breakers exhibit the steepest linear-fit wave slopes (27.5° at the 95th percentile), though a quadratic fit or skewed-Gaussian fit wave slope may be more appropriate as the concavity increases near the onset of breaking. In Chapter 3, we examine the evolution of wave slope and other geometric and kinematic wave parameters through pre-onset, onset, and developing breaking stages.

Chapter 3

GEOMETRY & KINEMATICS

3.1 Introduction

Understanding the dynamics of breaking waves in the surf zone is vital to the progress of nearshore wave and circulation models towards real-time operational use. The goal of wave models in coastal regions is to capture relevant physical processes through explicit representation or field-validated parameterizations. Phase-resolving models, such as Simulating WAves till SHore or SWASH (Zijlema et al., 2011), are time-dependent and conserve mass and momentum at a discrete level. In SWASH, the sea surface elevation is modeled in space and time, which allows for breaking criteria, such as a critical wave speed or wave steepness, to be assessed on a wave-by-wave basis and for wave shape changes to be tracked as breakers develop. Phase-averaged models, such as Simulating WAves Nearshore or SWAN (Booij et al., 1997), operate using a spectral action balance equation. In SWAN, energy dissipation due to wave breaking is parameterized using the Battjes and Janssen (1978) bore model, which determines the portion of the wave height spectra that breaks using the breaker parameter $\gamma = H/h$, the ratio of wave height to water depth. Phase-resolving models are often used for basic research about wave mechanics and as input for phase-averaged models, which are larger scale and used for predictive and hind-cast projects.

Traditionally, γ is estimated as a bulk statistic, using the significant wave height, H_s, or the root-mean-squared wave height, H_{rms}, and the mean water depth, $\bar{h}$. For example, Sallenger and Holman (1985) found $0.32 < \gamma_{rms} < 0.42$ in the inner surf zone and $0.4 < \gamma_{rms} < 0.8$ seaward of a shore-parallel sandbar at Duck, NC, the site of this current study. Both Sallenger and Holman (1985) and Raubenheimer et al. (1996) found that γ is not correlated with offshore wave steepness, the ratio of deep water wave height to deep water

wavelength H_0/L_0, but γ is positively correlated with local beach slope, β. Apotsos et al. (2008) tested empirical and modeled formulations for bulk γ from Thornton and Guza (1983), Battjes and Janssen (1978), Lippmann et al. (1996), Janssen and Battjes (2007), Baldock et al. (1998), and Whitford (1988) against field data collected at three different sites (Duck, NC, La Jolla, CA, and the Netherlands) and found that no universal value predicts breaking on all beaches. After tuning γ to optimize model performance across the three beaches, mean γ varied between 0.2 and 0.66 (Apotsos et al., 2008). When γ is modeled on a wave-by-wave basis the range increases to include $0.6 < \gamma < 1.4$ (Chella et al., 2015).

There are very few studies of γ for individual waves in the field. Suhayda and Pettigrew (1977) analyzed 10 plunging breakers at Rockley Beach, Barbados, and found that γ increased as the waves approached the breakpoint and decreased following the onset of breaking. At Virginia Beach, Weishar and Byrne (1978) tracked 116 waves and found $\gamma = 0.78$ on average, but that there was a significant difference between γ for plunging and non-plunging breakers.

This chapter analyzes γ on a wave-by-wave basis for a large dataset to investigate reasons why γ varies widely across different beaches and even at a single beach. Given that γ is often correlated with parameters used to predict breaker type, such as beach slope and wave steepness, it is reasonable to suggest that γ varies with breaker type. To that end, the relationships between γ, beach slope, wave steepness, and breaker type are investigated. First, we briefly summarize the methods used to track and classify breakers in the surf zone using LIDAR line-scans and IR imagery (see Chapter 2 for details). Second, results are presented from spatial analysis of key wave parameters near the onset of breaking, specifically, the breaker parameter $\gamma = H/h$, wave face slope, and wave phase speed. Third, the predictive capabilities of γ, wave face slope, and the Miche steepness criteria are explored. Last, we conclude with a discussion of the implications of our results for nearshore wave models.

3.2 Methods

3.2.1 Field Experiment

A detailed account of the field experiment setup and instruments can be found in Chapter
2. Briefly, LIDAR and thermal infrared (IR) remote sensing data of surf zone breaking
waves were collected on 07-08 November 2016 at the US Army Corps of Engineers Field
Research Facility (USACE FRF) in Duck, NC. A line-scanning LIDAR and an IR camera
were deployed on a mobile platform on the FRF pier that was repositioned as needed to
maintain observation of the region in which breaking initiated. 3.1 illustrates the bathymetry
for the cross-shore extent of the data collected when the platform was positioned at $x = 148$
m on 07 November (referred to as the onshore transect) and moved to $x = 190$ m on 08
November (referred to as the offshore transect). The LIDAR scanned 30-40 m in the cross-
shore direction at 5.2 Hz, from approximately 13 m above mean sea level. The IR camera
was deployed at the same height, collected frames at 10 Hz, and viewed the sea surface at
a 45° incidence angle. To capture a surf zone-scale field of view, a second IR camera was
mounted 27.8 m above mean sea level on the FRF imaging tower, pointed offshore. This
camera sampled at 5 Hz and viewed the sea surface at a 75° incidence angle. All fields of view
overlapped to facilitate data fusion, and each data source was transformed to the local FRF
coordinate system (positive x offshore, positive y northward along-shoreline, positive z up
and referenced to NAVD88). Data was collected during two rising-high tide intervals. For the
first sampling period (07 Nov), the FRF AWAC (Acoustic Wave And Current profiler) in 3.5
m water depth reported that the significant wave height was 2.0 m and the peak wave period
was 7.5 s. For the second sampling period (08 Nov), the significant wave height increased to
2.3 m and the peak wave period lengthened to 14.5 s. Bathymetry surveys were conducted
on 03 and 16 November, and a time-weighted interpolated bathymetry was computed for
07-08 November, shown in Figure 3.1. The validity and implications of the interpolated
bathymetry are discussed in Appendix A and in Section 3.2.3 below, respectively.
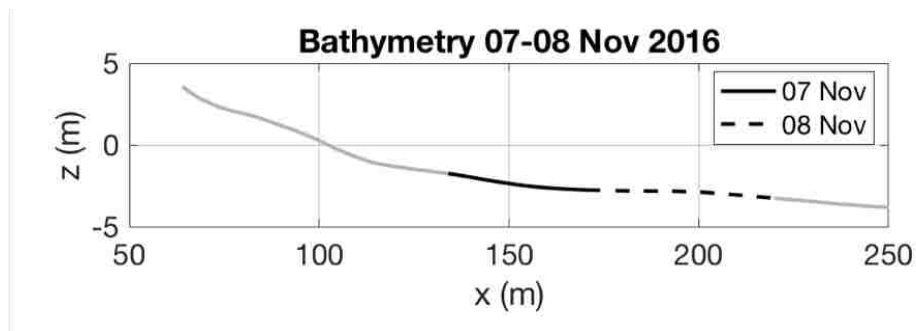
Figure 3.1: Time-weighted interpolated bathymetry (solid gray line) used for analysis of the data on 07-08 November. The LIDAR and IR camera deployed from the FRF pier collected data that spanned x=135-175 m (solid black line) on 07 November and x=175-215 m (dashed black line) on 08 November.

3.2.2 Breaker Classification

An automated breaker detection algorithm Carini et al. (2015) is used on the surf zone-scale IR imagery to identify candidate breakers traveling along the LIDAR transect. For each candidate breaker, the wave-scale IR imagery is then used to manually determine the onset of breaking and classify breaker type. For spilling breakers, the onset of breaking is defined as the moment active foam is first detected on the wave face. For plunging breakers, the onset of breaking is defined as the moment the wave crest begins to overturn. The breaker type is classified based on the unique thermal signatures of spilling and plunging breakers, shown in Figure 3.2. Along the back face of the wave, spilling breakers exhibit an unorganized patchy texture, while plunging breakers exhibit an organized streaky pattern. If the onset of breaking occurred offshore of the wave-scale IR camera's FOV, then the breaker type is classified as undetermined.

3.2.3 Wave Parameter Estimation

From the LIDAR line-scans, over 4200 individual waves are tracked using the spatial peak-tracking method described in Chapter 2. Figure 3.3a shows a sequence of three wave profiles
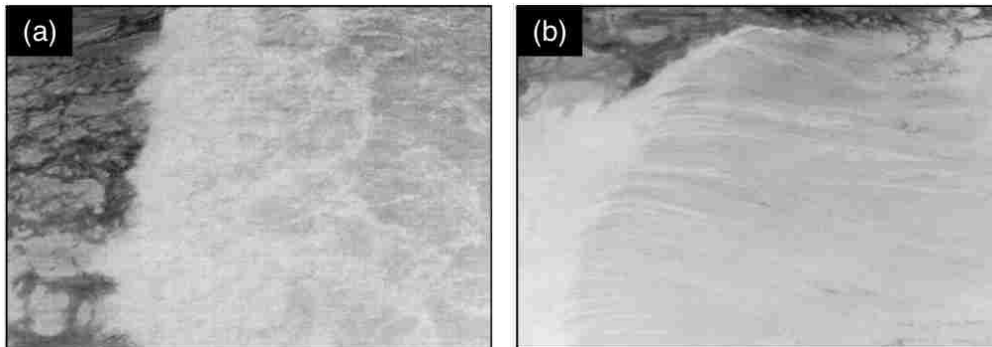
Figure 3.2: Unique thermal IR signatures of (a) spilling breakers and (b) plunging breakers, shown by the wave-scale IR imagery used to classify breaker type.

from an example breaking wave. The profiles have been centered on mean sea level, and the tracked peaks are marked. The active foam identified in the surf zone-scale IR imagery is overlaid in gray on the front face of each wave profile. Additionally, each LIDAR wave profile is fit with a skewed-Gaussian (SG) function to provide peak locations that are robust to sea spray and rapid wave shape changes.

Wave height is computed as the difference in elevation between the spatially-tracked wave peak and temporally-tracked wave trough, $H = z_{pk} - z_{tr}$. The water depth through which a wave travels is computed as the difference between the measured mean sea level and the interpolated bathymetry at the location of the wave peak, $h = z_{MSL} - z_{bathy}(x_{pk})$. Using H and h, we estimate instantaneous breaker parameter $\gamma = H/h$ (Figure 3.3b). Several metrics of wave face slope are presented in Chapter 2. In the current analysis, we focus on the quadratic-fit wave slope, θ_q, defined as the maximum slope achieved along the wave face by the parabola fitted to the upper 80% of the wave face (Figures 3.3a and 3.3c). This wave slope metric is particularly useful for waves near the onset of breaking whose wave face may display some degree of concavity. Wave slope may also be estimated as the maximum slope achieved by the SG fitted profiles along the upper 80% of the wave face, θ_{SG} (Figure 3.3c). As detailed in Chapter 2, the SG fitted profile peaks provide a more robust estimate of wave
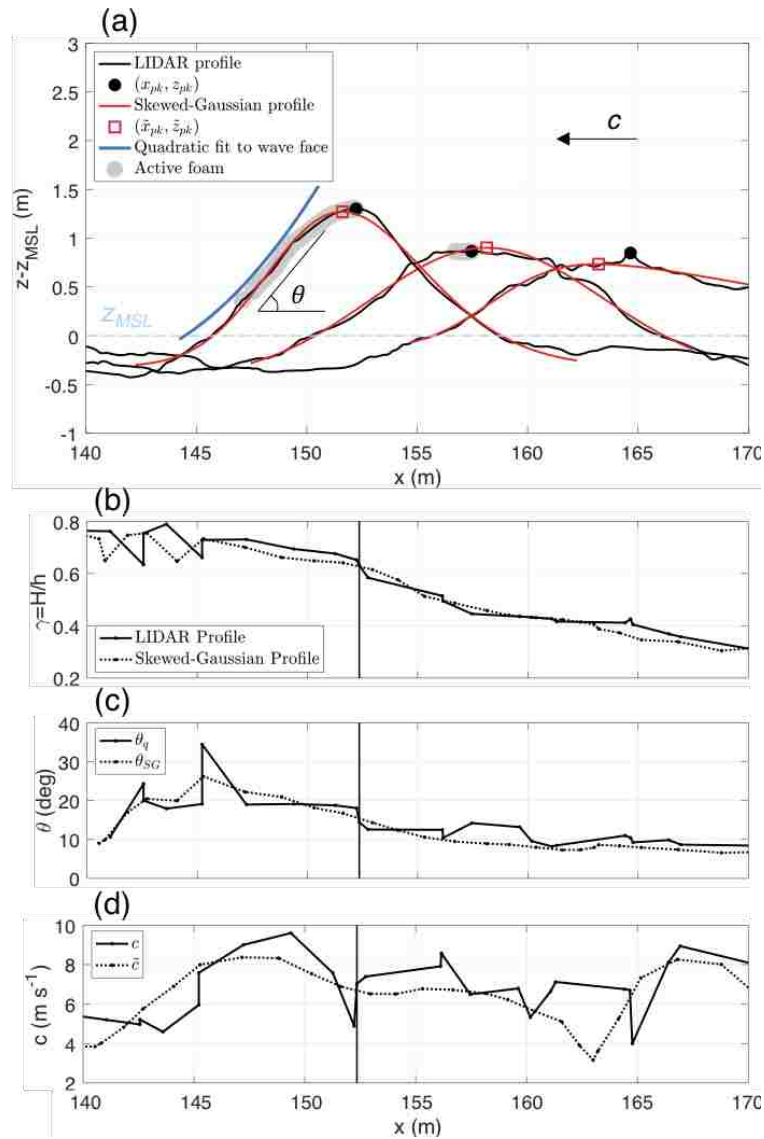
Figure 3.3: (a) Three LIDAR profiles (black curves) from a tracked breaking wave, with skewed-Gaussian fitted wave profiles (red curves) overlaid. The wave progresses from right to left as indicated by the wave speed arrow and the profiles have been centered on mean sea level, z_{MSL} (light blue dashed line). Wave slope θ is illustrated by an angle and a representative quadratic fit to one wave face (dark blue curve). Example tracked (b) γ, (c) wave slope, and (d) wave speed estimated from the LIDAR profiles (solid black line) and the SG fitted profiles (dotted black line). These parameters correspond to the same example wave shown in (a). The vertical line represents the breakpoint.

speed than using the raw LIDAR-tracked wave peaks. Therefore, the instantaneous wave speed presented in this analysis is defined from the SG profiles and denoted $\tilde{c}$ (Figures 3.3d and 3.3h). Wavelength is estimated as $L = \tilde{c}T$, where T is the trough-to-trough wave period from the time series extracted at the location of the tracked wave peak.

We note that the interpolated bathymetry has a significant impact on h, and thus also on γ. Appendix A shows that the time-weighted interpolated bathymetry agrees reasonably with the depth profiles estimated by inverting solitary wave theory using the measured wave speeds. The depth-inversion from solitary wave theory is not taken as our bathymetry, because we do not want to introduce a dependence between γ and measured wave speeds for our analysis.

3.3 Results

3.3.1 γ Distributions & Cross-shore Statistics

As a first order assessment of γ, Figure 3.4 presents a hierarchy of γ histograms. Each histogram is normalized by its population total and scaled by the bin width to create a probability distribution function (PDF) of γ, and all γ PDFs are well-fit by a Gaussian distribution. Figure 3.4a shows the γ-distribution for all tracked waves ($N = 4290$), with a mean and standard deviation of 0.49 and 0.27, respectively. The next tier segregates waves into three categories: non-breaking waves (Figure 3.4b), onset-observed breakers (Figure 3.4c), and breakers of undetermined type (Figure 3.4d). The γ-distribution for non-breaking waves ($N = 2627$) closely resembles that for all waves, but exhibits a smaller mean γ of 0.40. The mean γ for breakers whose onset was observed ($N = 524$) is 0.67, the largest mean γ for this tier, and the mean γ for undetermined type breakers ($N = 1139$) is slightly lower at 0.60. Investigating only those waves whose onset was observed in the wave-scale IR imagery (Figures 3.4e and 3.4f), we find that the mean γ is smaller for spilling breakers ($N = 413$) than for plunging breakers ($N = 111$), with values of 0.65 and 0.75, respectively.

Next, we examine the cross-shore evolution of the bin-averaged wave-by-wave γ for
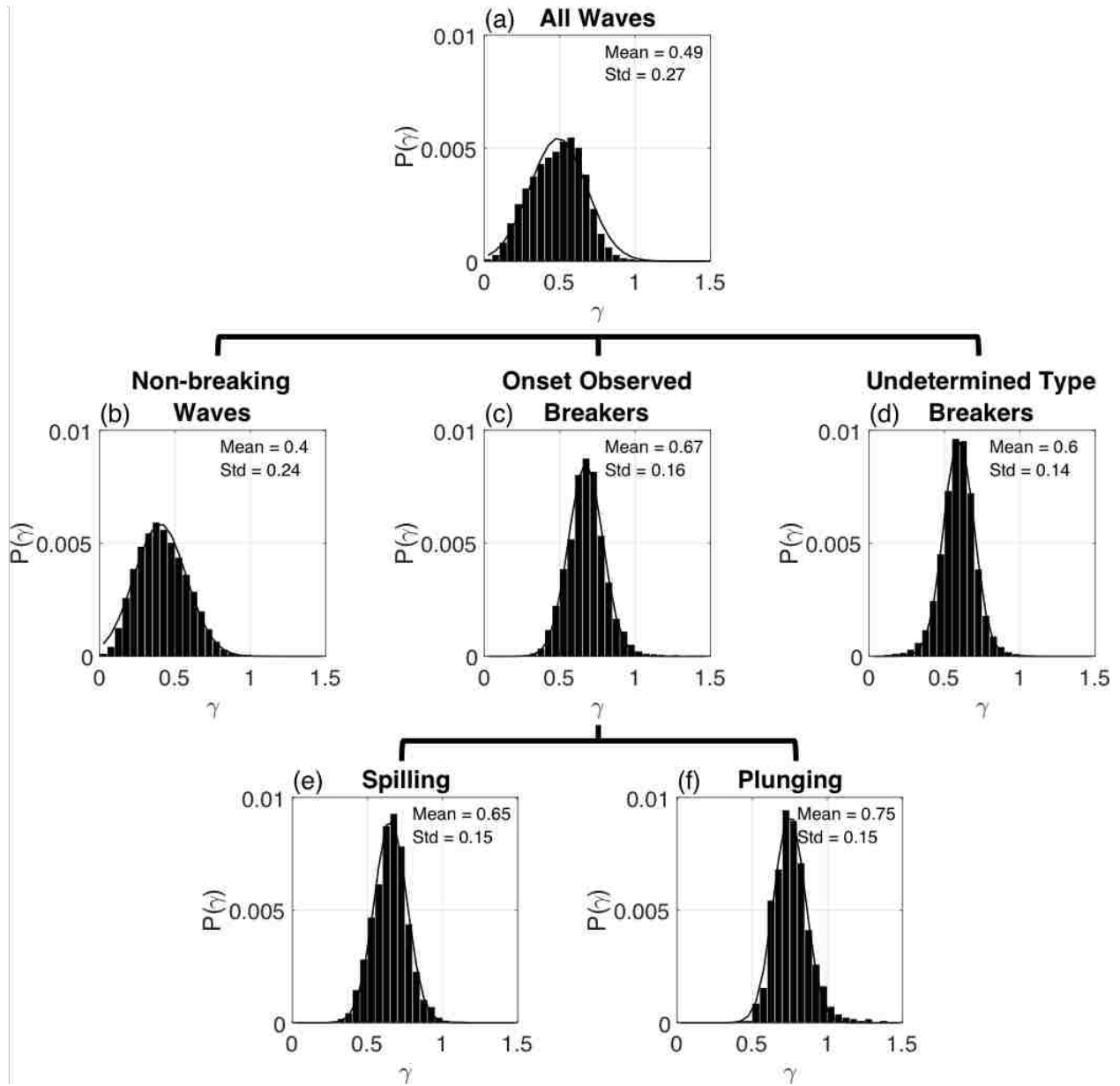
Figure 3.4: Hierarchy of normalized histograms P(γ) for (a) all waves, (b) non-breaking waves, (c) onset-observed breakers (includes both spilling and plunging), (d) undetermined type breakers, (e) spilling breakers, and (f) plunging breakers. Mean and standard deviation of the fitted Gaussian distribution (thin black curve) are reported within each subplot.

each breaker type and compare with the traditional statistically-defined $\gamma_s = H_s/h$ and $\gamma_{rms} = H_{rms}/h$, where H_s and H_{rms} are the significant and root-mean-squared wave heights, respectively. Figure 3.5 shows bin-averaged γ as a function of cross-shore position for non-breaking, spilling, plunging, and undetermined type breakers. For spilling and plunging breakers, only data from the onset and developing stages of breaking are included (pre-onset excluded). The standard deviation of each population was relatively constant, therefore only representative standard deviation bars are shown for clarity. γ_s and γ_{rms} were calculated every two meters using the sea surface elevation time series and water depth at each location.
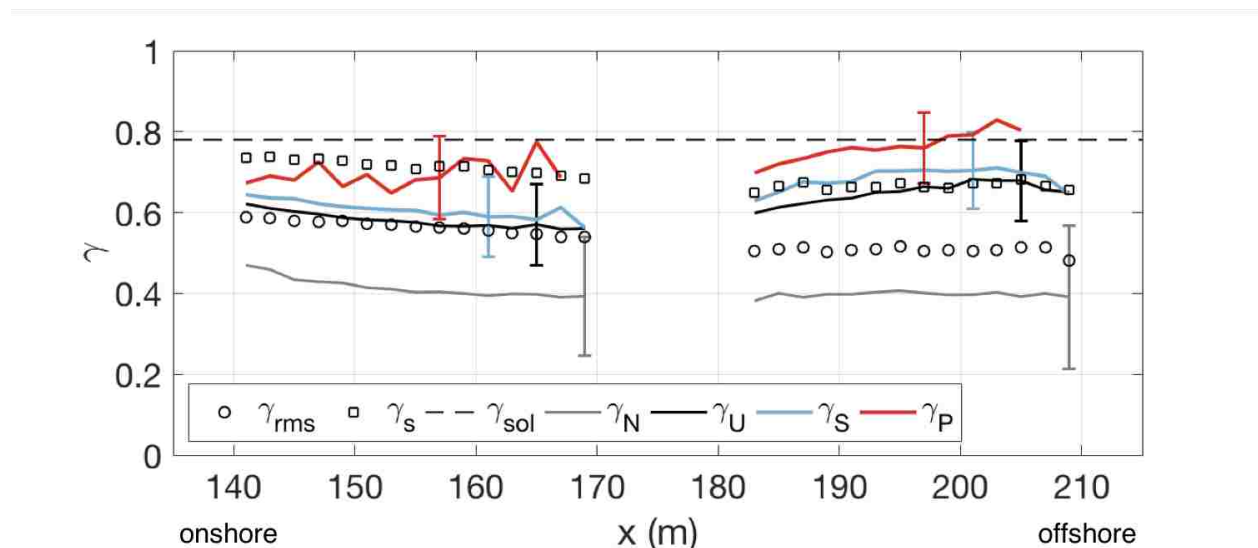
Figure 3.5: Bin-averaged γ, with representative standard deviation bars, as a function of cross-shore location for non-breaking waves γ_N (light gray), spilling breakers γ_S (blue), plunging breakers γ_P (red), and undetermined type breakers γ_U (black). $\gamma_r ms$ (circles) and γ_s (squares) estimated every two meters along the sample transects.

The onshore and offshore transects in Figure 3.5 show different cross-shore evolution of γ. For the onshore transect, γ_P for plunging breakers are approximately equal to γ_s near 160 m$< x <$170 m ($\gamma_P \approx 0.75$) and decreases slightly as breakers approach the shoreline ($\gamma_P < 0.70$). Undetermined type breaker γ_U and γ_S gradually increase from about 0.58

to 0.62, following γ_{rms}. For the offshore transect, γ_P is greater than γ_s across the entire transect, peaking at 0.82 and decreasing shoreward to about 0.70. γ_S and γ_U again exhibit similar behavior, this time matching γ_s, rather than γ_{rms}, at values between 0.65 and 0.68. For non-breaking waves, γ_N lies below all other estimates and is approximately constant at 0.40 from the offshore to onshore transect until $x <$155 m, when γ_N increases slightly to 0.47.

In nearshore wave models, the critical γ value derived from solitary wave theory, $\gamma_{sol} = 0.78$, is often employed to trigger breaking in the surf zone. Non-breaking waves, spilling breakers, and undetermined type breakers all maintain a mean γ less than γ_{sol} across the surf zone, though the distributions of γ for spilling and undetermined type breakers do contain some values above this limit for the offshore transect. Bin-averaged γ_P exceeds γ_{sol} for $x >$198 m and briefly at $x=$165 m. While the cross-shore, bin-averaged γ_S and γ_P mirror the type of information included in nearshore wave models, averaging based on cross-shore position obscures maximum γ values that may be achieved near the onset of breaking.

3.3.2   Evolution of γ, θ, and c Near the Onset of Breaking

To examine the evolution of γ about the breakpoint for spilling and plunging breakers we create ensemble-averaged wave profiles. Figure 3.6, shows wave-by-wave γ as a function of cross-shore position (see example in Figure 3.3c), centered on the location of the onset of breaking, x_b, and normalized by the wavelength, L. The shaded bands represent 95% of the raw data, which is bin-averaged and displayed with 95% confidence intervals on the mean. The data presented in Figure 3.6a was collected on 07 November at $x = 135 - 175$ m during a rising tide from $z_{MSL} =$0.15 m to $z_{MSL} =$0.65 m over a beach slope $0.02 < \beta < 0.04$, with $H_s = 1.8$ m and $T_p = 7.3$ s. The data in Figure 3.6b was collected on 08 November at $x = 185 - 220$ m during a rising tide from $z_{MSL} =$0.06 m to $z_{MSL}=$0.63 m over a beach slope $0 < \beta < 0.02$, with $H_s = 2.2$ m and $T_p = 14.0$ s. It should be noted that the shorter normalized cross-shore extent of measurements for 08 Nov than 07 Nov is mostly due to the longer wave periods (longer wavelengths) observed on that day.

Regardless of breaker type or location of the transect within the surf zone, γ increases to a maximum or peak at the onset of breaking. For the onshore transect, γ reaches a maximum of 0.63 for spilling breakers and 0.73 for plunging breakers at the onset of breaking. For spilling breakers, this peak γ is maintained as the breakers develop. For plunging breakers, γ is more variable during breaker development, because the tracked wave heights are variable due to the drastic shape changes, secondary plunging events, and splash up that are typical of plunging breakers. However, γ_P does gradually approach γ_S within one wavelength of the breakpoint. Using a two-sided t-test, we find that γ_S and γ_P are statistically different at the 95% confidence level within one-half wavelength (in both directions) of the breakpoint. For the offshore transect, γ peaks at 0.71 for spilling breakers and 0.81 for plunging breakers at the onset of breaking and then decreases as breaking develops. Based on the two-sided t-test at 95% confidence level, γ_S and γ_P are only statistically different within one-quarter wavelength of the breakpoint.

The onshore and offshore γ values for spilling breakers are statistically different (same t-test as noted above) across the full normalized transect. The onshore and offshore γ values for plunging breakers are statistically different, but not as strongly as the spilling breakers. γ_P is most different between onshore and offshore transects within one-quarter wavelength of the breakpoint. Overall, the range of γ observed for both spilling and plunging breakers (gray shaded regions in Figure 3.6) includes values greater than $\gamma_{sol} = 0.78$, even though ensemble-averaged γ only exceeds γ_{sol} for plunging waves observed along the offshore transect.

Other geometric and kinematic wave parameters of interest near the onset of breaking include wave face slope and phase speed. Figure 3.7 presents wave slope estimated using the quadratic-fitting method, θ_q, for spilling and plunging breakers in the same manner as Figure 3.6. For the onshore transect (Figure 3.7a), θ_q increases to a peak just after the onset of breaking, with plunging breakers achieving steeper slopes than spilling breakers (θ_q equals 30° and 22°, respectively). Spilling breakers maintain their maximum wave slope as they develop, while plunging breaker wave slope initially decreases and then becomes highly variable. The differences observed within one-quarter wavelength of the breakpoint
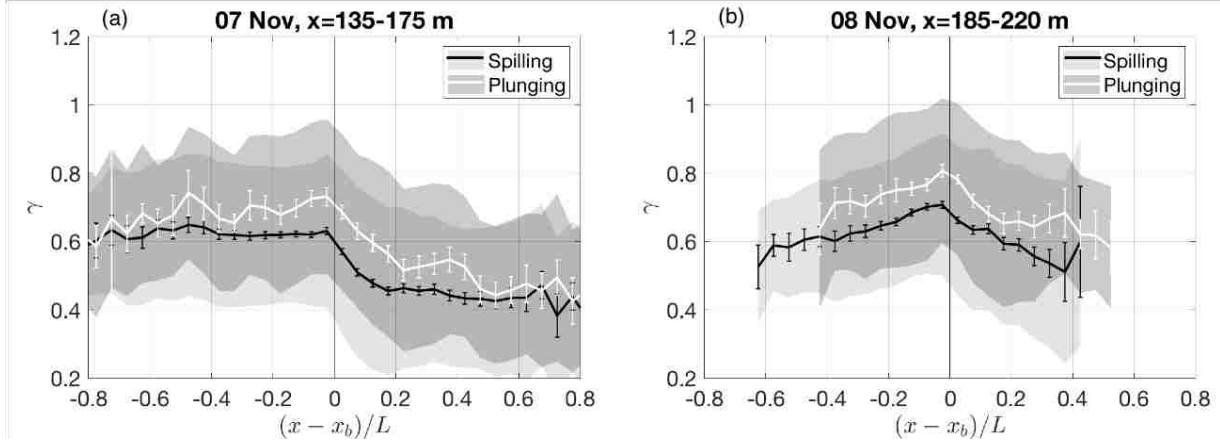
Figure 3.6: Evolution of γ for spilling (black lines) and plunging (white lines) breakers as a function of normalized cross-shore position relative to the breakpoint for data collected on (a) 07 Nov and (b) 08 Nov. See text for full description of wave conditions. Positive $(x - x_b)/L$ indicates before the onset of breaking and negative $(x - x_b)/L$ indicates after the onset of breaking. The shaded regions represent 95% of the data, and the solid lines are the bin-averaged values with 95% confidence intervals.

are statistically significant at the 95% confidence level, based on a two-sided t-test. Unlike γ, θ_q exhibits similar evolution for the onshore and offshore (Figure 3.7b) transects, though spilling breakers achieve slightly steeper wave slope just after onset ($\theta_q = 25.5°$).

Finally, we examine the evolution of wave speed about the breakpoint. Figure 3.8 presents wave speed, $\tilde{c}$, estimated using the skewed-Gaussian fitted profiles as a function of normalized cross-shore coordinate. Wave speed peaks just after the onset of breaking for both spilling and plunging breakers. Using a two-sided t-test at 95% confidence level, we find that there is no statistically significant difference between spilling $\tilde{c}$ and plunging $\tilde{c}$ for the onshore or offshore transects. However, for a given breaker type, $\tilde{c}$ is statistically different within approximately one-third wavelength of the breakpoint for the onshore and offshore transects. For the onshore transect, the peak $\tilde{c}$ lies between 6.8 m s^{-1} and 7.2 m s^{-1}. For the offshore transect, the maximum wave speed increases to 7.3 m s$^{-1} < \tilde{c} <$ 7.6 m s^{-1}.
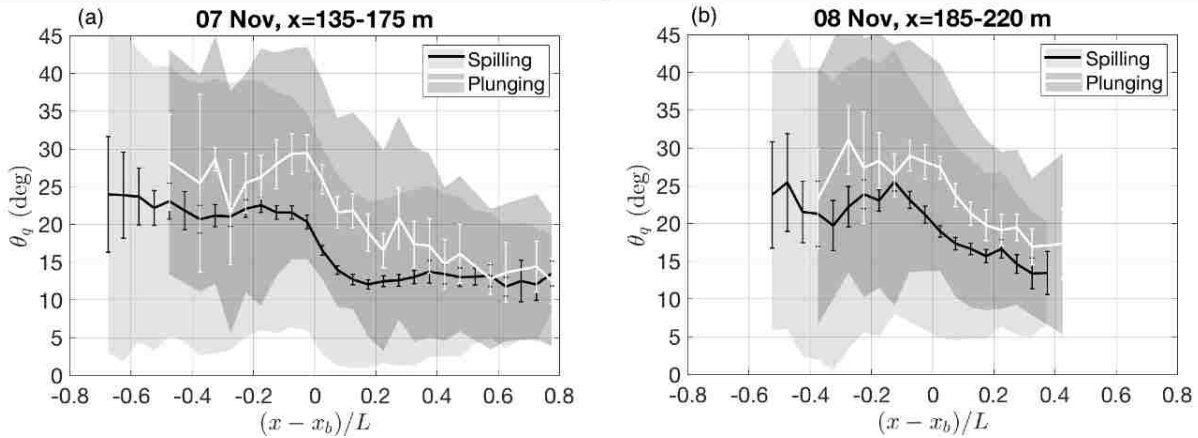
Figure 3.7: Evolution of quadratic-fit wave face slope, θ_q, for spilling (black line) and plunging (white line) breakers observed on (a) 07 November and (b) 08 November. Same x-axis scaling and data representation as in Figure 3.6.
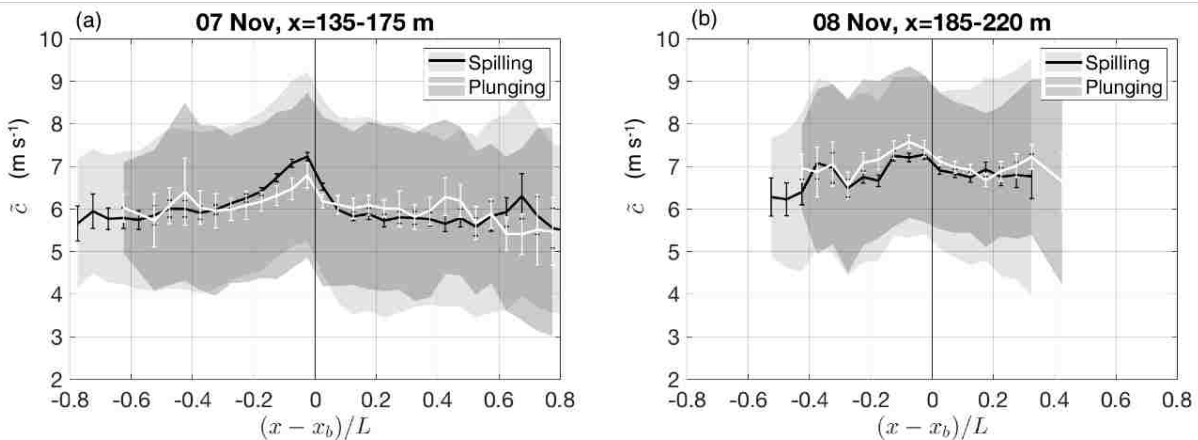
Figure 3.8: Evolution of the wave speed, $\tilde{c}$ (m s^{-1}), for spilling (black line) and plunging (white line) breakers observed on (a) 07 November and (b) 08 November. Same x-axis scaling and data representation as in Figure 3.6.

3.4 Discussion

3.4.1 Predicting Breaking & Breaker Type

Combining the information from Figures 3.6 and 3.7, we investigate the relationship between the steepening of the wave slope and the increase in γ that occurs as waves shoal to their breakpoint. Within the γ and θ_q parameter space, we define the 2D probability of observing a non-breaking or breaking wave as the relative prevalence of non-breaking and breaking wave observations at each (θ_q, γ) value pair, shown in Figure 3.9a. Non-breaking waves occupy the region of small θ_q and low γ, and breaking waves are most prevalent for large θ_q and high γ.
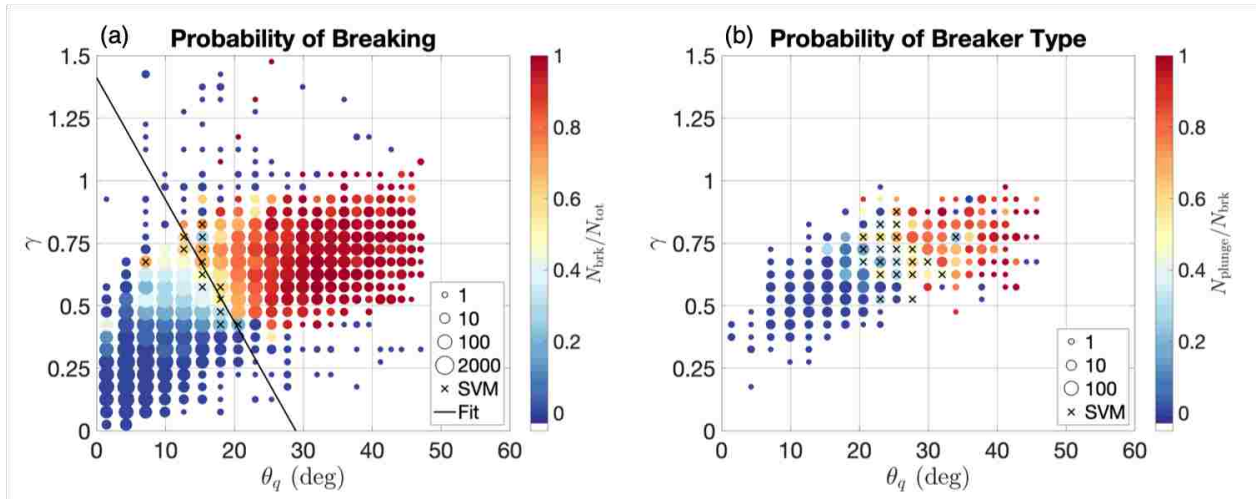
Figure 3.9: Probability (color) of (a) wave breaking (as opposed to not breaking) and that the breaker is (b) a plunging breaker (as opposed to a spilling breaker) for a given (θ_q, γ) pair. Point size is scaled by number of observations. The crosses mark the Support Vector Machine (SVM) modeling results that identify the transition between non-breaking and breaking observations or spilling and plunging observations. The black line in (a) is a linear fit to the support vector points: $\gamma = -0.049\theta_q + 1.41$.

A transition region, where there is roughly equal probability of observing a non-breaking or breaking wave, spans a parameter space where $10° < \theta_q < 20°$ and $0.45 < \gamma < 0.8$. Support Vector Machine (SVM) modeling is a form of machine-learning that can be used

Table 3.1: Linear regression model for predicting breaking: $y\ x_1 + x_2 + x_1 x_2$, Number of observations: 348, Error degrees of freedom: 345, Root Mean Squared Error: 0.329, Critical t-value at 95% and 99% confidence levels: 1.645 and 2.326

Predictor	Estimate	SE	t-stat	p-value
θ_q	0.013	0.002	7.0	1.27e-11
γ	-0.079	0.058	-1.4	0.18
$\theta_q \gamma$	0.013	0.003	4.2	3.70e-05

to define a binary classification based on a low or moderate number of predictors. Here, we use γ and θ_q as two predictors of the binary classifications of non-breaking or breaking. Non-breaking is defined as $N_{\mathrm{brk}}/N_{\mathrm{tot}} < 0.5$, and breaking is defined as $N_{\mathrm{brk}}/N_{\mathrm{tot}} \geq 0.5$. SVM modeling can also include a weighting function, here computed as the product of $N_{\mathrm{brk}}/N_{\mathrm{tot}}$ and the number of samples for each bin. Only bins containing at least 10 samples are included in the SVM model. The resulting transition region (support vector), marked by crosses in Figure 3.9a, is then fit with a line, using a robust fitting method that excludes outliers. For the transition from non-breaking to breaking, the linear fit yields $\gamma = -0.049\theta_q + 1.41$. The 95% confidence bounds on the slope and intercept are (-0.067, -0.031) and (1.13, 1.69), respectively.

Finally, to assess the predictive power of γ, θ_q, and the combination of the two parameters, a multivariate linear regression is performed of the type $y\ x_1 + x_2 + x_1 x_2$, where x_1 is θ_q and x_2 is γ. Table 3.1 shows that, based on both the p-value and t-test, θ_q alone is most predictive of breaking. The product of θ_q and γ is also a significant predictor, but γ alone is not a significant predictor of breaking.

Using only the breaking wave data, Figure 3.9b reports the probability of observing a spilling or plunging breaker for a given (θ_q,γ) pair. Spilling breakers mostly occupy the smaller wave face slopes and lower γ values, and plunging breakers occupy the larger wave face slopes and higher γ values.

Table 3.2: Linear regression model for predicting breaker type: y $x_1 + x_2 + x_1x_2$, Number of observations: 161, Error degrees of freedom: 158, Root Mean Squared Error: 0.246, Critical t-value at 95% and 99% confidence levels: 1.645 and 2.326

Predictor	Estimate	SE	t-stat	p-value
θ_q	0.002	0.004	0.59	0.56
γ	-0.327	0.083	-4.0	1.11e-04
$\theta_q\gamma$	0.031	0.005	6.0	1.16e-08

While the classification of spilling and plunging is discrete, breaker type is defined along a continuum as evidenced by the overlap of the regimes where there is equal likelihood of observing a spilling or plunging breaker. This transition occurs for $22° < \theta_q < 28°$ and $0.50 < \gamma < 0.85$. Defining spilling as $N_{\mathrm{plunge}}/N_{\mathrm{brk}} < 0.5$ and plunging as $N_{\mathrm{plunge}}/N_{\mathrm{brk}} \geq 0.5$, SVM modeling is performed using bins containing at least five samples. The resulting transition region (support vector) is marked by crosses in Figure 3.9b. While it appears reasonable to distinguish spilling from plunging breakers by drawing a nearly vertical line through the support vector points, they are not well-fit by a line. Again, a multivariate linear analysis is performed to assess the predictive power of γ, θ_q, and the combination of the two parameters. Table 3.2 shows that the combination of θ_q and γ is the most predictive of breaking. γ alone is also a significant predictor, but θ_q alone is not a significant predictor of breaking.

In addition to the direct measurement of wave face slope, we estimate a local wave steepness, H/L, to test the Miche criteria, which predicts breaking at a critical steepness when $H_b/L_b \geq 1/7 \tanh(k_b h_b)$ (Miche, 1944). To our knowledge, this is the first field verification of the Miche breaking criteria for depth-limited breaking in the surf zone. Figure 3.10 shows a density plot of H/L versus $\tanh(kh)$, created using parameter estimates from every instant each non-breaking wave was tracked. The values at the onset of breaking for each spilling and plunging breaker are overlaid and a linear fit to each breaker type is computed. The slopes

of the linear fit to onset spilling and plunging breakers are 0.111 and 0.124, respectively, and are smaller than the Miche steepness limit of 0.143. The density map of non-breaking waves confirms that 99.0% of non-breaking waves fall below the steepness limit from Miche, 95.5% fall below the limit estimated from onset plunging breakers, and 90.5% fall below the limit estimated from onset spilling breakers. We note that L and k are both estimated from measured $\tilde{c}$ and T, and thus introduce correlation between the independent and dependent axes. Nevertheless, this correlation does not overwhelm the signal, as evidenced by the non-breaking waves, which lie well below the Miche limit and cover a range of values.
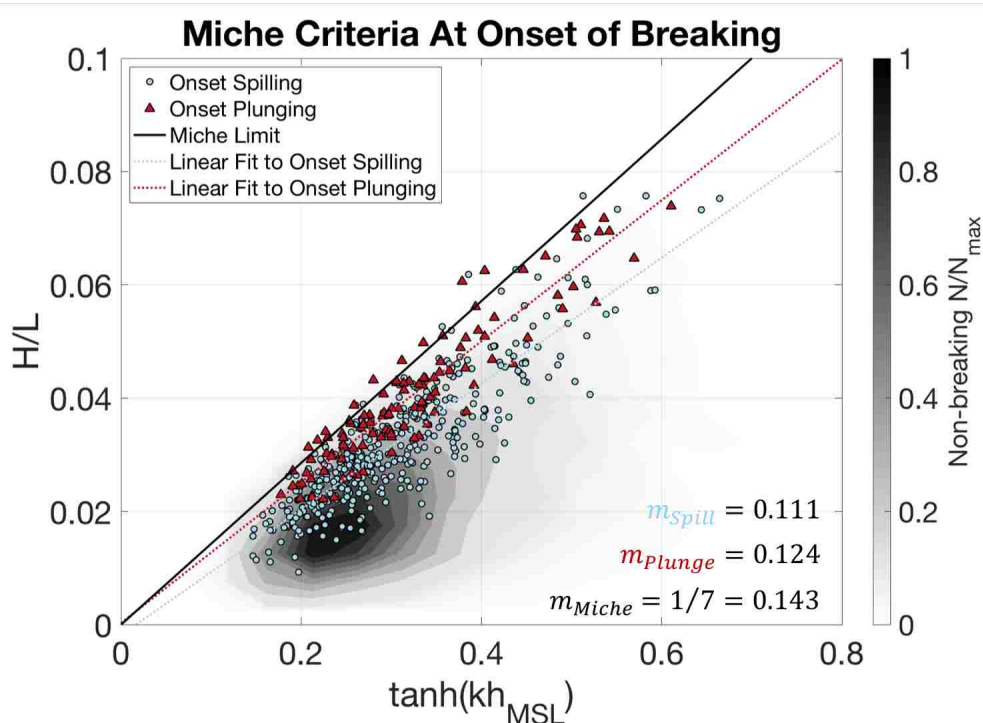
Figure 3.10: Density plot (grayscale) of the Miche steepness H_b/L_b versus $tanh(k_b h_b)$ for non-breaking waves. The values at the onset of breaking for each individual spilling (blue circles) and plunging (red triangles) breaker are overlaid. The Miche limit with slope of 1/7 (black solid line), a linear fit to the onset spilling breaker points (blue dotted line), and a linear fit to the onset plunging breaker points (red dotted line) are shown for comparison.

3.4.2 Implications for Modeling Wave Breaking Using γ

Previous experiments at Duck, NC, have reported a critical breaker parameter of $0.4 < \gamma_s <$ 0.8 (Sallenger and Holman, 1985), where γ_s is calculated using the significant wave height from time series data and does not distinguish between breaking and non-breaking waves. The distributions of spatially-tracked γ (Figure 3.4) compare reasonably to this range for every subset of the data. The mean γ values increase as expected from 0.40 for non-breaking waves, to 0.60 for undetermined type breakers, to 0.65 for spilling breakers, and finally to 0.75 for plunging breakers. On average, we find that γ for plunging breakers is 15% larger than for spilling breakers.

A wide range of γ_s has been reported from field experiments at other beaches, $0.2 <$ $\gamma_s < 1.2$ (Apotsos et al., 2008), and a consistent correlation has been found between local beach slope, β, and γ_s, where γ_s increases with increasing beach steepness (Sallenger and Holman, 1985; Raubenheimer et al., 1996). We find $0.65 < \gamma_s < 0.70$ for the offshore transect where $0 < \beta < 0.02$ and $0.70 < \gamma_s < 0.75$ for the onshore transect where $0.02 < \beta < 0.04$. These γ_s values are greater than what is predicted based on the γ_s-β dependency shown in Figure 7 of Raubenheimer et al. (1996) or Sallenger and Holman (1985). However, we do see different patterns of γ evolution for the offshore and onshore transects that are most likely attributable to differences in local beach slope.

For the onshore transect (Figure 3.6a), the bathymetry monotonically decreases and the transect is close to the shoreline ($x \approx 100$ m). After the breakpoint, H and h decrease in such a way as to maintain relatively constant γ values for both spilling and plunging breakers. For the offshore transect (Figure 3.6b), the bathymetry plateaus, therefore h changes very little. Following the onset of breaking, H decreases but h remains constant, so γ decreases as the spilling and plunging breakers develop. The increase and decrease of γ about the breakpoint was also observed in a study of 10 surf zone breakers by Suhayda and Pettigrew (1977), but has not been confirmed more robustly in the field until now. Interestingly, the breakpoint observed by Suhayda and Pettigrew (1977) occurred just before a plateau of the

bathymetry and the measurements spanned a similar spatial scale (30-40 m).

The variation of γ with breaker type is reasonable and expected based on evidence in the literature. Sallenger and Holman (1985) and Raubenheimer et al. (1996) found γ to vary with local beach slope, but to be independent of offshore wave steepness. Here, Figure 3.6 shows that local beach slope influences the evolution of γ about the onset of breaking, and Figure 3.9 shows that γ is correlated with local wave slope. Since local beach slope and wave steepness (or wave slope) are predictors of breaker type (Galvin, 1968), it follows that γ would vary with breaker type. Therefore, our results suggest that for a beach exhibiting mixed breaker types, parameterizing wave energy dissipation due to breaking using a single γ value does not accurately represent the breaking dynamics (Figure 3.6). For instance, based on the critical γ for SWAN of 0.78 (derived from solitary wave theory), if all waves become spilling breakers, the predicted breakpoint would be onshore of the measured breakpoint, for which $\gamma = 0.63 - 0.71$. However, the predicted breakpoint would be fairly accurate if all waves become plunging breakers, whose measured breakpoint occurs for $\gamma = 0.73 - 0.81$. For mixed breaker type wave conditions, using a single critical γ would yield wave breaking patterns that are either too concentrated or too evenly distributed across the surf zone, which has consequences for wave-driven circulation and sediment transport predictions.

3.4.3 Implications for Modeling Wave Breaking Using Wave Face Slope

Wave face slope follows a similar pattern of evolution about the breakpoint. These trends are indicative of wave shape changes that spilling and plunging breakers undergo as they develop into steady state bores. The shape of a spilling breaker, even at the onset of breaking, is similar to that of the steady state bore into which it is developing, which may account for the relatively constant wave slope following onset. In contrast, plunging breakers undergo a dramatic shape change as they transition to steady state bores, which is consistent with the highly variable wave slope following onset. SWASH, a phase-resolved nearshore wave model, determines the onset of breaking by using a critical local surface steepness threshold of 0.6, which is roughly equivalent to a wave slope of 30°. To our knowledge, this limit has not been

field-tested. This steepness criteria for breaking matches the critical wave slope we estimate for plunging breakers ($\theta_q = 30°$), though spilling breakers exhibit lower wave slope at the breakpoint ($22° < \theta_q < 25.5°$).

3.4.4   Implications for Modeling Wave Breaking Using Wave Speed

Measured wave speed, $\tilde{c}$, also peaks near the onset of breaking. While we are not able to evaluate breaking criteria based on the ratio of wave phase speed to fluid velocities at the crest used in phase-resolved wave models (we do not resolve fluid velocities) (Smit et al., 2014), we can compare measured $\tilde{c}$ to various theoretical wave speeds used in phase-averaged wave models. Two commonly employed theories for wave phase speed in the surf zone are shallow water linear wave theory, $c_{lin} = \sqrt{gh}$, and solitary wave theory $c_{sol} = \sqrt{g(H + h)}$. Figures 3.11a and 3.11b show that $\tilde{c}$ is under-predicted by c_{lin}, and Figures 3.11c and 3.11d show that $\tilde{c}$ is over-predicted by c_{sol}. On average, $\tilde{c}/c_{lin} = 1.23$ for spilling and plunging breakers combined, which is further from a ratio of one than the mean $\tilde{c}/c_{sol} = 0.95$. This agrees with laboratory and field studies of the surf zone, which found that solitary and shock wave speed predictions generally agree with measured wave speeds and out-perform shallow water linear wave theory and bore theory (Postacchini and Brocchini, 2014; Tissier et al., 2011).

3.5   Conclusions

Using cross-shore LIDAR line-scans and IR imagery, we track and classify over 4200 waves to evaluate the conditions for the onset of wave breaking in the surf zone. This remote sensing data fusion enables the segregation of waves into non-breaking, spilling, plunging, and undetermined type breaker classes. The spatial and temporal resolution of the LIDAR allows for direct computation of γ, wave face slope, and wave phase speed at every instant each wave is tracked across the surf zone.

We find that mean γ calculated from all the observed waves agrees with previous *in situ* time-series estimations of γ at Duck, NC. When further segregated by breaker type
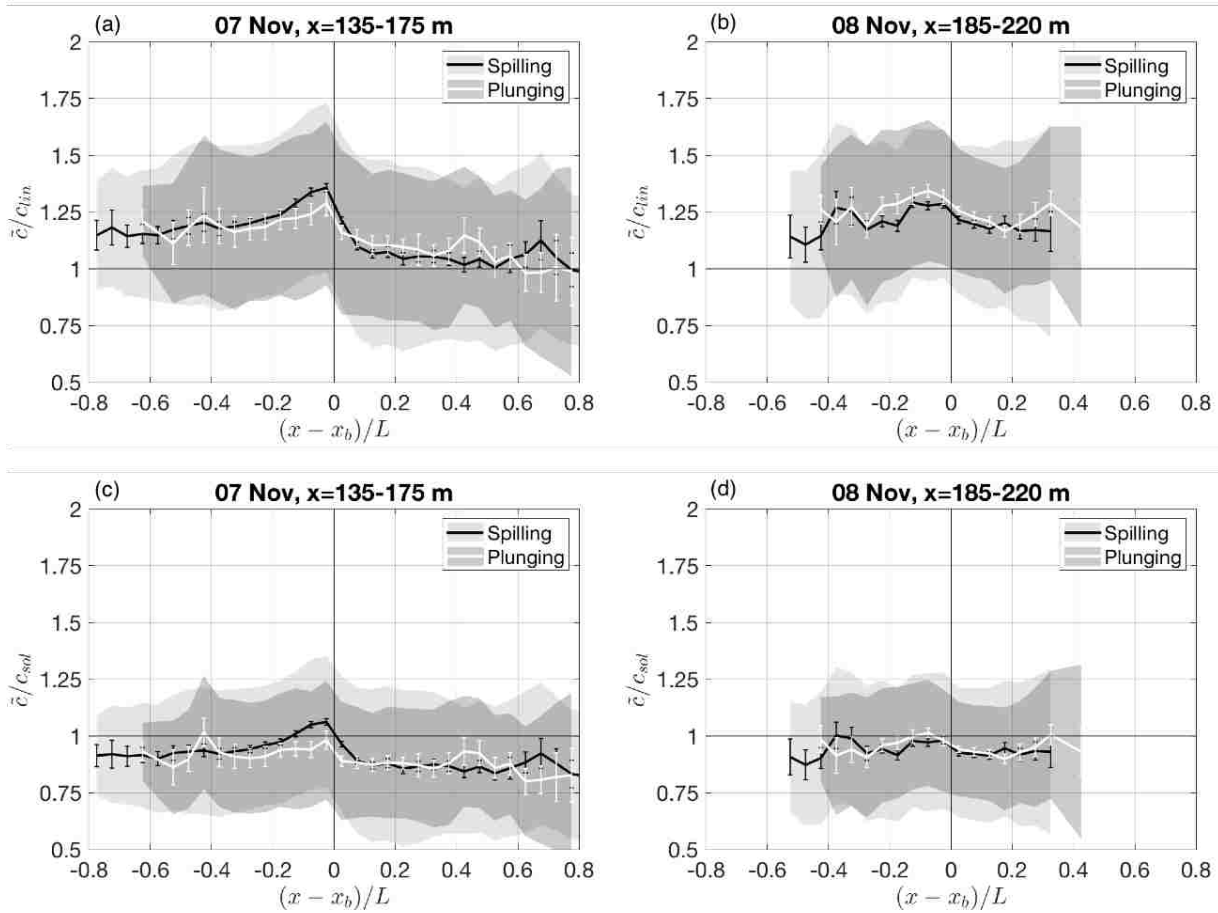
Figure 3.11: Evolution of the ratio of wave speeds, (a,b) $\tilde{c}/c_{lin}$ and (c,d) $\tilde{c}/c_{sol}$, for spilling (black line) and plunging (white line) breakers observed on (a,c) 07 November and (b,d) 08 November.

and examined as a function of cross-shore position, plunging breakers exhibit larger γ than spilling breakers. This suggests that the variability in γ reported from other field observations (0.4< γ <1.2) may be due in part to variability in the dominant breaker type at each study site.

Using a normalized cross-shore coordinate, the evolution of γ, θ_q, and $\tilde{c}$ was examined about the breakpoint for spilling and plunging breakers. Both γ and θ_q increase to a maximum near the onset of breaking, with plunging breakers achieving 15% higher γ and 18-36% steeper wave slopes than spilling breakers. There is no statistically significant difference between wave speed $\tilde{c}$ for spilling and plunging breakers, and both breaker types exhibit an increased wave speed at the onset of breaking. On average, $\tilde{c}$ is better described by solitary wave theory than shallow water linear wave theory. On average, c_{sol} is biased low, with $\tilde{c}/c_{sol}$=0.95, and c_{lin} is biased high, with $\tilde{c}/c_{lin}$=1.23.

We robustly characterize the γ and wave slope θ_q parameter space for the surf zone. The likelihood of observing non-breaking versus breaking waves or spilling versus plunging breakers based on γ and θ_q is useful for determining appropriate breaking limits for nearshore wave models and also helps describe the continuum of breaker type. The transition from non-breaking to breaking estimated using γ and wave face slope ($\gamma = -0.049\theta_q + 1.41$) could be incorporated into nearshore models to improve the parameterization of wave breaking. While a similar equation for the transition from spilling to plunging is not statistically supported by this dataset, there is a discernible relationship between γ and θ_q with respect to breaker type that may be defined with the inclusion of more data. If wave face slope is not resolved by the model, we suggest utilizing the relationship between wave slope (fit to the upper 80% of the wave face) and the ratio of the sea surface elevation to the modified wavelength, the wavelength shoreward of the wave crest, presented in Figure 2.12. We note that further investigation or assumptions would be required to relate the modified wavelength to the full wavelength, which is typically computed in nearshore wave models.

As a final extension, we test a shallow water Miche steepness criteria for the onset of breaking and find that it underestimates the breaking rates for most plunging and spilling

breakers. However, 99.0% of non-breaking waves fall below the Miche limit, and 90.5% of non-breaking waves fall below the most conservative Miche-type breaking limit derived from the spilling breaker data. Bulk statistics or critical values near the onset of breaking are still helpful especially if the modeled beach is known to be dominated by one type of breaker. If processes forced on shorter time and spatial scales are of interest, then an accurate, local critical γ or critical wave steepness (from wave face slope or the Miche criteria) is important. Ultimately, these geometric and kinematic differences at the onset of spilling and plunging breakers imply a difference in the wave energy dissipation rates. This topic will be explored in future research.

Chapter 4

ENERGETICS

4.1 Introduction

Spilling and plunging breakers transform and dissipate energy differently across the surf zone (Ting and Kirby, 1995, 1996), which affects the spatial and temporal distribution of wave forcing responsible for generating alongshore and cross-shore currents, suspending sediment, and enhancing air-sea gas exchange. However, most nearshore wave models parameterize wave energy dissipation based on the steady state hydraulic jump or bore-type breaker (e.g., Thornton and Guza, 1983; Battjes and Janssen, 1978). Therefore, they do not account for differences in energy dissipation rate due to breaker type (i.e., spilling versus plunging) or due to different breaker dynamics during the initial stages of breaking, prior to the wave achieving steady state. This chapter uses a subset of the LIDAR-IR-tracked breaking waves to attempt to quantify the differences in wave energy dissipation rate between spilling and plunging breakers during the initial stages of breaking.

4.1.1 Wave Energy Balance

Assuming straight and parallel bathymetry and shore-normal wave propagation, the cross-shore gradient of wave energy flux, $\mathcal{F}$, is balanced by dissipation due to breaking ϵ_{break}, dissipation due to bottom friction ϵ_{bot}, and reflection R following

$$(1 - R)\frac{\partial \mathcal{F}}{\partial x} = \epsilon_{break} + \epsilon_{bot}. \tag{4.1}$$

The dissipation due to bottom friction is much smaller than that due to breaking (Thornton and Guza, 1983) and is neglected. Reflection depends on beach steepness, tidal elevation, and wavelength, and has been reported to range from 3% to 18% of the incoming wave energy

at our study site (Elgar et al., 1994). Wave energy flux is defined as,

$$\mathcal{F} = Ec_g, \tag{4.2}$$

where wave energy, E, is estimated according to linear theory as a function of water density ρ, gravitational acceleration g, and the root-mean-squared wave height across the surf zone H_{rms},

$$E = \frac{1}{8}\rho g H_{rms}^2, \tag{4.3}$$

and group speed c_g may be approximated by phase speed c under shallow water linear wave theory assumptions. Energy may also be written in terms of the significant wave height, $H_s = \sqrt{2}H_{rms}$, as

$$E = \frac{1}{16}\rho g H_s^2. \tag{4.4}$$

In situ estimation of wave energy dissipation typically requires an array of instruments that measure wave height across the surf zone, along with an estimate of wave phase speed, which is most commonly made using water depth based on shallow water linear wave theory, $c_{lin} = \sqrt{gh}$ (Thornton and Guza, 1986; Elgar et al., 1994; Madsen et al., 1997; Ruessink et al., 2001; Feddersen, 2012). The wave energy dissipation rate is discretely computed as the wave energy flux gradient between instrument positions,

$$\frac{\triangle\mathcal{F}}{\triangle x} = \frac{\mathcal{F}(x_i) - \mathcal{F}(x_{i-1})}{x_i - x_{i-1}}. \tag{4.5}$$

Nearshore wave models can be verified by assessing the wave energy balance across the surf zone, using data collected in intermediate or deep water to estimate the incoming energy flux and data collected within the inner surf zone to estimate the energy flux after breaking. However, this comparison does not resolve spatial or temporal patterns of wave energy dissipation that occur on a scale less than the instrument spacing, which is typically greater than 10 m. Remote sensing technologies provide broad spatial coverage and high spatial and temporal resolution, which enable the investigation of such patterns by decreasing the distance between sampling locations $x_i - x_{i-1}$.

Evaluation of the right hand side of equation 4.1, depend on the chosen formulation of ϵ_{break}. We will test two common parameterizations of energy dissipation due to breaking, the bore model and the roller model.

Hydraulic Bore Model

The most common model for ϵ_{break} in equation 4.1 is a hydraulic jump or bore. In a hydraulic bore, (schematic shown in Figure 4.1) energy is lost in the turbulent motions of a hydraulic jump, which implies the direct transformation of wave motion into turbulent motion. The decrease of wave energy throughout the propagation of a turbulent bore occurs simultaneously with the decrease in total momentum flux. In other words, for a breaking wave that has reached a steady state bore phase, wave forcing is occurring instantaneously, at the same time and place as the breaking.
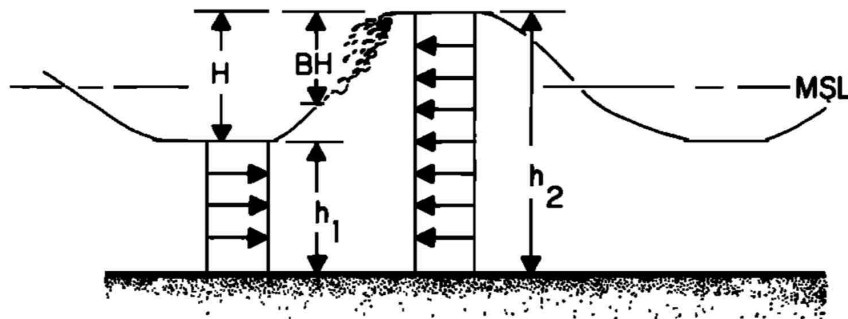
Figure 4.1: Diagram of a steady state breaking wave bore indicating the instantaneous wave height (H) and bore height fraction (B) used to parameterize the bore energy dissipation (from Thornton and Guza (1983)).

Following Le Mehaute (1962), the energy dissipation rate of a breaking wave is estimated from a bore or hydraulic jump of equivalent height (Stoker, 2011),

$$\epsilon_{bore} = \frac{1}{4}\rho g \frac{(h_2 - h_1)^3}{h_1 h_2} Q.$$

(4.6)

In equation 4.6, h_1 and h_2 are the water depth ahead of and behind the bore, respectively (as in Figure 4.1), and Q is the volume discharge per unit area across the bore. The volume discharge may be estimated under steady conditions as $Q = ch/L$, where c is the wave speed, h is the mean water depth, and L is the wavelength. In the numerator of equation 4.6, the distance $h_2 - h_1$ represents the peak-to-trough wave height H. For the hydraulic bore model, wave height is modulated by a coefficient B, a calibration factor of order 1, conceptualized as the fraction of the wave face covered by the turbulent bore, as shown in Figure 4.1 (Le Mehaute, 1962). Using these substitutions and the assumption that $h_1 h_2 \approx h^2$, we estimate the average energy dissipation per unit area in a breaking wave as,

$$\epsilon_{bore} = \frac{1}{4} B \rho g \frac{1}{T} \frac{H^3}{h}. \tag{4.7}$$

As stated, equation 4.7 is deterministic and represents the average energy dissipation per unit area in a single breaking wave. However, nearshore wave models propagate a spectrum of waves onshore and the energy dissipated when some proportion of that spectrum breaks, for a given water depth, must be estimated statistically. To that end, wave height and wave period statistics, as well as a predictor of the fraction of waves that break, Q_b, are used in the wave-averaged dissipation rate:

$$\epsilon_{bore} = \frac{1}{4} B \rho g \frac{1}{\overline{T}} Q_b \frac{H_{rms}^3}{h}. \tag{4.8}$$

There are several parameterizations for Q_b at a given location (or water depth) (including Baldock et al., 1998; Ruessink et al., 2003; Janssen and Battjes, 2007), all of which are a function of the breaker parameter $\gamma = H_b/h$, where H_b is the wave height at the onset of breaking. The differences lie in the critical value of γ and the distribution of wave heights and breaking wave heights based on H_{rms} and H_b (such as the Rayleigh distribution proposed by Thornton and Guza (1983)). A thorough testing of several parameterizations by Apotsos et al. (2008) found that no one parameterization out-performs the others and γ must be tuned to each field site.

4.1.2 Wave Roller Model

Numerical models (Iafrati, 2011) and field measurements (Feddersen, 2012) have found that the majority of the energy dissipation from a spilling breaker is concentrated above trough level, very near the water surface, as a result of the shear between the down-flowing roller and the up-wave face orbital flow of the fluid beneath it. The wave roller model, developed in the laboratory by Duncan (1981), balances the shear stress, τ, along the breaking boundary, L_r, with the tangential component of the weight of the aerated breaking region of cross-sectional area A on the underlying wave face,

$$\tau L_r = \rho' g A \sin \theta. \tag{4.9}$$

Here, θ is the slope of the breaking wave face and ρ' is the density of the aerated roller. In Duncan (1981), the roller density is $\rho'/\rho = 0.61$, but this ratio ranges from 0.4 to 0.87 in the literature.

A diagram of the roller is shown in Figure 4.2. Duncan (1981) found the geometry of the breaking region to be self-similar by showing that the aspect ratio, the ratio of its thickness to its length, was constant for all observed breakers,

$$\frac{\text{thickness}}{\text{length}} = \frac{A/L_r}{L_r} = \frac{A}{L_r^2} = 0.11 \pm 0.01. \tag{4.10}$$

This observation allows A to be eliminated from (4.9). The Duncan (1981) wave roller parameterization provides a framework for estimating energy dissipation due to spilling breakers on a wave-by-wave basis using roller length, wave slope and density of the breaking region. However, the relationship between A and L_r and the ratio of ρ' to ρ in the field remain unknown, mainly because they are extremely difficult to measure. Therefore, we form a general roller model that makes no assumptions about these relationships. The average energy dissipation per unit area given by the roller model is,

$$\epsilon_{roller} = C_r \rho g L_r^2 \frac{\sin \theta}{\bar{T}}, \tag{4.11}$$

where $C_r = (\rho'/\rho)(A/L_r^2)$ and $\bar{T}$ is the average wave period.
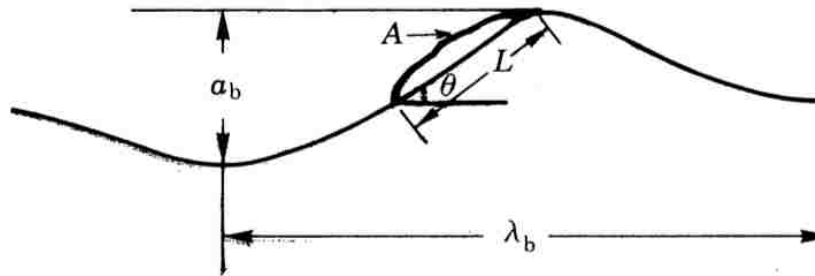
Figure 4.2: A schematic of the idealized wave roller (from Duncan (1981)). The roller cross-sectional area A, roller length L_r, and wave slope θ are indicated.

The wave roller model has been tested in the laboratory and the field for steady state spilling breakers. Haller and Catalan (2009) used the D81 wave energy dissipation formula to predict wave height from camera-based roller length estimates and compared the results to measured wave height across a freshwater laboratory surf zone. Results were promising over the limited range of waves produced, and although no direct estimate of wave energy dissipation was made, the authors suggested that the D81 parameterization could be used to estimate wave dissipation in the field. Since then, the wave roller model has been successfully tested in the field to estimate total wave energy dissipation along a cross-shore transect (Carini et al., 2015), map average dissipation rates over a 2D area (Díaz et al., 2017), and estimate wave-by-wave energy dissipation for steady state spilling breakers (Martins et al., 2018).

4.2   Methods

4.2.1   Data Description & Noise Reduction

A subset of 72 spilling and 35 plunging breakers, each observed for at least $0.3T$ s following the onset of breaking, are selected for analysis and comparison of wave energy flux and dissipation rates. The distribution of tracked wave heights and wave periods for these 107 breakers are comparable, as shown in Figure 4.3.
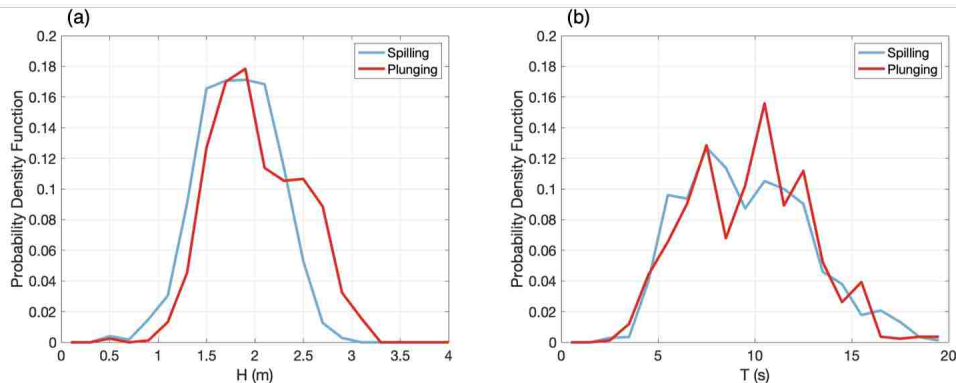
Figure 4.3: Histograms of (a,b) tracked wave height and (c,d) tracked wave period for (a,c) 72 spilling and (b,d) 35 plunging breakers.

Because estimating the wave energy flux gradient requires differencing, an operation that amplifies noise in a dataset, a smoothing protocol is implemented on all tracked wave parameters. For wave height, wave period, wave face slope, and wave speed, a 10-point smoothing (loess) is performed for each tracked wave. The loess filter performs a local quadratic (nonlinear) least-squares regression on the data (Schlax and Chelton, 1992), which retains the pattern of evolution of the tracked parameter while reducing its variance. On averaged, the 10-point window spans 5 m. An example of the loess filtered wave height is shown in Figure 4.4.

4.2.2 Estimating Wave Energy Dissipation Rate

Dissipation rates are estimated using the linear formulation of the wave energy flux gradient based on wave height and wave form speed (as discussed in Section 2.4.2), the bore model, and the roller model. For the linear formulation, the wave energy E is estimated from equation 4.4 because our measured wave heights near the onset of breaking are more statistically similar to H_s than to H_{rms}. All estimates are made using smoothed parameter values and calculated at or between (for gradients) every location that the wave peak is tracked. Equation 4.4 is evaluated using individual trough-to-peak wave height, H. The wave energy flux $\mathcal{F}$ is
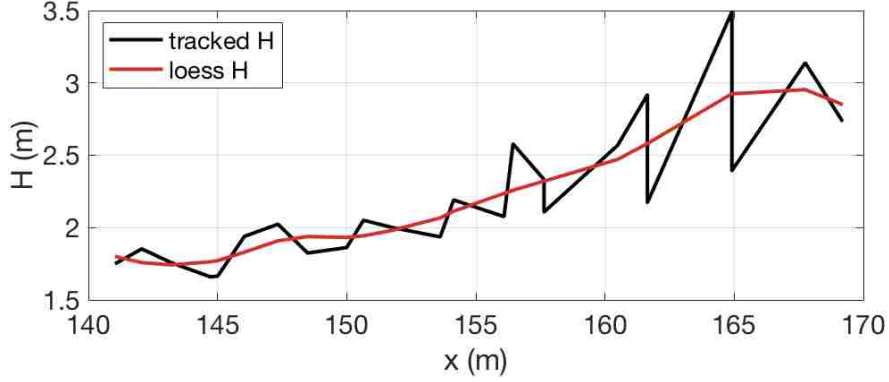
Figure 4.4: Example result from loess filtering the tracked wave height for a plunging breaker.

estimated from equation 4.2 using E and c, and the wave energy flux gradient is estimated from equation 4.5 using $\mathcal{F}$ and the skewed-Gaussian peak locations $\tilde{x}_{pk}$. For the bore model, equation 4.7 is evaluated using H, T, h, and $B = 1$. For the roller model, equation 4.11 is evaluated using L_r, θ_q, and T, with values for A/L_r^2 and ρ'/ρ from Duncan (1981).

To compare between spilling and plunging breaker types, we ensemble-average the wave energy flux and dissipation rate estimates. The spatial extent of each tracked wave is centered on the location of the peak at the onset of breaking and normalized by the individual wavelength: $x' = (x - x_b)/L$. The wave energy flux and dissipation rates are normalized by their value at the onset of breaking for each wave, for example, $\mathcal{F}' = \mathcal{F}(x')/\mathcal{F}(0)$. After normalization, energetic quantities for each breaker type are bin-averaged using bins $x' = -0.5 : 0.02 : 0.5$ (negative x' indicates after the onset of breaking).

4.3   Results

4.3.1   Wave Energy Flux

The general pattern of evolution of wave energy flux is consistent, regardless of breaker type. Figure 4.5 shows the normalized wave energy flux, $\mathcal{F}'$, for individual spilling and plunging breakers, as well as the ensemble average for each breaker type. Individual $\mathcal{F}'$ profiles for

plunging breakers exhibit more variability than spilling breakers. However, the ensemble-averaged profiles show that $\mathcal{F}'$ decreases steadily after the onset breaking ($x' < 0$) for both spilling and plunging breakers. Prior to breaking ($x' > 0$), $\mathcal{F}'$ increases, which seemingly disobeys conservation laws. This will be discussed in Section 4.4.
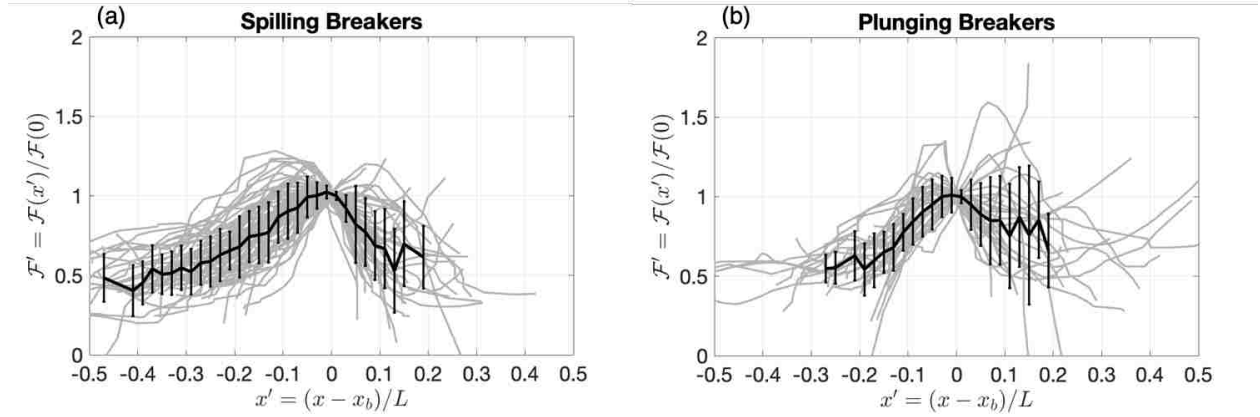
Figure 4.5: Individual (grey) and bin-averaged (black) normalized wave energy flux for (a) 72 spilling breakers and (b) 35 plunging breakers as a function of normalized distance from the onset of breaking (negative x' indicates after onset of breaking). Error bars extend one standard deviation from the mean.

Comparing the evolution of $\mathcal{F}'$ for spilling and plunging breakers in Figure 4.6a confirms that plunging breakers lose energy at a greater rate than spilling breakers just after the onset of breaking. A two-sided t-test confirms that the difference between ensemble-averaged spilling and plunging $\mathcal{F}'$ profiles is statistically significant for $-0.1 \geq x' > -0.2$. The general trends and range of statistically significant difference for spilling and plunging $\mathcal{F}'$ are consistent even when the mean wave form speed is used in equation 4.2 instead of the tracked wave form speed, as shown in Figure 4.6b. However, the rate of change of wave energy flux, or the dissipation rate, is effected by the choice of wave speed metric.

To estimate this dissipation rate, we fit a line to $\mathcal{F}'$ over sequential intervals of x'. The slopes of these lines correspond to the fraction of normalized wave energy flux lost per wavelength L. Tables 4.1 and 4.2 report the fitted slopes and their 95% confidence intervals
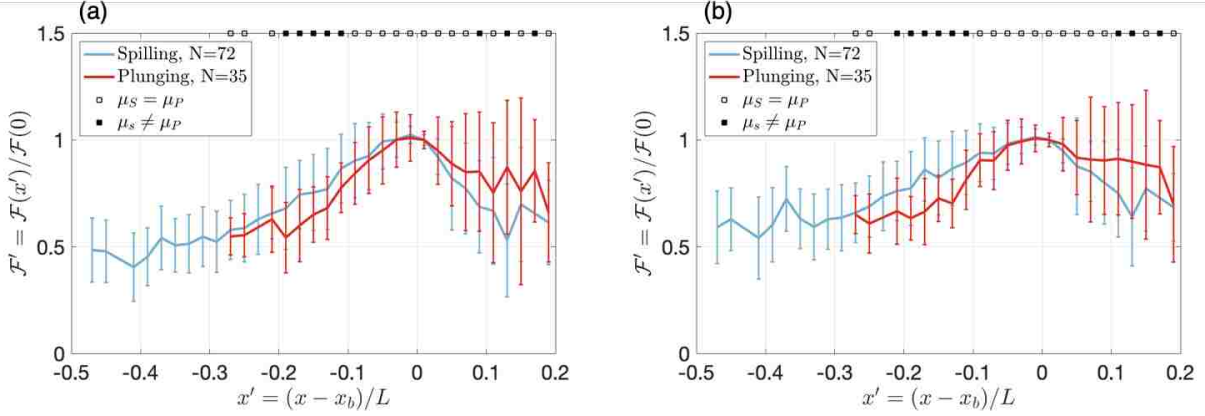
Figure 4.6: Bin-averaged normalized wave energy flux, estimated using (a) tracked wave speed $\tilde{c}$ and (b) mean wave speed $\langle\tilde{c}\rangle$, for spilling (blue) and plunging (red) breakers as a function of normalized distance from the onset of breaking (negative x' indicates after onset of breaking). Error bars extend one standard deviation from the mean. The squares along the top axis report when the mean wave energy flux from spilling and plunging breakers is significantly different (filled square) and not significantly different (open square), according to a two-sided t-test.

for wave energy flux calculated using tracked wave form speeds and mean wave form speeds, respectively.

Table 4.1 shows that the dissipation rate is greatest for $-0.03 \geq x' > -0.2$. Over this interval, wave energy flux decreases by about 21% every $0.1L$ for spilling breakers and by about 30% every $0.1L$ for plunging breakers. For $-0.2 \geq x' > -0.3$, the rate of change of wave energy flux is approximately equal for spilling and plunging breakers, with wave energy flux decreasing about 14% per $0.1L$.

Overall, the dissipation rates are lower when estimated using mean wave form speed. For $-0.03 \geq x' > -0.2$, Table 4.2 shows that the rate of change of $\mathcal{F}'(\langle\tilde{c}\rangle)$ for spilling breakers is 13% per $0.1L$, which is 38% smaller than when the tracked wave form speed is used. Plunging breakers lose 24% per $0.1L$ over this interval, which is 20% smaller than the dissipation rate estimated using the tracked wave form speed.

Next, instead of estimating wave energy flux gradients from the ensemble-averaged profile,

x'	Spilling	Plunging
$0.01 \geq x' > -0.03$	-0.05 (-8.4, 8.3)	-0.02 (-3.3, 3.2)
$-0.03 \geq x' > -0.2$	2.1 (1.8, 2.4)	3.0 (2.7, 3.2)
$-0.2 \geq x' > -0.3$	1.4 (0.4, 2.3)	1.4 (0.2, 2.6)

Table 4.1: Rate of change of normalized wave energy flux $(\partial \mathcal{F}'(\tilde{c})/\partial x')$ for various ranges of x' estimated using tracked wave speed, $\tilde{c}$, for spilling and plunging breakers. Mean values reported with 95% confidence interval in parentheses.

x'	Spilling	Plunging
$0.01 \geq x' > -0.03$	0.05 (-5.1, 5.3)	-0.2 (-3.7, 4.1)
$-0.03 \geq x' > -0.2$	1.3 (1.0, 1.6)	2.4 (2.0, 2.9)
$-0.2 \geq x' > -0.3$	1.8 (1.1, 2.4)	0.5 (-2.2, 3.2)

Table 4.2: Rate of change of normalized wave energy flux $(\partial \mathcal{F}'(\langle \tilde{c} \rangle)/\partial x')$ for various ranges of x' estimated using mean wave speed, $\langle \tilde{c} \rangle$, for spilling and plunging breakers. Mean values reported with 95% confidence interval in parentheses.

we do so for each individual breaker. Figure 4.7 plots the normalized dissipation rate from $0 > x' > -0.2$ for each spilling and plunging breaker as a function of the predictors γ and θ. Our observations from Section 3.4.1 are confirmed by these 108 individual breakers; as γ and θ increase, the breaker type transitions from spilling (marked by circles) to plunging (marked by triangles), with some overlap along the continuum. Most of the plunging breakers exhibit higher initial normalized dissipation rates than the spilling breakers. However, there is no strong correlation between increased γ and θ and increased dissipation rate.
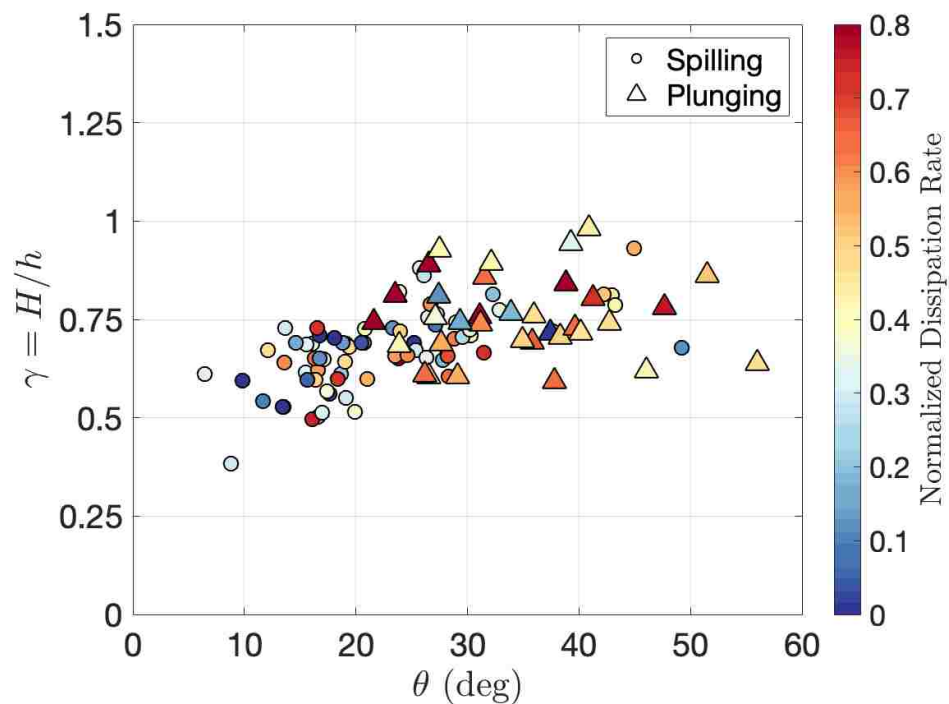
Figure 4.7: Normalized dissipation rate (colorbar), or wave energy flux gradient, estimated over the first $0.2L$ from the onset of breaking for individual spilling (circles) and plunging (triangles) breakers, plotted as a function of θ and γ.

4.3.2 Dissipation Rate Models

Dissipation rate estimated using the bore model (equation 4.7) and the roller model (equation 4.11) are presented in the same manner as wave energy flux, normalized by their values at onset and bin-averaged for each breaker type. Figure 4.8 shows results from the bore model. Relative to the dissipation rate at onset, spilling breakers maintain an elevated dissipation rate for a greater fraction of a wavelength than plunging breakers. However, the non-normalized mean dissipation rate at onset is 1159.8 W m^{-2} for plunging breakers and 865.6 W m^{-2} for spilling breakers. So on average, the bore model estimates that plunging breakers have 38% larger dissipate rates than spilling breakers near the onset. The evolution of normalized, ensemble-averaged ϵ_{bore} for $0 \geq x' > -0.3$ shows that the bore model predicts spilling breakers dissipate energy more gradually than plunging breakers near the onset of breaking. The statistical significance of these difference are again recorded along the top axis of Figure 4.8 from a two-sided t-test.
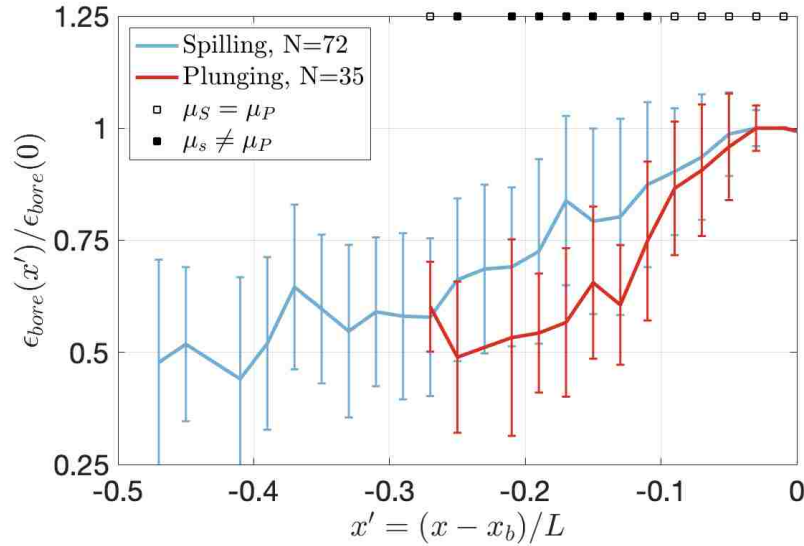
Figure 4.8: Bin-averaged normalized dissipation rate estimated using the bore model for spilling (blue) and plunging (red) breakers as a function of x'. Error bars and t-test results are presented in the same format as Figure 4.6.

Figure 4.9 shows results from the roller model when evaluated using $A/L_r^2 = 0.11$ and $\rho'/\rho = 0.61$ from Duncan (1981). There is only one small region of statistically significant difference, $-0.25 \leq x' \leq -0.27$, between the normalized, ensemble-averaged ϵ_{roller} for spilling and plunging breakers. The lack of statistical difference is attributed to the large variability between individual ϵ_{roller} profiles as indicated by the large error bars on the ensemble-averaged curves. Non-normalized mean ϵ_{roller} at the onset of breaking is 882.5 W m^{-2} for spilling breakers and 911.5 W m^{-2} for plunging breakers, which is only a 3.3% difference. For spilling breakers, the roller predicted dissipation rate gradually decreases with relatively small scale variability from $x' = 0$ to $x' = -0.5$. No such pattern emerges for plunging breakers, whose normalized, ensemble-averaged ϵ_{roller} exhibits high variability with multiple, relatively large increases and decreases from $x' = 0$ to $x' = -0.27$.
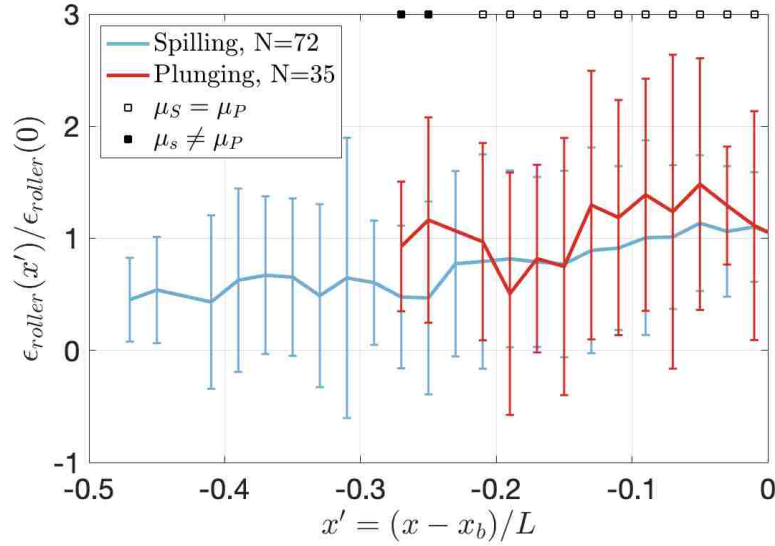
Figure 4.9: Bin-averaged normalized dissipation rate estimated using the roller model for spilling (blue) and plunging (red) breakers as a function of x'. Error bars and t-test results are presented in the same format as Figure 4.6.

4.4   Discussion

4.4.1   Case Study: Model Comparison

To compare the magnitudes in addition to the evolution of dissipation rate near the onset of breaking, we choose one spilling and one plunging wave of approximately equal wave height breaking in similar water depth. The dissipation rate estimates from the bore model and the roller model (evaluated using A/L_r^2 and ρ'/ρ from Duncan (1981)) are compared to the best estimate of true dissipation rate calculated via equation 4.5. Based on the results for wave energy flux (Figure 4.6), equation 4.5 is evaluated using the tracked wave speed $\tilde{c}$ and the mean wave speed $\langle\tilde{c}\rangle$. We cannot make this comparison on an ensemble-averaged basis because the averaging aliases the impact the observed wave height and wave period distributions, making a wave energy balance untenable.

Figure 4.10 shows the dissipation rate comparison and the relevant wave parameters as a function of normalized distance from the onset of breaking for the chosen spilling and plunging breakers. Note that while it appears the plunging breaker was observed over a shorter distance than the spilling breaker, this is an artifact of the x-axis normalization, as the plunging breaker exhibited a longer average wavelength. In fact, the spilling and plunging breakers were observed for similar real-world distances (27 m and 21 m, respectively) following the onset of breaking.

For the spilling breaker, the roller model produces a gradual increase, followed by a gradual decrease in dissipation rate, which mimics $\triangle\mathcal{F}/\triangle x$ (regardless of wave speed metric used). The maximum value of ϵ_{roller} is half that of $\triangle\mathcal{F}(\tilde{c})/\triangle x$, but agrees well with $\triangle\mathcal{F}(\langle\tilde{c}\rangle)/\triangle x$. Unlike $\triangle\mathcal{F}/\triangle x$, ϵ_{roller} does not decrease to zero, but plateaus around 500 W m^{-2} for $x' < -0.3$. The bore model does not capture the gradual ramp up of dissipation rate. Instead, ϵ_{bore} is nearly at its maximum at the onset of breaking. It increases slightly to a peak of 1500 W m^{-2} at $x' = -0.04$ and then gradually decreases, plateauing at a value slightly higher than ϵ_{roller} at about 650 W m^{-2} for $x' < -0.3$.

For the plunging breaker, neither the bore model nor the roller model replicate the
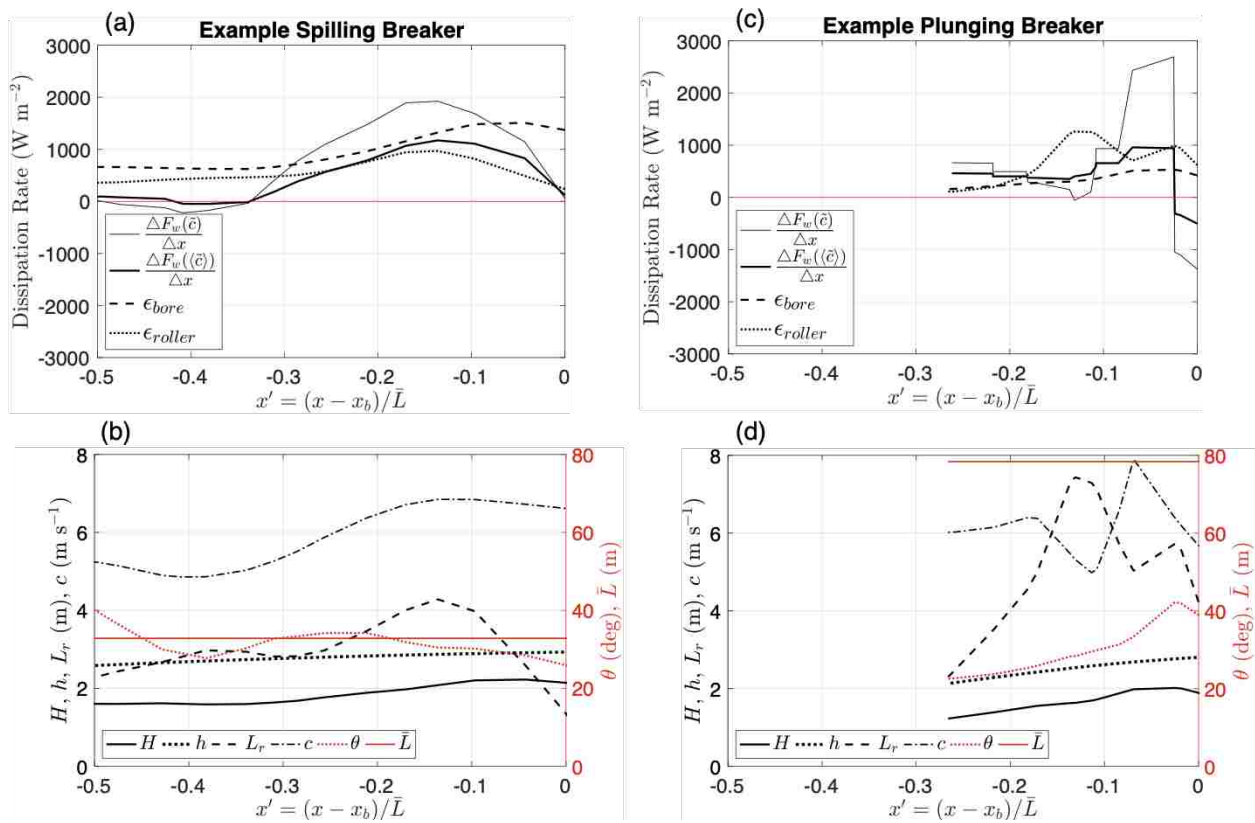
Figure 4.10: Comparison of dissipation rate estimates plotted as a function of x' for (a) a spilling breaker and (c) a plunging breaker. The wave parameters used to estimate $\partial \mathcal{F}/\partial x$, ϵ_{bore}, and ϵ_{roller} are also plotted for (b) the spilling breaker and (d) the plunger breaker. The with line color in (b,d) corresponds to the applicable y-axis.

shape or magnitude of the dissipation rate estimated from $\triangle\mathcal{F}(\tilde{c})/\triangle x$. In the span of $-0.01 > x' > -0.03$, $\triangle\mathcal{F}(\tilde{c})/\triangle x$ jumps to a maximum value of 2700 W m^{-2}. It then decreases to 950 W m^{-2} by $x' = -0.07$, drops to 0 W m^{-2} at $x' = -0.125$, and finally rebounds to an average value of about 450 W m^{-2} for $-0.15 > x' > -0.25$. Based on the evolution of H and $\tilde{c}$ in Figure 4.10d, the variability in $\triangle\mathcal{F}(\tilde{c})/\triangle x$ is dominated by similar variability in measured wave form speed. This is further supported by the much smoother evolution of $\triangle\mathcal{F}(\langle\tilde{c}\rangle)/\triangle x$, estimated using mean wave form speed. The roller model estimates higher dissipation rate than the bore model and exhibits some variability as the breaker develops, though not in the same way as $\triangle\mathcal{F}(\tilde{c})/\triangle x$. The bore model behaves very similarly for the plunging breaker as observed for the spilling breaker, except it has much smaller magnitude, with a maximum of about 530 W m^{-2}.

For $0 > x' > -0.03$ both estimates of $\triangle\mathcal{F}/\triangle x$ are negative, indicating that there was some other source of energy convergence as the wave crest begins to overturn. This increase in wave energy flux (or corresponding negative wave energy flux gradient, relative to the normalized x-coordinate) was also seen in Figure 4.6 for both spilling and plunging breakers. Prior to the onset of breaking, the wave energy flux should be constant. However, because this analysis was performed along a cross-shore transect, it is possible that energy convergence in the alongshore direction, which is not accounted for, is responsible for the increasing wave energy flux. Ultimately, the observations described here, especially for the individual spilling and plunging breakers, are inconclusive as the variability cannot be definitively ascribed to a single cause. To truly compare dissipation rate models and the wave energy flux gradient, the energy contributions from both the x and y directions must be resolved.

4.4.2 Variability & Limitations of the Roller Model

The roller model is likely not appropriate for plunging breakers near the onset of breaking, because they do not produce a roller until steady state is achieved. However, if the large region of active foam produced just after onset (by the impinging jet, collapsing air cavity, splash up, secondary plunging, etc.) is measured as a proxy roller length, ϵ_{roller} could compare

favorably with $\partial\mathcal{F}/\partial x$. This will be further examined for the example plunging breaker in the next section. For now, we investigate multipath IR reflections as a possible explanation for roller length variability, especially for steep plunging breakers, that would contaminate the normalized and ensemble-averaged ϵ_{roller}.

Our hypothesis is that increased pixel intensities in the IR imagery due to multipath reflection along steep plunging wave faces (Branch et al., 2014) are falsely identified as active breaking by the automatic breaker detection algorithm. If active breaking is automatically detected prior to the onset of breaking due to steep wave face slope or if the region of active foam is overestimated due to multipath reflections at the toe of the roller, L_r will be biased high and ϵ_{roller} is subject to errors of $\mathcal{O}(L_r^2)$. We can use ensemble-averaged wave profiles of the automated detection of active foam to further investigate.

The following analysis was completed on the same 72 spilling and 35 plunging breakers included in the normalized and ensemble-averaged ϵ_{roller} profiles. The vertical coordinates of individual wave profiles are centered on z_{tr} and normalized by H, $z' = (z - z_{tr})/H$. The horizontal coordinates of individual wave profiles are centered on x_{pk} and normalized by $L = \tilde{c}T$, $x' = (x - x_{pk})/L$. Using the normalized profiles, we compute the ensemble-averaged profiles for spilling and plunging breakers at pre-onset ($-0.05 < t' < 0$), onset ($0 < t' < 0.05$), post-onset ($0.1 < t' < 0.2$), and developing ($0.2 < t' < 0.3$) breaking stages, where $t' = (t - t_b)/T$. The ensemble-averaged profiles with 95% confidence interval are shown in Figure 4.11. Overlain on the profiles at each stage of breaking is the corresponding probability of the presence of active foam (foam produced by breaking). The probability of the presence of active foam along the wave face is calculated by averaging the masks of breaking from individual wave profiles, as presented in Figure 2.7c.

As expected, the probability of the presence of active foam is near zero along the front face of the pre-onset profiles (Figures 4.11a and 4.11e). The very low, non-zero active foam probabilities observed near the peak of pre-onset spilling and plunging ensemble-averaged profiles are caused by variations in the data, such as sea spray at the crest or IR multipath reflections off the pre-onset wave faces (Branch et al., 2014). Since the active foam probability
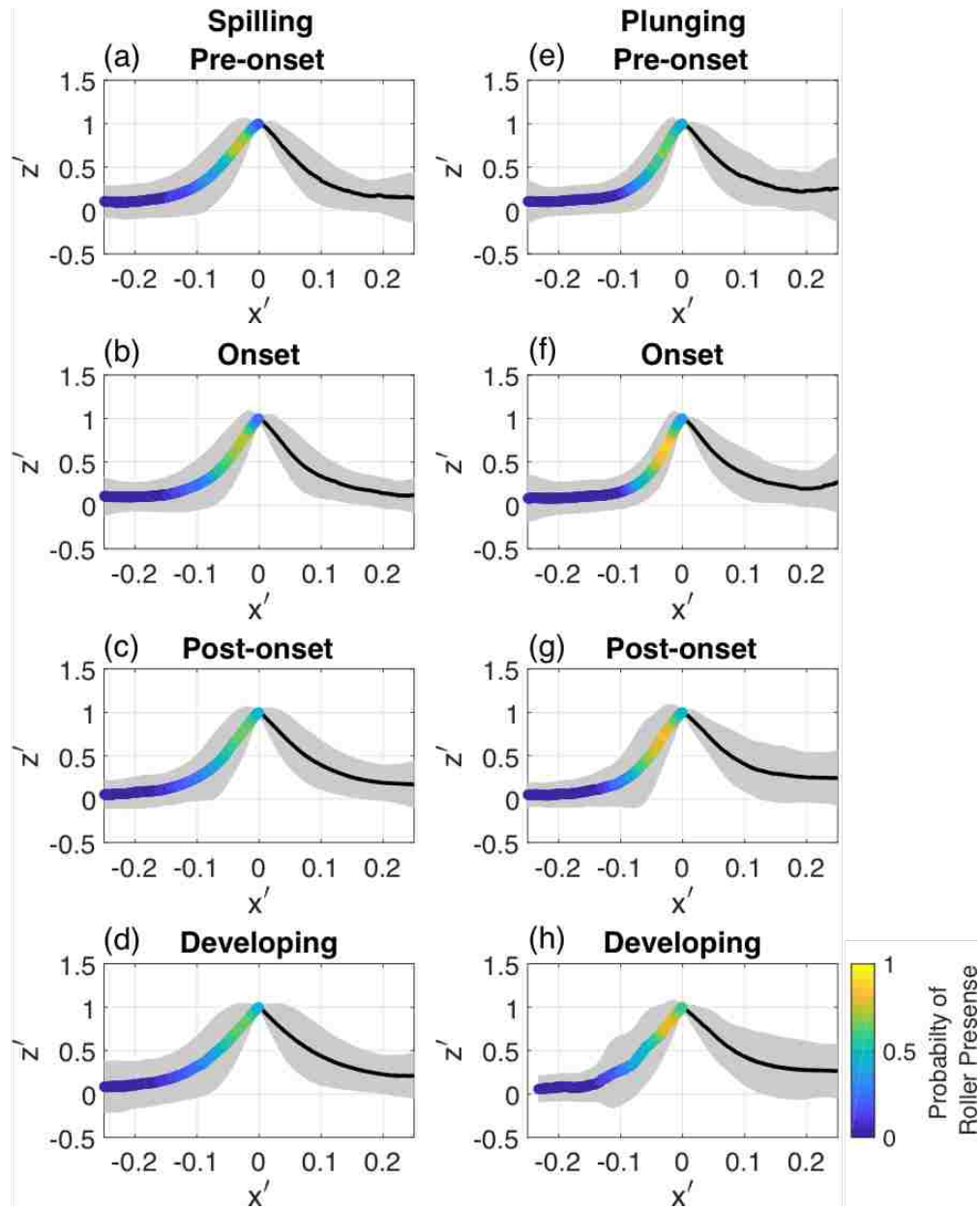
Figure 4.11: Ensemble-averaged wave profiles (black curves) with 95% confidence intervals (gray bands) for (a) pre-onset spilling, (b) onset spilling, (c) post-onset spilling, (d) developing spilling breaker, (e) pre-onset plunging, (f) onset plunging, (g) post-onset plunging, and (h) developing plunging breaker. The colors on the front face of the wave indicate the probability of the presence of active foam or aerated roller.

for pre-onset ensemble-averaged profiles has a mean of 0.05 and a standard deviation of 0.13, these variations are not deemed meaningful.

The effect of IR multipath reflections is much more pronounced for onset plunging breakers. The onset of plunging is manually determined by inspecting the wave-scale IR imagery for the moment the crest begins to overturn. This means that at onset, there is no active foam along the front face of the wave. However, Figure 4.11f shows very high probabilities of roller presence along the front face of the onset plunging ensemble-averaged wave profile. While not all plunging waves were reviewed again, several of those that were confirmed that the automated detection algorithm was triggered by multipath reflection from the steep wave face slope (25°-45°, Figure 3.9b). These results are supported laboratory measurements by Branch et al. (2014), who found multipath IR reflections were common for steep breakers in imagery collected at large incidence angle, as was the case for the FRF tower-mounted IR camera. For developing plunging breakers (Figure 4.11h), splash up and secondary plunging events (Basco, 1985) produce active foam along a highly variable and turbulent front wave face, and false extension of the roller due to multipath is not likely an issue.

For spilling breakers, onset is defined as the moment active foam appears near the peak (Figure 4.11b). In Figures 4.11c and 4.11d, the foam roller gradually extends down the front face of the wave (Basco, 1985). Despite the growth of the roller, the probability of roller presence remains relatively low at 0.5. This implies that there is considerable variability in roller evolution across spilling breakers. Multipath reflections may contribute to roller length variability for spilling breakers, though to a lesser extent than plunging breakers due to their shallower wave slopes (5°-25°, Figure 3.9b).

4.4.3   Parameterizing Plunging Breakers

Neither the bore nor roller models can capture the rapid and concentrated dissipation of energy seen for plunging breakers. However, other parameterizations have been developed specifically for plunging breakers. Estimates of the wave energy dissipation due to air entrainment in a plunging breaker vary widely, from 4%-9% of the total wave energy (Blenkinsopp

and Chaplin, 2007) to 30%-50% of the total wave energy (Lamarre and Melville, 1991). This large range was investigated by Iafrati (2011), who found through numerical modeling that the energy transferred from a plunging wave into the potential energy accumulated in bubbles accounted for various percentages of the total wave energy according to the wave steepness $\sigma = ka = H_0/2L_0$: 10%-15% for $\sigma = 0.50$, 20%-25% for $\sigma = 0.60$, 30%-35% for $\sigma = 0.65$. The Iafrati (2011) numerical simulation of plunging breakers provides guidance about the relative importance of air entrainment to wave energy dissipation, but has not yet been tested in the laboratory or field.

Drazen et al. (2008) and Iafrati (2011) use inertial scaling and treat the plunging wave crest as a projectile traveling a ballistic trajectory to model energy dissipation. Figure 4.12 schematically shows how Iafrati (2011) scales the area of the air cavity submerged by the plunging wave A_0 as,

$$A_0 \propto H \cdot B_p = H \cdot [(u_c - u_t) - (u_c - u_t)_{0.32}]\sqrt{2H}, \qquad (4.12)$$

where H is the trough to crest height of the plunging breaker at the point of maximum wave steepness, B_p is the width of the air cavity, and u_c and u_t are the speed of the wave crest and wave toe, respectively. The subscript 0.32 references the crest and toe speeds of the steepest non-breaking waves observed in the model. This parameterization could not be tested here, but it could provide an estimate of the energy lost to air entrainment by way of the work needed to submerge an air cavity of size A_0 against the force of buoyancy (Lamarre and Melville, 1991).

4.5   Conclusions

Using the LIDAR and IR-derived wave parameters defined in Chapter 2 and analyzed in Chapter 3, wave energy fluxes and dissipation rates are estimated for spilling and plunging breakers near the onset of breaking. A subset of spilling and plunging breakers are used in this analysis. Those chosen were observed for at least 0.3 wave periods following the onset of breaking and exhibited a mean wave height of 1.8-2 m. The effect of wavelength
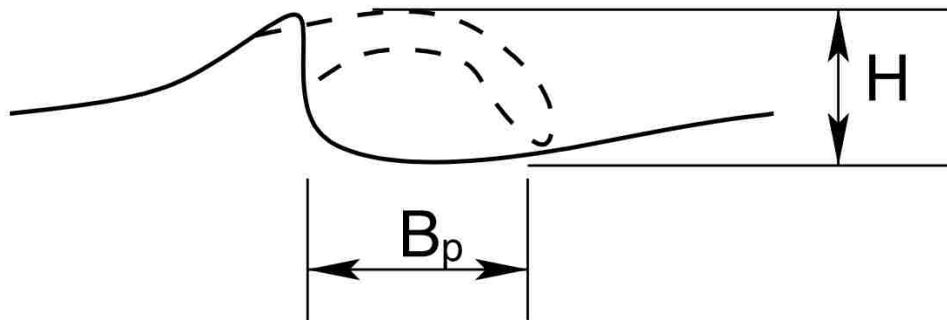
Figure 4.12: Schematic of a plunging breaker (from Iafrati (2011)), where B_p is the width of the air cavity, H is the trough to crest height of the plunging breaker at the point of maximum wave steepness, and the dashed outline is the trajectory of the plunging wave crest.

variation was accounted for by normalizing the distance since breaking by the wavelength, $x' = (x - x_b)/L$.

The normalized and ensemble-averaged wave energy flux, estimated using wave height and wave speed, shows that plunging breakers dissipate energy at a greater rate than spilling breakers near the onset of breaking, regardless of whether a mean wave speed or a tracked wave speed is used in the estimate. The wave energy flux exhibits its greatest rate of change for $-0.03 \geq x' > -0.2$ for both breaker types, and the normalized wave energy flux gradient, estimated using the tracked wave form speed, is 40% greater for plunging breakers than for spilling breakers over this interval. The ensemble-averaged and individual breaker results from Figures 4.6 and 4.7 confirm that plunging and spilling breakers are energetically different during the initial stages of breaking. Therefore, if the different dynamics of the initial stages of breaking are not somehow incorporated into wave models, the initial increased dissipation for plunging breakers will be missed.

The bore model estimates wave energy dissipation rate using the wave height, water depth, mean wave period, and B, the fraction of wave height covered by the bore (set to 1). The bore model predicts maximum dissipation rate at the onset of breaking for both spilling

and plunging breakers. However, high dissipation rate for plunging breakers is concentrated very near the onset of breaking, with a quick drop off to lower dissipation rates starting at $x' = -0.05$. Whereas, the dissipation rate for spilling breakers gradually decreases as the breaker develops, decreasing to 50% of the onset dissipation rate by $x' = -0.39$.

The roller model is also used to estimate wave energy dissipation rate for spilling and plunging breakers based on roller length, wave slope, mean wave period, and a constant that represents both the roller geometry and its density relative to that of sea water. Using the roller model, no statistically significant difference is found between dissipation rates for spilling and plunging breakers. The most likely explanation and source of error for the roller model is the effect of multipath reflection on the automated roller detection algorithm. Multipath IR reflections along a steeply sloped wave face amplify the thermal radiation received by the IR camera and either result in a roller identified in the absence of foam (just prior to onset) or a roller of artificially increased length (just after onset). The ensemble-averaged wave profiles of the probability of active foam strongly suggest that the former occurs for plunging breakers and the latter for both breaker types. These data limitations prohibit any substantial conclusions about wave energy dissipation rates estimated using the roller model.

Chapter 5

CONCLUSION

The application of this thesis is two fold: it makes a substantial contribution to the development of surf zone remote sensing methods and it provides geometric, kinematic, and energetic measurements of spilling and plunging breakers near the onset of breaking that are useful for improving nearshore wave models. The surf zone is a challenging environment in which to make measurements, and the data collected are invariably complicated by technology limitations or natural variability. The methods for fusing IR and LIDAR data to classify breaker type is vital to all of the results presented here, and the detailed account of the challenges of this dataset and our proposed solutions are useful for others using IR, LIDAR, or similar remote sensing technologies in the surf zone. The wave parameters analyzed, γ, wave slope, and wave speed, are commonly employed as breaking criteria in nearshore wave models. For phase-averaged models concerned with long timescale or large spatial scale processes, the bulk statistics and critical values of γ near the onset of breaking are useful. For phase-resolved models focused on short time and spatial scales processes, the local critical values of γ, wave slope, and wave speed are applicable. Potential avenues of future research using this data are discussed later in this chapter.

5.1 Main Findings

Chapter 2 presents detailed LIDAR-IR data fusion methodology to track individual waves, classify breaker type, and measure wave parameters in the surf zone. Utilizing the full spatial and temporal resolution of the LIDAR data, we track over 4200 waves. The surf zone-scale IR imagery is used to automatically identify candidate breakers, and the wave-scale IR imagery is manually reviewed to determined the moment of onset and classify breaker type. In IR,

an unorganized textured thermal signature on the back face of breaking waves indicates spilling type and an organized streaky thermal pattern indicates plunging type. In total, 524 spilling and plunging breakers are measured. Wave height is calculated as the difference between the spatially-derived peak elevation and the temporally-derived trough elevation, which guarantees that the true peak elevation of the wave is sampled and provides trough elevation even if its location is beyond the instrument field of view. Fitting the wave profiles with a skewed-Gaussian curve and using the fitted wave peaks to estimate instantaneous tracked wave speed produces a smoothly varying wave speed metric that is robust to noise due to spray or rapid wave shape changes. This wave speed metric is the best possible approximation (given the current dataset) of the wave phase speed. Four metrics of wave face slope are examined. When fitting a wave slope, the most robust estimate is achieved by using the upper 80% of the wave face. As expected, plunging breakers exhibit the steepest linear-fit wave slopes, though the quadratic fit or skewed-Gaussian fit wave slope may be more appropriate as the concavity increases near the onset of breaking.

Chapter 3 presents analysis of three key breaking wave parameters on a wave-by-wave basis: γ (the ratio of wave height to water depth), wave face slope, and wave phase speed. The range of γ calculated on a wave-by-wave basis agrees with previous *in situ* time-series estimations of γ at Duck, NC. Across the surf zone, we find that plunging breakers exhibit larger γ than spilling breakers, which suggests that the reported variability in γ ($0.4 < \gamma < 1.2$) from other field observations could be attributed to natural variability in the dominant breaker type at a given beach. γ, wave slope, and wave speed all reach their maximum value at or just after the onset of breaking. Plunging breakers exhibit 15% larger γ values and 18-36% steeper wave slopes than spilling breakers, but there is no statistically significant difference for wave speed. Together, γ and wave slope are strong predictors of breaking and breaker type. We also test the Miche steepness criteria for the onset of breaking in shallow water and find that there is a clear separation between breaking and non-breaking waves, with 99% of non-breaking waves falling below the Miche limit. However, the strict Miche limit applies only for some of the observed plunging breakers, and would underestimate the

breaking rates for most plunging and spilling breakers.

Chapter 4 presents a comparison of the wave energy flux gradient with dissipation rates from the bore model and roller model. For plunging breakers, the ensemble-averaged wave energy flux decreases at a rate up to 1.4 times that of spilling breakers within 0.2 wavelengths of the onset of breaking. When investigated on a wave-by-wave basis, plunging breakers again exhibit larger dissipation rates than spilling breakers, though the dissipation rates do not show correlation with the γ-θ parameter space used to predict breaking and breaker type. For plunging breakers, the ensemble-averaged bore model estimates high dissipation rates concentrated very near the onset of breaking followed by a sharp decline, while for spilling breakers, the dissipation rate gradually decreases from its maximum value at onset as the breakers develop. There is no statistically significant difference in the ensemble-averaged roller model dissipation rates for spilling and plunging breakers. The influence of multipath IR reflections on roller length estimates is the most likely cause of the large uncertainty in roller-based dissipation estimates. When analyzing a single breaker of each type, neither the bore nor the roller model capture the pattern of dissipation rate within 0.2 wavelengths of the onset for the plunging breaker.

5.2 Future Directions

5.2.1 Automated Breaker Type Classification

One of the strengths of this work is the volume of waves analyzed. However, this only represents about 10 hours out of almost two weeks worth of data. There are legitimate reasons for limiting the dataset. First, all necessary instruments (two IR cameras and one LIDAR) must be operational at the same time. This was not always the case as systems inevitably malfunction and must be fixed during a field experiment. Second, the wave conditions must include frequent breaking. This produces foam, which serves as a diffuse reflector for the LIDAR. In order to achieve dense returns along the cross-shore transect, sufficient foam must persist on the sea surface. Third, it is time-consuming to manually review the onset of

breaking and classify breaker types.

The first two limitations can only be addressed with a new field experiment or different instrumentation. However, there are remedies for the third limitation, and methods for handling and processing large datasets are an area of active research. Motivated by the need for automated breaker classification and encouraged by the distinct IR signatures of spilling and plunging breakers, Buscombe and Carini (2019) trained a deep convolution neural network (DCNN) to predict breaker type based on the wave-scale IR imagery. This work is part of only a handful of studies that used deep learning on geophysical imagery, and the first to address surf zone hydrodynamics. Processing over 400,000 images at 1 Hz, the DCNN model classifies breaker type (one type per image) with accuracies (F1 scores) of 0.97, 0.81, and 0.74, for non-breaking, spilling, and plunging waves, respectively. This result demonstrates the the DCNN is sensitive to subtle variations of IR image tone, contrast, saturation, and texture that collectively indicate a changing dynamic state, while being robust to variation in lighting, significant textural variation within a given breaker type, and a small training set of images. In analyzing the results, we found that the frequency of occurrence of plunging classifications increases as significant wave height and peak wave period increase, as shown in Figure 5.1. The opposite trend is seen for spilling classifications.

This motivates one area of continued research: using the DCNN results to investigate the continuum of breaker type. Breaking waves exist along a continuum between spilling and plunging (and collapsing and surging). For each image classified, the DCNN ascribes a probability for each class, where each probability can vary between 0 and 1, and the three classes do not sum to one. An example is shown in Figure 5.2.

We hypothesize that those waves whose DCNN classification is not dominated by any one class, but instead more evenly split between spilling and plunging, are examples of waves that exist along the continuum between spilling and plunging. To prove this hypothesis, we need to show that the DCNN classification probabilities produce consistent trends with respect to the breaker type continuum. While the human eye and brain are capable of recognizing an "in-between" spilling and plunging type breaking in the imagery, for an objective analysis, we
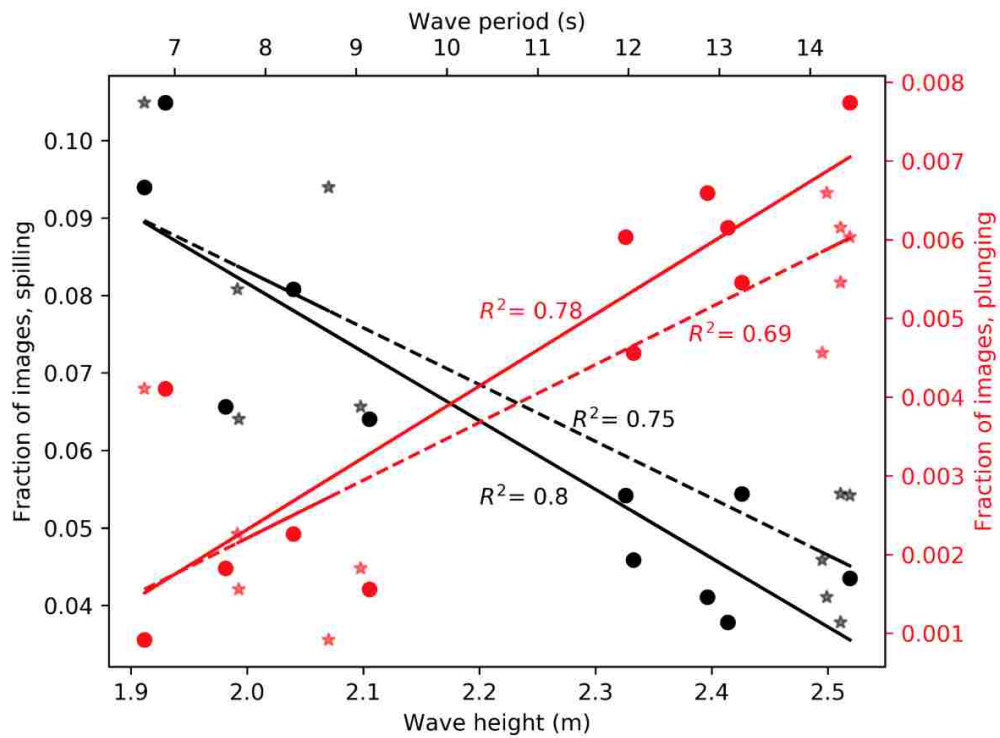
Figure 5.1: Fraction of images with spilling and plunging waves as a function of significant wave height (circles) and peak wave period (stars). [Figure created by Dan Buscombe using data provided by Roxanne J Carini.]
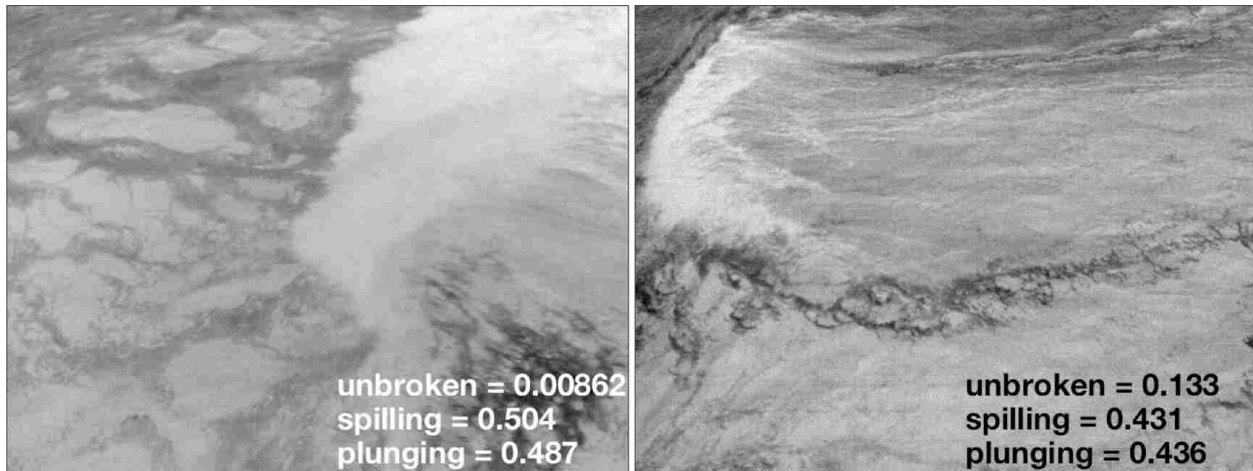
Figure 5.2: Two examples of DCNN classification results (predictive probabilities listed in bottom right corner of each image) for breakers that appear to exist somewhere along the continuum between spilling and plunging classes.

must define the breaker type continuum based on measurable wave parameters. One option would be to use the γ and wave slope relationships presented in this thesis to parameterize the breaker continuum.

5.2.2   *3D Sea Surface Reconstruction & EO-IR Data Fusion Applications*

Stereo imaging methods rely on feature matching across image pairs, and most stereo image processing software were developed for EO imagery, which typically have $\mathcal{O}$(10-100 Megapixels). Our IR cameras have 640x480 (307,200) pixels, and both commercial software PhotoScan and the Waves Acquisition Stereo System (WASS) by Benetazzo (2006) failed to identify enough matched features for sea surface reconstruction due to this coarse resolution. However, stereo EO imagery collected during ROLLEX and preliminary work by Ladner and Palmsten (2017) shows successful reconstruction of a region of the sea surface that overlaps the wave-scale IR imagery FOV (Figure 5.3).

Stereo reconstruction of the sea surface would expand the dataset by capturing more instances of waves at onset of breaking (not limited to the alongshore location of the LIDAR
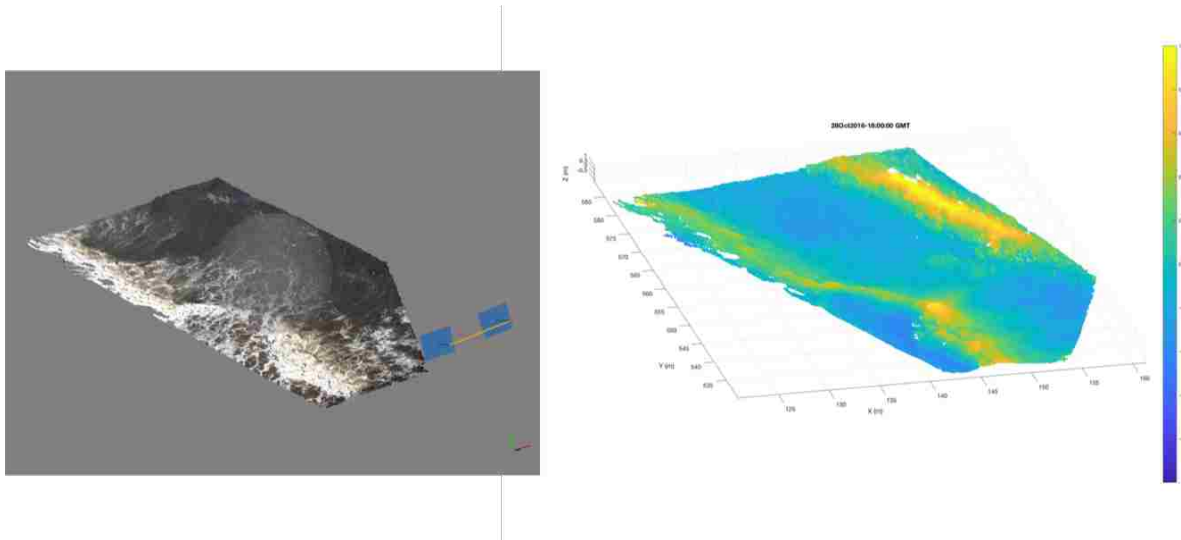
Figure 5.3: 3D sea surface reconstruction from stereo pair of EO cameras deployed alongside the IR cameras on the FRF pier during ROLLEX (Ladner and Palmsten, 2017).

transect). It could also be used to investigate along-crest variability in wave height, wave slope, roller length, and wave speed, for a more robust examination of breaking criteria.

Combining EO and IR imagery may provide a solution for the multipath IR errors in roller identification. The thresholding methods from Carini et al. (2015) would first be used on the IR imagery to segregate active foam and regions of high reflectance from residual foam and undisturbed sea surface. Then, the collocated EO imagery along the wave face is used to separate the roller (bright, white) from the steep wave face (dark). We note that for certain positions of the sun relative to the EO camera, reflections from steep wave slopes may still pose a problem for roller isolation.

5.2.3   Wave Energy Dissipation Rate

Chapter 4 presents wave energy flux measurements that confirm that plunging breakers dissipate energy at a greater rate than spilling breakers in the early stages of breaking. Neither the bore nor the roller model capture these differences. Chapter 4 proposed a

plunging wave model that parameterizes the energy lost to air entrainment at the onset of plunging breaking using the work needed to submerge an air cavity of size A_0 against the buoyancy force (Lamarre and Melville, 1991; Drazen et al., 2008; Iafrati, 2011). While the LIDAR data presented here is insufficient to resolve the plunge distance, B_p in Figure 4.12, recent multibeam LIDAR observations of plunging breakers demonstrate robust visualization of the plunging air cavity (Brodie et al., 2018). The area of this air cavity could also be estimated via the parametric cubic curve fitting (Longuet-Higgins, 1982) as pursued by Brodie et al. (2018).

Another next step of this research would be to expand the cross-shore extent of LIDAR coverage, similar to the coverage demonstrated by Martins et al. (2016), in order to guarantee the observation of a wave from the onset of breaking, thorough development, to steady state. In this way, we could quantify the time or space, relative to wave period or wavelength, required for a spilling or plunging breaker to evolve into a steady state bore. We found that 0.15 T after the onset marks a distinct transition in the character of energy dissipation for both spilling and plunging breakers, but the waves are not observed long enough to know if a second transition occurs. This information would help answer questions such as: How much energy does a wave lose during its onset stage relative to its steady state stage? Given that the bore model is applied universally, what are the consequences of not including or including onset dynamics when modeling wave forcing across the full surf zone? How might the bore model be modified to improve predictions of nearshore processes that are sensitive to the temporal and spatial patterns in wave forcing, such as transient rip currents?

Appendix A

BATHYMETRY VALIDATION

Using LIDAR-derived wave phase speeds for non-breaking waves, so as to avoid any speed-altering effects of breaking, water depth at the study site was derived by inverting the relationships of shallow water linear wave theory:

$$c_{lin} = \sqrt{gh_{MSL}}, \tag{A.1}$$

solitary wave theory:

$$c_{sol} = \sqrt{g(h_{MSL} + H)}, \tag{A.2}$$

and shock wave theory:

$$c_{shock} = -2(gh_{MSL})^{1/2} + 2(gh_{tr})^{1/2} + \left(\frac{gh_{pk}}{2h_{tr}}(h_{tr} + h_{pk})\right)^{1/2}. \tag{A.3}$$

Figure A.1 shows that the bin-averaged depths inverted from solitary and shock wave theories agree well with the interpolated bathymetry at both the onshore and offshore locations of the pier instruments, while shallow water linear wave theory predicts depths more than 1 m deeper. This is consistent with work by Postacchini and Brocchini (2014); Tissier et al. (2011), and Martins et al. (2018), which show that solitary wave and shock wave theories produce similar results and out-perform linear wave theory for predicting wave speed in the surf zone. The solitary wave and shock wave theory depth-inversion calculations strongly support the use of the date-weighted interpolated bathymetry for the offshore LIDAR transect, where little change is observed from 03 to 16 November. For the onshore transect, where much larger changes are observed between the survey dates, the difference between the interpolated and solitary wave theory-inverted bathymetry ranges from about 10 cm to 40 cm.
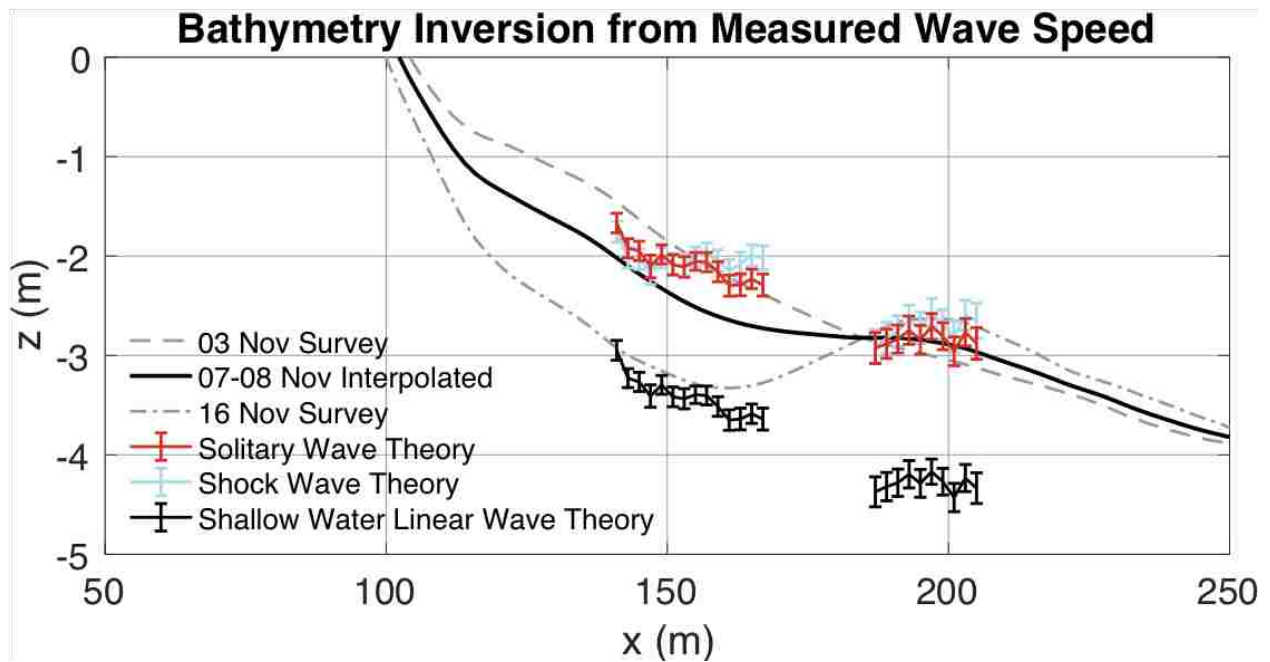
Figure A.1: Cross-shore transect of the surveyed bathymetry from 03 November (dashed gray) and 16 November (dot-dashed gray) and the time-weighted, linearly interpolated bathymetry (solid black) for data collection time period. Bin-averaged depth-inversion results using solitary wave theory (red), shock wave theory (blue) and shallow water linear wave theory (black) with 95% confidence intervals.

BIBLIOGRAPHY

Aarninkhof, S. G. and Ruessink, B. G. (2004). Video observations and model predictions of depth-induced wave dissipation. *IEEE Transactions on Geoscience and Remote Sensing*, 42(11):2612–2622.

Adeyemo, M. (1968). Effect of beach slope and shoaling on wave asymmetry. *Coastal Engineering Proceedings*, 1(11).

Apotsos, A., Raubenheimer, B., Elgar, S., and Guza, R. (2008). Testing and calibrating parametric wave transformation models on natural beaches. *Coastal Engineering*, 55(3):224–235.

Baldock, T., Holmes, P., Bunker, S., and Van Weert, P. (1998). Cross-shore hydrodynamics within an unsaturated surf zone. *Coastal Engineering*, 34(3-4):173–196.

Basco, D. R. (1985). A qualitative description of wave breaking. *Journal of waterway, port, coastal, and ocean engineering*, 111(2):171–188.

Battjes, J. (1988). Surf-zone dynamics. *Annual Review of Fluid Mechanics*, 20(1):257–291.

Battjes, J. A. (1975). Surf similarity. In *Coastal Engineering*, pages 466–480. ASCE Library.

Battjes, J. A. and Janssen, J. (1978). Energy loss and set-up due to breaking of random waves. In *Coastal Engineering 1978*, pages 569–587. ASCE Library.

Benetazzo, A. (2006). Measurements of short water waves using stereo matched image sequences. *Coastal engineering*, 53(12):1013–1032.

Benetazzo, A., Ardhuin, F., Bergamasco, F., Cavaleri, L., Guimarães, P. V., Schwendeman, M., Sclavo, M., Thomson, J., and Torsello, A. (2017). On the shape and likelihood of oceanic rogue waves. *Scientific Reports*, 7(1):8276.

Birkemeier, W. A., Miller, H., Wilhelm, S., DeWall, A., and Gorbics, C. (1985). A user's guide to the coastal engineering research center's (cerc's) field research facility. Technical report, DTIC Document.

Blenkinsopp, C. and Chaplin, J. (2007). Void fraction measurements in breaking waves. In *Proceedings of the Royal Society of London A: Mathematical, Physical and Engineering Sciences*, volume 463, pages 3151–3170. The Royal Society.

Blenkinsopp, C., Mole, M., Turner, I., and Peirson, W. (2010). Measurements of the time-varying free-surface profile across the swash zone obtained using an industrial lidar. *Coastal Engineering*, 57(11-12):1059–1065.

Booij, N. et al. (2008). Swan technical documentation: Swan cycle iii version 40.72. *Delft University of Technology*.

Booij, N., Holthuijsen, L., and Ris, R. (1997). The" swan" wave model for shallow water. In *Coastal Engineering 1996*, pages 668–676. ASCE Library.

Branch, R., Chickadel, C. C., and Jessup, A. T. (2014). Thermal infrared multipath reflection from breaking waves observed at large incidence angles. *IEEE Transactions on Geoscience and Remote Sensing*, 52(1):249–256.

Branch, R., Chickadel, C. C., and Jessup, A. T. (2016). Infrared emissivity of seawater and foam at large incidence angles in the 3–14μm wavelength range. *Remote Sensing of Environment*, 184:15–24.

Brodie, K., Albright, A., Hartzell, P. J., Bak, S., Collins, C. O., Hesser, T., and Dickhudt, P. (2018). Multi-beam lidar observations of breaking waves. In *Close-Range Remote*

Sensing of Nearshore Processes and Coastal Morphology. American Geophysical Union Fall Meeting.

Brodie, K. L., Raubenheimer, B., Elgar, S., Slocum, R. K., and McNinch, J. E. (2015). Lidar and pressure measurements of inner-surfzone waves and setup. *Journal of Atmospheric and Oceanic Technology*, 32(10):1945–1959.

Brodie, K. L., Raubenheimer, B., Spore, N. J., Gorrell, L., Slocum, R. K., and Elgar, S. (2016). Lidar observations of wave shape. In *Nearshore Processes*. American Geophysical Union: Ocean Sciences Meeting.

Buscombe, D. and Carini, R. J. (2019). A data-driven approach to classifying wave breaking in infrared imagery. Submitted to Coastal Engineering.

Carini, R. J., Chickadel, C. C., Jessup, A. T., and Thomson, J. (2015). Estimating wave energy dissipation in the surf zone using thermal infrared imagery. *Journal of Geophysical Research: Oceans*, 120(6):3937–3957.

Chella, M. A., Bihs, H., Myrhaug, D., and Muskulus, M. (2015). Breaking characteristics and geometric properties of spilling breakers over slopes. *Coastal Engineering*, 95:4–19.

Chella, M. A., Bihs, H., Myrhaug, D., and Muskulus, M. (2016). Hydrodynamic characteristics and geometric properties of plunging and spilling breakers over impermeable slopes. *Ocean Modelling*, 103:53–72.

Dally, W. R. and Brown, C. A. (1995). A modeling investigation of the breaking wave roller with application to cross-shore currents. *Journal of Geophysical Research: Oceans*, 100(C12):24873–24883.

Derakhti, M., Banner, M. L., and Kirby, J. T. (2018). Predicting the breaking strength of gravity water waves. *arXiv preprint arXiv:1802.03586.*

Díaz, H., Catalán, P. A., and Wilson, G. W. (2017). Quantification of two-dimensional wave breaking dissipation in the surf zone from remote sensing data. *Remote Sensing*, 10(1):38.

Drazen, D. A., Melville, W. K., and Lenain, L. (2008). Inertial scaling of dissipation in unsteady breaking waves. *Journal of Fluid Mechanics*, 611:307–332.

Duncan, J. (1981). An experimental investigation of breaking waves produced by a towed hydrofoil. *Proc. R. Soc. Lond. A*, 377(1770):331–348.

Duncan, J. H. (2001). Spilling breakers. *Annual review of fluid mechanics*, 33(1):519–547.

Elgar, S., Herbers, T. H. C., and Guza, R. T. (1994). Reflection of ocean surface gravity waves from a natural beach. *Journal of Physical Oceanography*, 24(7):1503–1511.

Elko, N., Feddersen, F., Foster, D., Hapke, C., McNinch, J., Mulligan, R., zkan Haller, H. T., Plant, N., and Raubenheimer, B. (2014). The future of nearshore processes research. In *Abstract OS22A-08 presented at 2014 Fall Meeting, AGU, San Francisco, Calif., December.*

Feddersen, F. (2012). Scaling surf zone turbulence. *Geophysical Research Letters*, 39(18):L18613.

Fogelberg, R. A. (2003). A study of microbreaking modulation by ocean swell using infrared and microwave techniques. Master's thesis, University of Washington.

Forte, M. F., Birkemeier, W. A., and Mitchell, J. (2017). Nearshore survey system evaluation. Technical report, ERDC-CHL Vicksburg United States.

Forte, M. F. and Dopsovic, R. (2016). Field research facility data integration framework data management plan: Survey lines dataset. Technical report, US Army Engineer Research and Development Center Duck United States.

Galvin, C. J. (1968). Breaker type classification on three laboratory beaches. *Journal of geophysical research*, 73(12):3651–3659.

Govender, K., Mocke, G., and Alport, M. (2002). Video-imaged surf zone wave and roller structures and flow fields. *Journal of Geophysical Research: Oceans*, 107(C7).

Grilli, S., Svendsen, I., and Subramanya, R. (1997). Breaking criterion and characteristics for solitary waves on slopes. *Journal of waterway, port, coastal, and ocean engineering*, 123(3):102–112.

Haller, M. C. and Catalan, P. A. (2009). Remote sensing of wave roller lengths in the laboratory. *Journal of Geophysical Research-Oceans*, 114.

Handler, R. A., Savelyev, I., and Lindsey, M. (2012). Infrared imagery of streak formation in a breaking wave. *Physics of Fluids*, 24(12):121701.

Hartley, R. and Zisserman, A. (2003). *Multiple view geometry in computer vision.* Cambridge university press.

Holland, K. T., Holman, R. A., Lippmann, T. C., Stanley, J., and Plant, N. (1997). Practical use of video imagery in nearshore oceanographic field studies. *IEEE Journal of oceanic engineering*, 22(1):81–92.

Holman, R. and Haller, M. C. (2013). Remote sensing of the nearshore. *Annual Review of Marine Science*, 5:95–113.

Holman, R. A., Sallenger, A. H., Lippmann, T. C., and Haines, J. W. (1993). The application of video image processing to the study of nearshore processes. *Oceanography*, 6(3):78–85.

Huang, Z.-C. and Hwang, K.-S. (2015). Measurements of surface thermal structure, kinematics, and turbulence of a large-scale solitary breaking wave using infrared imaging techniques. *Coastal Engineering*, 96:132–147.

Iafrati, A. (2011). Energy dissipation mechanisms in wave breaking processes: spilling and highly aerated plunging breaking events. *Journal of Geophysical Research: Oceans*, 116(C7).

Janssen, T. and Battjes, J. (2007). A note on wave energy dissipation over steep beaches. *Coastal Engineering*, 54(9):711–716.

Jessup, A., Zappa, C., Loewen, M., and Hesany, V. (1997a). Infrared remote sensing of breaking waves. *Nature*, 385(6611):52.

Jessup, A., Zappa, C. J., and Yeh, H. (1997b). Defining and quantifying microscale wave breaking with infrared imagery. *Journal of Geophysical Research: Oceans*, 102(C10):23145–23153.

Kjeldsen, S., Myrhaug, D., et al. (1979). Breaking waves in deep water and resulting wave forces. In *Offshore Technology Conference*. Offshore Technology Conference.

Komar, P. D. and Gaughan, M. K. (1973). Airy wave theory and breaker height prediction. In *Coastal Engineering 1972*, pages 405–418. ASCE Library.

Ladner, H. and Palmsten, M. (2017). Stereo reconstruction of 3d sea surface of surf zone breaking waves using eo imagery. personal communication.

Lamarre, E. and Melville, W. (1991). Air entrainment and dissipation in breaking waves. *Nature*, 351(6326):469–472.

Le Mehaute, B. (1962). On non-saturated breakers and the wave run-up. *Coastal Engineering Proceedings*, 1(8):6.

Lippmann, T., Brookins, A. s., and Thornton, E. (1996). Wave energy transformation on natural profiles. *Coastal Engineering*, 27(1-2):1–20.

Longuet-Higgins, M. S. (1982). Parametric solutions for breaking waves. *Journal of Fluid Mechanics*, 121:403424.

Madsen, P. A., Sørensen, O., and Schäffer, H. (1997). Surf zone dynamics simulated by a boussinesq type model. part i. model description and cross-shore motion of regular waves. *Coastal Engineering*, 32(4):255–287.

Marmorino, G. and Smith, G. (2005). Bright and dark ocean whitecaps observed in the infrared. *Geophysical research letters*, 32(11).

Martins, K., Blenkinsopp, C., Deigaard, R., and Power, H. (2018). Energy dissipation in the inner surf zone: New insights from lidar-based roller geometry measurements. *Journal of Geophysical Research: Oceans.*

Martins, K., Blenkinsopp, C. E., Almar, R., and Zang, J. (2017a). The influence of swash-based reflection on surf zone hydrodynamics: a wave-by-wave approach. *Coastal Engineering*, 122:27–43.

Martins, K., Blenkinsopp, C. E., Power, H. E., Bruder, B., Puleo, J. A., and Bergsma, E. W. (2017b). High-resolution monitoring of wave transformation in the surf zone using a lidar scanner array. *Coastal Engineering*, 128:37–43.

Martins, K., Blenkinsopp, C. E., and Zang, J. (2016). Monitoring individual wave characteristics in the inner surf with a 2-dimensional laser scanner (lidar). *Journal of Sensors*, 2016.

Miche, A. (1944). Mouvements ondulatoires de la mer en profondeur croissante ou décroissante. Première partie: Mouvements ondulatoires périodiques et cylindriques en profondeur constante. *Annales des Ponts et Chaussées*, 114:42–78.

Miller, R. L. and Zeigler, J. M. (1964). The internal velocity field in breaking waves. *Coastal Engineering Proceedings*, 1(9).

Mukaro, R., Govender, K., and Mccreadie, H. (2013). Wave height and wave velocity measurements in the vicinity of the break point in laboratory plunging waves. *Journal of Fluids Engineering*, 135(6):061303.

Munk, W. H. (1949). The solitary wave theory and its application to surf problems. *Annals of the New York Academy of Sciences*, 51(1):376–424.

Niclòs, R., Caselles, V., Valor, E., and Coll, C. (2007). Foam effect on the sea surface emissivity in the 8–14 μm region. *Journal of Geophysical Research: Oceans*, 112(C12).

Plant, N., Holman, R., Freilich, M., and Birkemeier, W. (1999). A simple model for inter-annual sandbar behavior. *Journal of Geophysical Research-Oceans*, 104(C7):15755–15776.

Postacchini, M. and Brocchini, M. (2014). A wave-by-wave analysis for the evaluation of the breaking-wave celerity. *Applied Ocean Research*, 46:15–27.

Power, H. E., Hughes, M. G., and Baldock, T. E. (2015). A novel method for tracking individual waves in the surf zone. *Coastal Engineering*, 98:26–30.

Raubenheimer, B., Guza, R., and Elgar, S. (1996). Wave transformation across the inner surf zone. *Journal of Geophysical Research: Oceans*, 101(C11):25589–25597.

Reniers, A. and Battjes, J. (1997). A laboratory study of longshore currents over barred and non-barred beaches. *Coastal Engineering*, 30(1):1–21.

Robertson, B., Nistor, I., Hall, K., and Buckham, B. (2014). Remote measurement and prediction of breaking wave parameters. *Coastal Engineering Proceedings*, 1(34):41.

Ruessink, B., Miles, J., Feddersen, F., Guza, R., and Elgar, S. (2001). Modeling the along-shore current on barred beaches. *Journal of Geophysical Research: Oceans (1978–2012)*, 106(C10):22451–22463.

Ruessink, B., Walstra, D., and Southgate, H. (2003). Calibration and verification of a parametric wave model on barred beaches. *Coastal Engineering*, 48(3):139–149.

Sallenger, A. H. and Holman, R. A. (1985). Wave energy saturation on a natural beach of variable slope. *Journal of Geophysical Research: Oceans*, 90(C6):11939–11944.

Schlax, M. G. and Chelton, D. B. (1992). Frequency domain diagnostics for linear smoothers. *Journal of the American Statistical Association*, 87(420):1070–1081.

Smit, P., Janssen, T., Holthuijsen, L., and Smith, J. (2014). Non-hydrostatic modeling of surf zone wave dynamics. *Coastal Engineering*, 83:36 – 48.

Stoker, J. J. (2011). *Water waves: The mathematical theory with applications*, volume 36. John Wiley & Sons.

Suhayda, J. N. and Pettigrew, N. R. (1977). Observations of wave height and wave celerity in the surf zone. *Journal of Geophysical Research*, 82(9):1419–1424.

Thornton, E. B. and Guza, R. (1983). Transformation of wave height distribution. *Journal of Geophysical Research: Oceans*, 88(C10):5925–5938.

Thornton, E. B. and Guza, R. T. (1986). Surf zone longshore currents and random waves: Field data and models. *Journal of Physical Oceanography*, 16(7):1165–1178.

Ting, F. C. and Kirby, J. T. (1995). Dynamics of surf-zone turbulence in a strong plunging breaker. *Coastal Engineering*, 24(3-4):177–204.

Ting, F. C. and Kirby, J. T. (1996). Dynamics of surf-zone turbulence in a spilling breaker. *Coastal Engineering*, 27(3-4):131–160.

Tissier, M., Bonneton, P., Almar, R., Castelle, B., Bonneton, N., and Nahon, A. (2011). Field measurements and non-linear prediction of wave celerity in the surf zone. *European Journal of Mechanics-B/Fluids*, 30(6):635–641.

Tissier, M., Bonneton, P., Michallet, H., and Ruessink, B. (2015). Infragravity-wave modulation of short-wave celerity in the surf zone. *Journal of Geophysical Research: Oceans*, 120(10):6799–6814.

Watanabe, Y. and Mori, N. (2008). Infrared measurements of surface renewal and subsurface vortices in nearshore breaking waves. *Journal of Geophysical Research: Oceans*, 113(C7).

Weishar, L. L. and Byrne, R. J. (1978). Field study of breaking wave characteristics. In *Coastal Engineering 1978*, pages 487–506. ASCE Library.

Whitford, D. J. (1988). *Wind and wave forcing of longshore currents across a barred beach.* PhD thesis, Monterey, California. Naval Postgraduate School.

Wright, L. and Short, A. D. (1984). Morphodynamic variability of surf zones and beaches: a synthesis. *Marine geology*, 56(1-4):93–118.

Zijlema, M., Stelling, G., and Smit, P. (2011). Swash: An operational public domain code for simulating wave fields and rapidly varied flows in coastal waters. *Coastal Engineering*, 58(10):992–1012.